
This item was submitted to [Loughborough's Research Repository](#) by the author.
Items in Figshare are protected by copyright, with all rights reserved, unless otherwise indicated.

Novel insulation techniques for high voltage pulse transformers

PLEASE CITE THE PUBLISHED VERSION

PUBLISHER

© Jing Luo

LICENCE

CC BY-NC-ND 4.0

REPOSITORY RECORD

Luo, Jing. 2019. "Novel Insulation Techniques for High Voltage Pulse Transformers". figshare.
<https://hdl.handle.net/2134/13327>.

This item was submitted to Loughborough University as a PhD thesis by the author and is made available in the Institutional Repository (<https://dspace.lboro.ac.uk/>) under the following Creative Commons Licence conditions.



For the full text of this licence, please go to:
<http://creativecommons.org/licenses/by-nc-nd/2.5/>

University Library

Author/Filing Title LUO, J

.....
Class Mark T

Please note that fines are charged on ALL
overdue items.

FOR REFERENCE ONLY

0403603277



Novel Insulation Techniques for High-Voltage Pulse Transformers

by

Jing Luo, B Eng

A Doctoral thesis submitted in partial fulfilment of the requirements for the award
of Doctor of Philosophy of Loughborough University

November, 2006

© by *Jing Luo* , 2006



Loughborough
University
Pilkington Library

Date

July

Class

T

Acc

No. 0403603277

Acknowledgments

First of all, I would like to express my sincere appreciation and thanks to my supervisor, Professor Ivor Smith, for the continuous support that he has provided, not only in research matters but also in various personal concerns and areas of day to day living in a foreign country. In particular, I am grateful for his ready and congenial availability for counselling, whatever the problem or difficulty. Both his wide knowledge and his logical way of thinking have been of great value for me. His encouraging, personal guidance and detailed constructive comments provided a good basis for the present thesis.

I must acknowledge my indebtedness to Dr. Bucur Novac. He was a constant source of inspiration, providing a steady flow of novel ideas for my research, and with a great wish to help and support young people like me to achieve scientific excellence. I must thank him for his systematic guidance and the great effort that he put into training me in the scientific field.

I would also like to thank Mr D F Rankin and Mr P Sarkar, colleagues in the Pulsed-Power Research Group at Loughborough University for providing constant and friendly help throughout the past three years. Special thanks also go to Dr M. Istenič for his enormous assistance throughout my time as a research student. He was in charge of the experiments reported in the thesis and he proposed many improvements to my primitive designs. He was always ready to provide expert advice and assistance in experimental situations, and prepared to devote much time to discussing with me various questions.

I also would like to give my express to my friends , Ma Xiaomei, Liu Zhen, Wang Shanshan and Shi Jianjun, for the time we have spent together, which was full of laughter, mutual encouragement, and generous care.

Finally, I take this opportunity to express the profound gratitude to my family for their love and continuous support, both spiritual and material.

Abstract

This thesis describes a research investigation into novel designs of high voltage pulse transformers using magnetic insulation, which is the only practicable form of insulation for much of the equipment presently used in ultrahigh voltage pulsed-power work, including transmission lines and plasma opening switches. Although its use in transformers would bring important advantages in both size and weight reductions, a number of seemingly insurmountable problems have however so far prevented this.

Two novel arrangements are presented in this thesis: one of these is a 500 *kV* transformer with *self*-magnetic insulation, and the other one is a 1 *MV* 'Tesla' transformer with *external* magnetic insulation. It is shown that both of these overcome the problems inherent in earlier designs and also offer considerable scope for further development in a number of important areas. It is believed that they represent the first working examples of magnetically-insulated transformers anywhere in the world.

Modelling considerations of the transformers developed include both theoretical models and predicted characteristics. The filamentary technique used to describe mathematically the arrangements being investigated involves decomposition of the main conducting components into filamentary elements. The resulting equivalent electrical network includes all the mutual interactions that exist between the different filamentary elements, takes magnetic diffusion fully into account and enables the resistances and self and mutual inductances that are effective under fast transient conditions to be calculated. Theoretical results provided by the resulting mathematical models have been successfully validated by comparison with reliable experimental data.

Much of the work detailed in the thesis has already been presented in high quality academic journals and at prestigious international conferences, and a solid theoretical and experimental basis has been laid down for future development and new progress into pulsed power system research.

Key words: Magnetic insulation, high voltage pulse transformers, filamentary modelling

Table of Contents

1	Introduction	1
1.1	High voltage pulse transformer	8
1.1.1	Advantage and development of air cored transformers.....	8
1.1.2	Types of air cored transformers	9
1.1.3	Transformer insulation	12
1.2	Magnetic insulation technique	14
1.3	Thesis objectives	18
1.4	Thesis organisation.....	20
2	Filamentary modelling.....	22
2.1	Introduction to filamentary modelling	22
2.2	General formulation	24
2.3	Electrical properties of θ -current circuits	27
2.3.1	Magnetic vector potential of a circular current loop	27
2.3.2	Magnetic flux density of a circular current loop	28
2.3.3	Forces between two parallel coaxial loops	29
2.3.4	Mutual inductance of two parallel and coaxial circular loops.....	30
2.3.5	Self inductance of circular loop.....	31
2.3.5.1	Finite rectangular cross-section conductors.....	31
2.3.5.2	Finite circular cross-section conductors.....	31
2.3.5.3	Finite ribbon cross-section conductors	32
2.3.6	Resistance	32
2.4	Electrical properties of z-current circuits	33
2.4.1	Magnetic flux density of straight conductor in z-current circuits	33
2.4.2	Forces between two parallel filaments	34
2.4.3	Mutual inductance of two parallel filaments	34
2.4.4	Self inductance of coaxial structures	35
2.4.5	Resistance of cylindrical conductor geometry.....	35
2.5	HVT inductance calculations	36
2.5.1	The textbook formula	36

2.5.2	The Energy Method	36
2.5.3	The Magnetic Flux Method	37
2.6	Skin and proximity effects	39
2.7	Magnetic field, forces and other issuers.....	40
2.8	Capacitance calculation.....	41
2.9	Electric field and potential distribution	43
2.10	2D modelling of HVT.....	44
2.10.1	HVT basic geometries	44
2.10.2	2D modelling of a spiral-strip HVT	46
2.10.3	2D modelling of a helical HVT	50
2.11	Benchmarking with experimental results	53
2.11.1	Inductance calculations.....	53
2.11.2	Dynamic HVT performance in a conditioning system.....	55
3	Finite element analysis	58
3.1	Introduction to FEA	58
3.2	Field computations	60
3.3	General formulation	62
3.4	Electrical field analysis of spiral strip pulse transformer	67
3.4.1	Edge effect.....	69
3.4.2	Field enhancement factor.....	70
3.4.3	Field enhancement optimisation.....	75
3.4.3.1	Round edge	75
3.4.3.2	Insulation material	76
3.4.3.3	Cage techniques	77
3.5	Electrical field analysis of helical pulse transformer	81
4	Design of 500 kV spiral-strip transformers with magnetic insulation.....	84
4.1	Transformer arrangement.....	86
4.1.1	Description of transformer arrangement.....	86
4.1.2	Primary and secondary coil parameters and material selection.....	89
4.1.3	Primary conditioning system and EWA design.....	91
4.2	Filamentary modelling	92
4.3	Breakdown analysis.....	98

4.4	Implementation of magnetic insulation technique	99
4.4.1	Magnetic self-insulation	100
4.4.1.1	Theoretical description.....	100
4.4.1.2	Estimation of magnetic insulation characteristics.....	104
4.4.2	Magnetic insulation with imposed field	106
4.4.2.1	Imposed field system design.....	106
4.4.2.2	Evaluation on the efficiency of the imposed field	108
5	Design of a 1 MV HVT with external magnetic insulation.....	110
5.1	Introduction to the Tesla transformer.....	110
5.1.1	Brief history of Tesla coil.....	111
5.1.2	Simplified theory of operation.....	113
5.2	Design specification and main solutions	115
5.2.1	Primary capacitor selection	117
5.2.2	Spark gap selection.....	118
5.2.3	Tesla coil dimensions and material selection	120
5.2.4	External field system design.....	122
5.3	Simulation model	123
5.3.1	Theory of operation	124
5.3.2	Parameter calculation	125
5.3.3	Optimized system	126
6	Testing	132
6.1	Self-Magnetic insulation of 500 kV HVT [6.1]	132
6.1.1	Experimental set up	132
6.1.2	Analysis of results	138
6.1.2.1	Preliminary experimentation.....	138
6.1.2.2	EWA performance	140
6.1.2.3	Inductance.....	144
6.1.2.4	Transformer performance	146
6.1.3	Magnetic insulation dependence on primary current [6.1].....	148
6.2	Magnetic insulation of 1 MV HVT [6.8]	152
6.2.1	Experimental arrangement.....	152
6.2.2	Diagnostic methods	161

6.2.3 Analysis of results	161
7 Conclusion	163
Published papers.....	165
References.....	167

List of Figures

Figure 1.1 Marx generator circuit	2
Figure 1.2 Operation circuit of a three-stage LC generator	3
Figure 1.3 Three-stage stacked strip-line generator.....	4
Figure 1.4 Stacked coaxial-line generator	5
Figure 1.5 Spiral generator	5
Figure 1.6 Shape of the output pulse from a spiral generator on open circuit.....	6
Figure 1.7 Arrangement for helical HVT developed at Loughborough University [1.10]	10
Figure 1.8 Arrangement for spiral-strip HVT developed at Loughborough University with only showing secondary turns for clarity [1.11].....	11
Figure 1.9 Magnetic insulation principle with vector B parallel to plates and orthogonal to electric field showing (a) $B = 0$ and (b) scalloped drift orbit viewed in the stationary frame (c) drift orbit viewed in a frame of reference moving at the electron drift velocity	14
Figure 1.10 Critical magnetic field strength for magnetic insulation versus voltage between anode-cathode gap ($d = 10 \text{ mm}$).....	18
Figure 2.1 Circular current loop.....	27
Figure 2.2 Forces between two parallel coaxial loops.....	29
Figure 2.3 Hypothetical rail gun configuration used for filamentary modelling.....	33
Figure 2.4 Loughborough based pulsed power system including a spiral-strip HVT [2.18]	44
Figure 2.5 Helical HVT developed at Texas Tech University (TTU), USA [2.19]	45
Figure 2.6 Simplified view of spiral-strip HVT circuit for use in filamentary modelling.	47
Figure 2.7 Filamentary representation of the spiral-strip HVT	48
Figure 2.8 Equivalent filamentary circuit diagram for a spiral strip HVT	49
Figure 2.9 Filamentary representation of the helical HVT	51
Figure 2.10 Equivalent filamentary circuit diagram for a helical HVT.....	52
Figure 2.11 Variation of primary inductance L_p with the number of filaments in the axial direction n_p	54
Figure 2.12 Equivalent lumped circuit of a laboratory based pulsed power system	56
Figure 2.13 Load voltage for the laboratory based system presented in [2.20].....	56

Figure 2.14 Load voltage for the Loughborough system presented in Figure 2.3	57
Figure 3.1 Typical FEA process	59
Figure 3.2 A spiral winding arrangement showing (a) electric field distribution (b) equipotential lines.....	68
Figure 3.3 Geometry of a planar layered insulation structure	70
Figure 3.4 Ideal layered cylindrical insulation structure	73
Figure 3.5 The distribution of electric field lines with (a) unprofiled electrode (b) profiled electrode.....	76
Figure 3.6 Map of electric field equal potentials for the spiral-strip Loughborough HVT	78
Figure 3.7 Same as Figure 3.6, but using simplified end rings: maximum electric field <i>MV / m</i>	79
Figure 3.8 Same as Figure 3.6, but only one cage present: maximum electric field <i>MV / m</i>	79
Figure 3.9 Electric field distribution along the edge of Loughborough spiral-strip HVT 15 turn secondary using various cage structures corresponding to A) Figure 3.6 (a), B) Figure 3.6 (b), C) Figure 3.7 D) Figure 3.8.....	80
Figure 3.10 Equivalent circuit with (a) spiral-strip winding (b) helical winding	81
Figure 3.11 Map of electric field equal potentials for the helical TTU (a) with grading technique (b) without grading technique	83
Figure 4.1 Schematic of an explosively-driven single-shot power supply for a HPM load (FCG- flux-compression generators, OS- opening switch, SG-spark gap,).....	84
Figure 4.2 Equivalent lumped circuit of a laboratory based pulsed power system	87
Figure 4.3 Cross section of magnetically self-insulated HVT winding arrangement and capacitive voltage divider (HVD) [4.13]	88
Figure 4.4 Cross section of MSI-HVT [4.13]	89
Figure 4.5 Dependence of the energy on the EWA resistivity	93
Figure 4.6 Simplified view of EWA for use in filamentary modelling	94
Figure 4.7 Filamentary representation of EWA.....	95
Figure 4.8 Primary current, its time rate-of-change and voltage output from the spiral- strip transformer	97
Figure 4.9 Mechanism for magnetically-insulated gap.....	101
Figure 4.10 Schematic view of a 3-turn spiral-strip HVT	102

Figure 4.11 Examples of electron particle dynamics simulations in MAGIC® using the geometry of Figure 4.10 c showing (a) initial situation at $t = 0$, (b) breakdown at $I_p = 0 \text{ kA}$, $V_s = 500 \text{ kV}$, (c) magnetic insulation at $I_p = 49 \text{ kA}$, $V_s = 500 \text{ kV}$	105
Figure 4.12 Schematic drawing of spiral-strip high voltage transformer arrangement with the injection of external magnetic field	107
Figure 4.13 Axial component of magnetic flux density variation along a radial line (a) $t = 0$ (b) $t = 4.25 \mu\text{s}$	109
Figure 5.1 Nikola Tesla in his laboratory with his transformer (a photograph taken in Colorado Springs during an experiment on December 31, 1899)	111
Figure 5.2 Tesla transformer basic schematic diagram	114
Figure 5.3 HVT components in vacuum	116
Figure 5.4 Primary circuit arrangement of 1 MV HVT	117
Figure 5.5 Titan T-670 Spark Gaps	118
Figure 5.6 Secondary winding arrangement of Tesla transformer	121
Figure 5.7 Mechanism of magnetic insulation with auxiliary coil	123
Figure 5.8 Principle of magnetic insulation in Tesla transformer	125
Figure 5.9 Predicted values of first design (a) primary current (b) open secondary voltage	127
Figure 5.10 Predicted values of second design (a) primary current (b) open secondary voltage	129
Figure 5.11 Predicted values of third design (a) primary current (b) open secondary voltage	130
Figure 5.12 Predicted current provided by an external source and required for the magnetic insulation (time origin as Figure 5.1)	131
Figure 6.1 Experimental 500 kV transformer with self-magnetic insulation	133
Figure 6.2 Secondary spiral winding of transformer	134
Figure 6.3 Schematic (dimensions in mm) and photograph of a glass/Macor® spacer installed in the secondary winding	135
Figure 6.4 Ring cage shield	136
Figure 6.5 Circuit for MSI-HVT experiments	137
Figure 6.6 (a) dI_p/dt and (b) V_s measured in an experiment with early breakdown ($1 \mu\text{s}$ after closure of CS of Figure 6.5) The initial charging voltage of the capacitor bank was 15 kV	139

Figure 6.7 Slotted conductive O-strip placed onto the edge of secondary winding	140
Figure 6.8 Calibration circuit for EWA	141
Figure 6.9 Circuit current.....	142
Figure 6.10 Rate-of-change of current.....	142
Figure 6.11 Details of rate-of-change of current between ($9\ \mu s$ - $10\ \mu s$).....	143
Figure 6.12 Voltage across EWA	143
Figure 6.13 Measurement of primary inductance	145
Figure 6.14 Measurement of mutual inductance.....	145
Figure 6.15 di/dt of primary current	146
Figure 6.16 Integrated primary current.....	147
Figure 6.17 Load voltage	147
Figure 6.18 Experimental primary-current/secondary breakdown-voltage characteristics for MSI-HVT 10^{-6} Torr and 10^{-5} Torr (superscript 1 and 2, respectively) [6.1] .	148
Figure 6.19 Typical waveforms when secondary breakdown-voltage is $V_s = 480\ kV$, corresponding to $I_p = 57\ kA$. [6.1]	150
Figure 6.20 Typical waveforms when peak output voltage $V_s = 300\ kV$, corresponding to $I_p = 32\ kA$	150
Figure 6.21 Comparison between theoretical predictions for the primary-current/secondary breakdown-voltage characteristics for MSI-HVT based on Equations 4.7 and 4.10 and MAGIC [®] calculation and experimental data as in Figure 6.18 [6.1]	151
Figure 6.22 Experimental arrangement of 1 MV Tesla transformer with magnetic insulation [6.8].....	153
Figure 6.23 Experimental 1 MV Tesla transformer with magnetic insulation	154
Figure 6.24 (a) Secondary winding using 2 mm uninsulated stainless steel wire, (b) PVC spacers between the secondary turns	155
Figure 6.25 Secondary winding with polyethylene insulated conductor enabling a compact design [6.8].....	156
Figure 6.26 Outside view of the auxiliary coil [6.9].....	157
Figure 6.27 Schematic of primary main capacitor bank supply	158
Figure 6.28 Schematic of auxiliary capacitor bank supply.....	159
Figure 6.29 Schematics of experimental arrangement [6.8]	160

Figure 6.30 Magnetically insulated output voltage signal with maximum injection field current of 0.58 MA corresponding to a field of about 1 T . C_b charged to 28 kV ..162

List of Tables

Table 2.1 Relative merits and drawbacks of HVT designs for use in high-power systems	46
Table 2.2 Calculated and measured inductances for the Loughborough spiral-strip HVT54	
Table 2.3 Calculated and measured inductances for the Texas Tech University helical HVT [2.19]	55
Table 4.1 Main parameters of the simplified MSI-HVT model	104

List of symbols

a	- radius
\vec{A}	- magnetic vector potential
A_z	- axial component of the magnetic potential vector
A_θ	- circular component of the magnetic potential vector
\vec{B}	- magnetic flux density
B_{crit}	- critical field magnitude to achieve magnetic insulation
B_{min}	- minimum magnetic field required to provide the insulation
B_r	- radial component of the magnetic flux density
B_z	- axial component of the magnetic flux density
B_θ	- circular component of the magnetic flux density
B^*	- non-relativistic factor of B_{crit}
$\left\{ \frac{\partial B}{\partial t} \right\}$	- time-derivative of the magnetic flux density
c	- electromagnetic wave propagation velocity
C	- capacitance
C_n	- direct capacitance between the element and the ground
C_p	- capacitance of primary circuit
C_s	- capacitance of secondary circuit
$[C]$	- dielectric permittivity coefficient matrix
CS-	- closing switch
dA	- vectorial surface area
d_{ij}	- axial separation between the i_{th} and the j_{th} filaments
ds	- incremental sections of the filament
$\frac{d}{dt}$	- time derivative
D	- displacement vector
D_{n1}, D_{n2}	- normal components of $\{D\}$ on both sides of the interface
DC -	- direct current
e	- electron charge
E_a	- average electric field between two winding conductor layers
E_{axial}	- axial component of electrical field
E_B	- breakdown electric field
E_{max}	- maximum macroscopic field strength
E_r	- radial electrical field
E_{radial}	- radial component of electrical field
E_{total}	- total electrical field
E_{t1}, E_{t2}	- tangential components of $\{E\}$ on both sides of the interface

$E(k)$	- complete elliptic integral of the second kind
EMF	- electromotive force
EMP	- electro magnetic pulse
EWA	- exploding wire array
f	- frequency
F_i	- Field enhancement factors for each pair of turns
\vec{F}	- force
F_z	- z -component of the force in cylindrical co-ordinates
F_ρ	- ρ -component of the force in cylindrical co-ordinates
FCG	- flux-compression generators
FEA	- Finite Element Analysis
h	- field enhancement factor
h_i	- axial dimension of i_{th} filament
H	- magnetic field
\vec{H}	- magnetic field vector
H_0	- initial value of the magnetic field
H_z	- z -component of the magnetic field
HPM	- high-power microwave
HVD	- capacitive voltage divider
HVT	- high voltage transformer
i	- counter
I	- current intensity
I_{ext}	- current in external coil
I_i	- current in the i_{th} filament
I_{max}	- peak current intensity
I_p	- primary current
$I_{p\ min}$	- minimum primary current for magnetic insulation
I_s	- secondary current
$\{I_e\}$	- nodal current vector
I	- current intensity matrices
j	- counter
J_{n1}, J_{n2}	- normal components of $\{J\}$ on both sides of the interface
k	- ratio coefficient for elliptic functions
$[K]$	- electrical conductivity coefficient matrix
$K(k)$	- complete elliptic integral of the first kind
l	- length
l_{cyl}	- cylinder length
l_{eff}	- effective length
l_h	- helical coil length
l_z	- length along z -axis
L	- self inductance
L_b	- inductance of the capacitor bank

L_{ext}	- inductance of external coil
L_f	- inductance of exploding wires
L_i	- inductance of the i_{th} filament
L_l	- inductance from the load
L_p	- primary inductance
L_s	- secondary inductance
m	- mass
m_e	- electron mass
mp	- number of columns
$M_{i,j}$	- mutual inductance between the i_{th} and the j_{th} filaments
M_{p-s}	- mutual inductance between primary and secondary windings
M	- inductance matrices
MSI	- magnetic self-insulation
n	- number of turns in spiral winding
np	- number of rows
N	- total number of filaments
N_p	- number of filaments in primary winding
N_s	- number of filaments in secondary winding
$\{N\}$	- element shape function
OS	- opening switch
p	- pitch
P	- primary
q	- electric charge
q_i	- electric charge of i_{th} filament
Q	- total charge in the circuit
$\{Q_e^n\}$	- nodal charge vector
r	- radius, radial component of the cylindrical co-ordinates
r_c	- coil radius
r_{eff}	- effective radius
r_g	- radius of the circular electron orbit in the moving frame
r_i	- mean radius of i_{th} filament
r_m	- mean radius
r_p	- radius to the point P
r_s	- radius of the cross-section
r_s^k	- radius of the k_{th} turn in spiral winding
r^m	- mandrel radius of spiral winding
R	- resistance
R_b	- resistance of the capacitor bank
R_{ext}	- resistance of the external coil
R_f	- resistance of exploding wires
R_l	- resistance of the load

R_{pi}	-	filamentary resistance in primary winding
R_{si}	-	filamentary resistance in secondary winding
s	-	area
s_i	-	cross section area of i_{th} filament
S-		secondary
SG-		spark gap
t	-	time
t_r	-	rise time
t_i	-	radial dimension of i_{th} filament
T	-	temperature
TL-		flat transmission line
v	-	wave propagation velocity
v_d	-	drift velocity
vol	-	element volume
V	-	voltage
V_0	-	initial voltage of the capacitor bank
V_{break}	-	vacuum breakdown voltage
$\{V_e\}$	-	nodal electric scalar potential
V_i	-	voltage in the i_{th} filament
V	-	voltage vector matrices
W	-	energy
z	-	axial component of the cylindrical co-ordinates
z_0	-	initial axial separation distance
α	-	angle
β	-	edge effect factor
δ	-	skin depth
ε	-	small quantity
ε_0	-	vacuum electric permittivity
ε_r	-	relative electric permittivity
ε_{xx}	-	permittivity in the x-direction
$[\varepsilon]$	-	permittivity matrix
ϕ	-	conductor diameter
γ	-	Grüneisen-gama function
γ_0	-	reference value of Grüneisen-gama function
η	-	electrical resistivity
η_0	-	electrical resistivity at room temperature
$\eta(\rho_d, T)$	-	resistivity of the conductor at a density ρ_d and a temperature T
φ	-	angle
λ	-	wavelength
μ	-	magnetic permeability
μ_0	-	vacuum magnetic permeability
θ	-	angle, angular component of the cylindrical co-ordinates

ρ -	radial component of the cylindrical co-ordinates
ρ_d -	conductor density
ρ_s -	surface charge density
ρ_{xx} -	resistivity in the x-direction
$\{\rho\}$ -	charge density vector
$\{\rho_s\}$ -	surface charge density vector
σ -	electrical conductivity
σ_i -	electrical conductivity of the i_{th} filament
$[\sigma]$ -	electrical conductivity matrix
τ -	period
ω -	angular frequency
Δ -	maximum distance the electron moves away from the cathode
ψ -	electric potential

1 Introduction

Pulsed power science and technology deals with the physical and technical foundations for the production and application of high voltage pulses with very high power ($> 1 \text{ GW}$) and pulse energies ($> 1 \text{ kJ}$). A generator scheme for the production of high power electric pulses is always based on an energy store that is charged slowly at a relatively low charging power and is subsequently discharged rapidly following the activation of a switch.

The simplest form of pulse generator relies on the discharge of energy stored in either capacitors or inductors, with the main advantage of inductive storage being its smaller size. The energy density storage capability of inductors is much greater than that of capacitors, and indeed can be at least an order of magnitude more. Its main disadvantage is that the discharge circuit must contain an opening switch which has, in many circuits, to turn off large currents very quickly for the circuit to work efficiently [1.1]. Unfortunately such opening switches are difficult to construct, particularly in circuits which are required to operate repetitively. Thus pulse generators using capacitive energy storage where the switching is easier are far more common than their inductive counterparts. Using capacitive energy storage is not only simple but relatively inexpensive and the necessary switches are commonly available. However, a basic capacitive discharge circuit is limited in operation to roughly 100 kV , because of the difficulty of making reliable switches that will operate above this voltage. Other problems may arise from the physical size of the components needed to build the circuit, the high DC power supply voltages used to charge the capacitor and the difficulties in suppressing corona discharges from various parts of the circuit.

The Marx generator [1.2] is the most popular and versatile high voltage generator for many pulsed power applications, particularly when very high voltages and powers are required. As such the circuit is widely used in applications such as

lightning and EMP simulation, streamer chambers, flash X-ray and electron beam generators and high-power gas lasers.

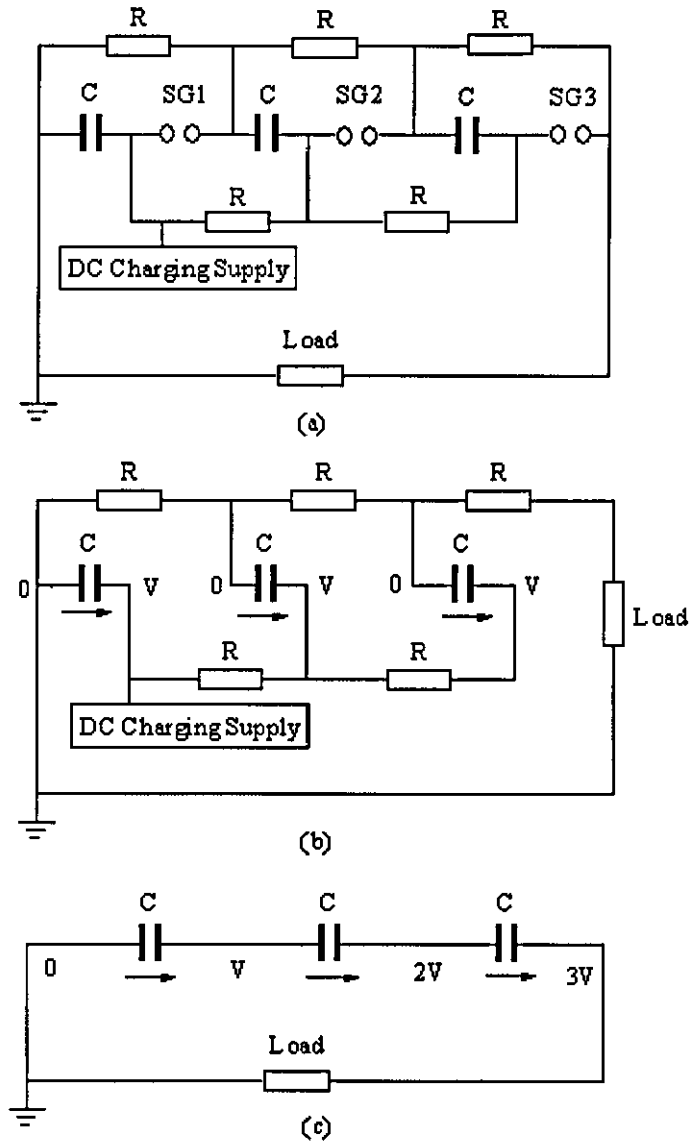


Figure 1.1 Marx generator circuit

(a) Full circuit

(b) Effective initial circuit

(c) Effective circuit during pulse

The operation circuit of a three-stage Marx generator is illustrated in Figure 1.1 Marx generators are basically very simple in theory, as a stack of n capacitors is charged in a parallel configuration to a voltage V and then rapidly discharged in series. A voltage of nV is obtained by the closure of switches between the capacitor stages, with the output voltage corresponding to the charging voltage multiplied by the number of stages. It is assumed that the values of the charging resistors are sufficiently high that they can be neglected once the circuit is operated. Major advantages of this configuration are its modularity and its ability to cover a wide range of pulse amplitudes with a typical efficiency of 85-90%, but it also has limitations in the large number of switches that is required.

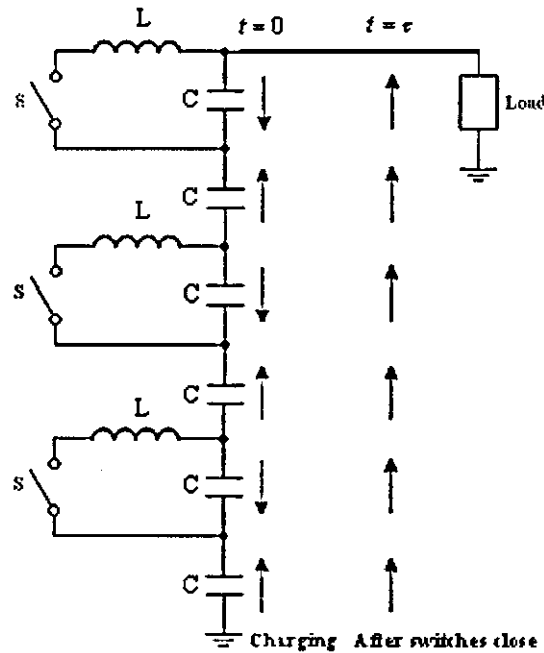


Figure 1.2 Operation circuit of a three-stage LC generator

Vector inversion generators can also be used to generate high voltage pulses. For example, the LC generator [1.3] offers a low-output-impedance alternative to the conventional Marx generator and it can be used for forming pulses with a duration of about 10 ns . The circuit shown in Figure 1.2 illustrates how the LC generator operation is based on the vector-inversion principle. The capacitors are charged to a potential V with the polarities of adjacent capacitors opposing each other at $t = 0$, as indicated by the arrows, so that the net potential across the series-connected capacitors

is zero. Once the capacitors are charged the switches are simultaneously closed, and the potential on the capacitors that are connected to the switches are consequently reversed at $t = \pi(LC)^{1/2}$. The output voltage is then $2nV$, where n is the number of stages in the generator. Triggering of the LC generator is less complicated than that of the Marx generator, as the number of switches is halved, and the output impedance can be made very low because it does not include the internal switches and their connections. Though the circuit is simple, it is difficult to turn on the switches at the same time and the 100% voltage reversal on the capacitor voltage presents a problem.

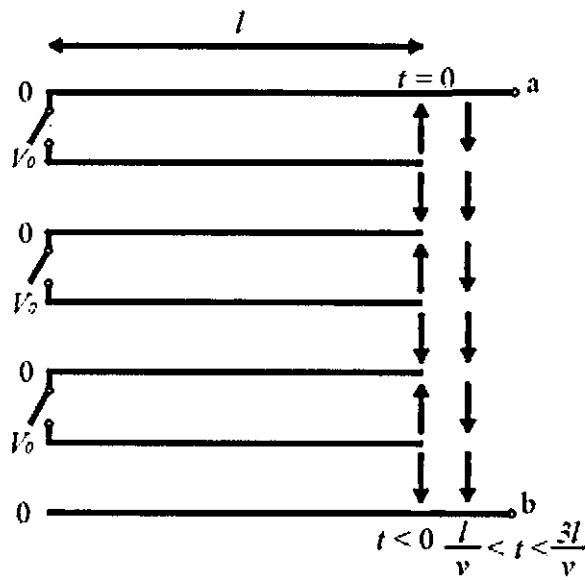


Figure 1.3 Three-stage stacked strip-line generator

The stacked strip-line generator (Figure 1.3) and stacked coaxial-line generator (Figure 1.4) are both capable of producing voltages of several megavolts with rise times of about 10^{-9} s and are easy to construct [1.4]. During charging the line at $t < 0$, the direction of the electric field is as indicated by the arrows. The three closing switches are closed at $t = 0$, and the arrows show the direction of the voltages at $l/v < t < 3l/v$. The pulse width of this stacked line is $\tau = \frac{2l}{v}$, where l is the length of the line and v is the wave propagation velocity from the source to the load. The performance of the stacked strip-line generators is limited mainly by the switch impedance and resistive losses in the lines. Figure 1.4 shows a stacked line that uses only one closing switch, with coaxial cables being used. Since the line uses only one

closing switch, it can avoid the problem of synchronization that arise in multi-switch systems.

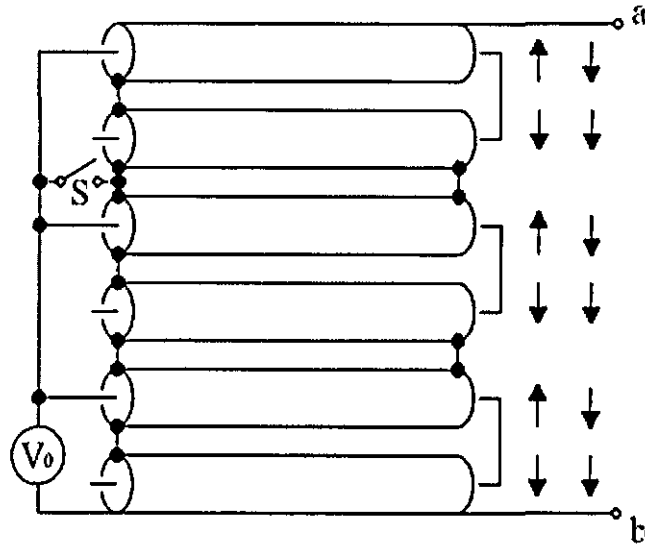


Figure 1.4 Stacked coaxial-line generator

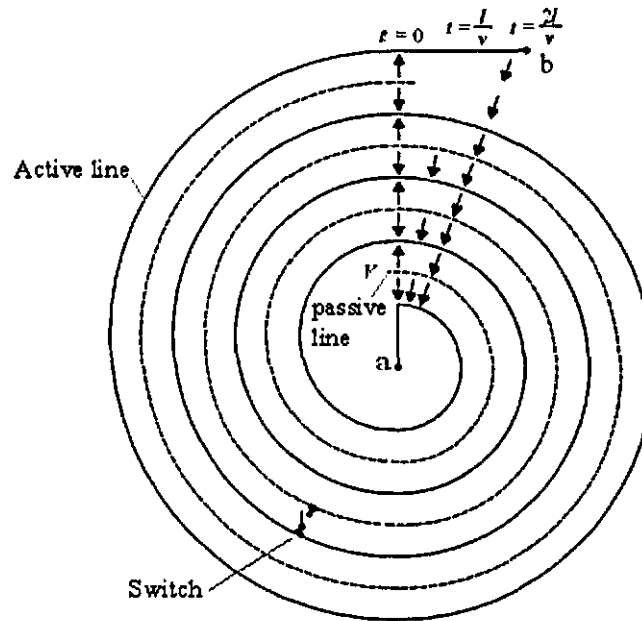


Figure 1.5 Spiral generator

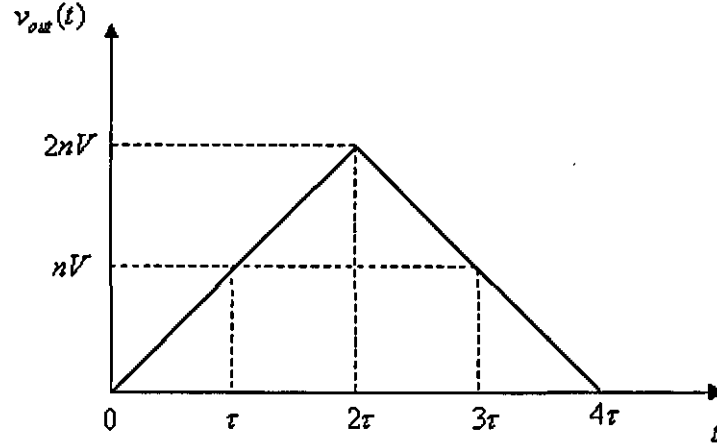


Figure 1.6 Shape of the output pulse from a spiral generator on open circuit

The spiral generator [1.5] of Figure 1.5 can produce voltages of at least 1 *MV* with greater simplicity and compactness. As shown, it contains twin spiral lines with common conductors (an active line and a passive line) with a switch at the midpoint. Initially, with the generator charged to V on the passive line, the voltage wave propagates only on the passive line, with the switch open and the directions of the electric fields in different parts of the structure opposing each other as shown by the arrows in Figure 1.5; therefore the output voltage between a and b is zero at $t = 0$ when the switch is closed. The voltage wave then propagates from the switch into the active line, and at time $t = \frac{l}{v}$ (l is half of the active line length) when it reaches the ends of the line, the potential on the active line is reduced to zero, and the voltage between the inner and outer turns builds up to $-nV$, where n is the number of turns in spiral. After the voltage waves arrive at a and b, they reflect and propagate back towards the midpoint switch, and the output voltage between a and b is therefore $2nV$ by the time $t = \frac{2l}{v}$ when the waves have returned to the switch. As the process repeats, the output voltage starts to reduce and when the voltage wave finally reaches the switch again at $t = \frac{4l}{v}$, the generator returns to its original state of $V = 0$. The waveform of the output voltage is illustrated in Figure 1.6 as:

$$V(t) = \frac{nvVt}{l} \quad (0 < t < \frac{2l}{v}) \quad (\text{Eq.1.1})$$

$$V(t) = 4nV - \frac{nvVt}{l} \quad \left(\frac{2l}{v} < t < \frac{4l}{v}\right) \quad (\text{Eq.1.2})$$

It has been pointed out that operation of the generator is based on the propagation of voltage waves around the spiral and is only applicable to generators which have a very large diameter [1.5]. The main disadvantage of the spiral generator is that the output pulse is triangular rather than rectangular, as shown in Figure 1.6. Another problem is that the generator is constructed from a pair of continuous conductors, which interconnect regions of different potential and form a closed loop with the strip line to which it is connected, causing circulating currents to flow across the loop that tend to reduce these potential differences. This particular problem limits the spiral generator from becoming a low output impedance alternative to the pulse transformer or Marx generator [1.5].

High-voltage transformers are key to many pulsed high-energy, high-power generators. They can provide an attractive financial alternative to the Marx generator for many special applications, such as charging the high-voltage pulse forming transmission lines used with high power electron or ion beam accelerators and driving portable X-ray sources and special free electron lasers. They have also been found useful for driving wide band electromagnetic radiators, all of which require the generation of a high-energy pulse of over 10 kJ, with the amplitude rising to some 500 kV or more in less than 100 ns, and then remaining almost constant for at least 1 μ s. In general, transformer systems are smaller than Marx generators, because the low-voltage capacitor bank in the primary circuit is inherently more compact and is not ordinarily operated in a tank of insulating oil. The resulting system requires substantially less floor space and does not involve separate oil storage and handling facilities. These simplifications yield a system that costs less to build and operate than a Marx system.

1.1 High voltage pulse transformer

As indicated in the previous section, a pulse transformer is a transformer specifically designed for transmitting electrical pulses which have both fast rise and fall times and in between maintaining a 'constant' amplitude sometimes up to multi-*MV*. There is a wide range of applications for such transformers, starting from the low power versions used in digital logic or telecommunications circuits, often for matching logic drivers to transmission lines. Medium power versions are found in power-control circuits such as camera flash controllers or triggering circuits. Larger power versions are employed to interface low-voltage control circuitry to the high-voltage gates of power semiconductors such as TRIACs, IGBTs, thyristors and MOSFETs. Possibly the most important technically advanced are the special purpose high-voltage pulse transformers used in the generation of high power pulses for particle accelerators, microwave sources such as klystrons or magnetrons, and other applications.

1.1.1 Advantage and development of air cored transformers

When conventional pulse transformers are to be operated at very high power levels, or with large volt-second products, it is clear that to avoid magnetic saturation large cores must be used with a large numbers of winding turns. Eventually, as the power level is raised, a point is reached where the core size required becomes impractical. To tackle this problem a different type of pulse transformer was developed by G. Rohwein [1.6-1.7] and J. C. Martin [1.8-1.9] in which there is no magnetic core and, in order to achieve good flux linkage between the primary and secondary windings, these are located very close to each other. This is usually achieved by employing conductors of thin copper foil rather than wire, arranged tightly on top of each other and with sheets of flexible plastic providing inter-turn insulation. Nonetheless, the absence of a magnetic core means that the coupling coefficients of these transformers are generally lower than those of magnetically-cored transformers, and the leakage inductance is usually a much large fraction of the

winding inductance. An important advantage of air-cored transformers is however that the frequency limitations imposed by magnetic cores are relaxed, and they can be used at frequencies of several MHz.

Air-cored transformers are usually used in a different way to the more conventional wire-wound transformers, and their predominant use is in charging capacitive loads, such as pulse-forming lines or high-voltage capacitors, to very high potentials. The energy source is usually a low voltage capacitor, that is rapidly discharged into the often single turn primary winding. They can be operated at impressively high output voltages running into the *MV* range and at energy loadings exceeding 10 *kJ*. The maximum energy loading of a given transformer depends on the width and thickness of the foil windings, with an empirical rule being that more than 1 *kJ* per centimetre width of winding can be handled.

1.1.2 Types of air cored transformers

Although many possible geometries can be envisaged for high-current high voltage transformers, only two simple arrangements are discussed here. The first and most common of these is the single-layer helical wound transformer shown in Figure 1.7 and the second is the spiral-strip type of Figure 1.8. The primary windings of either type, whether single or multiple turn, can however be designed in a variety of ways without affecting their electrical breakdown characteristics. For reasons of high-voltage insulation, the low-voltage primary winding is normally placed outside the secondary in either type of design, so that the high-voltage output of the secondary can be led out through the centre of the assembly.

The transformers differ from each other mainly in the configuration of the secondary windings. With helical transformers, a high-voltage standoff between the primary and secondary windings is ensured by an insulated space between these windings, with the space either being uniform or tapered in the longitudinal direction. When tapered, the insulation thickness increases with voltage along the length of the coils. With spiral-strip transformers, the voltage standoff is largely a function of the

radial thickness of the secondary winding, because the turns directly overlay each other. The winding stack has therefore a purely radial voltage gradient between the high-voltage inner turns and lower-voltage outer turns.

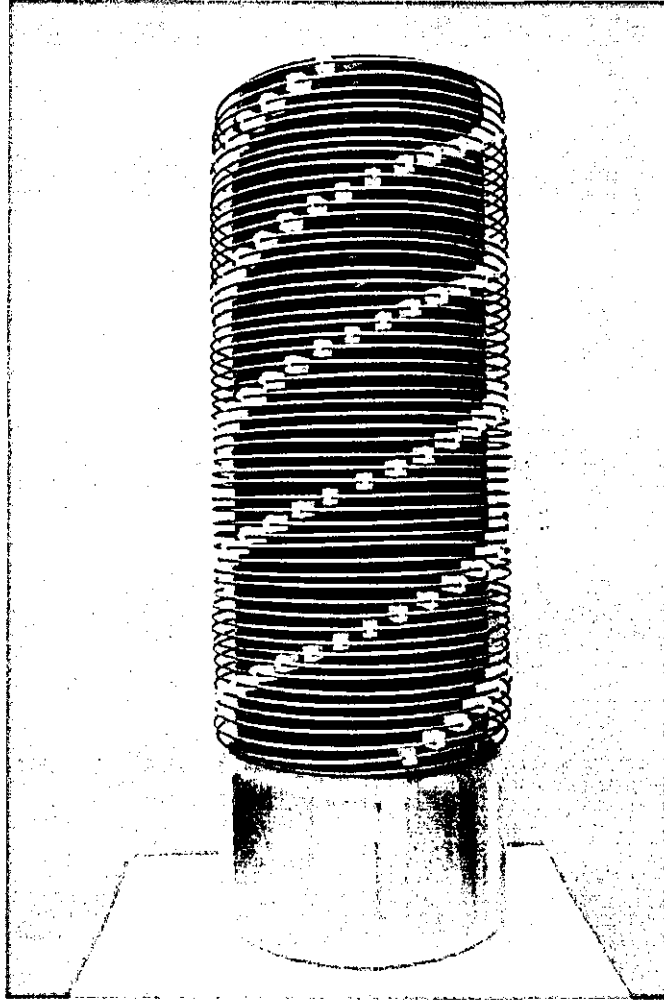


Figure 1.7 Arrangement for helical HVT developed at Loughborough University

[1.10]



Figure 1.8 Arrangement for spiral-strip HVT developed at Loughborough University with only showing secondary turns for clarity [1.11]

Each configuration has its own merits and drawbacks. For the spiral-strip type, the main advantage is that they may have a large coupling coefficient, usually larger than 0.9. They can not only be scaled for multi- MV operation but can also carry large currents ($>1\text{ MA}$) in both primary and secondary circuits. They have a coaxial output, as is required by most loads, but are relatively complex to manufacture and have a very high secondary capacitance. In comparison, helical transformers have a low coupling coefficient (<0.8), and are difficult to scale to above 1 MV . They cannot drive large currents in the secondary winding, but are widely employed because of their ease of manufacture and their ability to support an extremely high secondary/primary turns ratio. They have a low secondary winding capacitance and can easily be adapted to a coaxial geometry.

1.1.3 Transformer insulation

In the design of high-voltage pulse transformers, insulation is an essential consideration. As a minimum, it is necessary to know the maximum voltage stresses that will be reached during operation and the effective dielectric strength of the insulating materials. The types of materials most commonly adopted are the familiar plastics, oils or high-pressure gases, which are often employed in combination. Failure in one invariably leads to an overall failure.

High-pressure gas provides a flexible and reliable method of high-voltage insulation. Under high vacuum conditions, the breakdown strength is quite high. The breakdown voltage can in fact be controlled by the gas pressure and with two parallel-plate electrodes the breakdown voltage initially decreases with the barometric pressure. This is due to the fact that, as the molecular density of the air is reduced, there is a greater likelihood that a free ion can traverse the space between the electrodes without a collision. However, as the pressure is further reduced, the required voltage for breakdown increases again, because the more limited number of air molecules make ionizations more infrequent. Even a high vacuum has a limited dielectric strength however, and the transformer dimensions will need to accommodate this. A second consideration is that the surfaces need to remain clean and free from dust over long periods, so that there is no possibility of arcing or surface flashover.

The better the insulating property of a dielectric, the higher is its resistance, and the lower is the dielectric leakage loss. Oil has an extremely high resistance, so that it is not measurably leaky. Special-purpose oil is in widespread use, due in part to its relatively low cost and thermal characteristics, which are basically satisfactory for high-voltage pulse use up to more than 500 kV [1.12]. The problems that arise are most frequently because the oil can easily become contaminated by arcing. It can be extremely messy to work with, and the large volume required will cause the transformer to be extremely heavy and bulky. This is clearly unsuitable for the increasing number of applications that demand compact and very lightweight arrangements.

Recent advances in air-cored transformers using Mylar-polyethylene insulation film have been reported [1.13], which offers considerable flexibility through its chemical, thermal and physical properties. One of the most outstanding of these is its high insulation resistance over a wide temperature range and, since it also has a very high breakdown voltage stresses, Mylar can be used to provide a very compact assembly. Unfortunately, the techniques involved are difficult to extend to voltages above about 500 *kV*.

The last two decades have seen enormous advances in high-voltage, fast-pulse techniques, due mainly to the introduction of the revolutionary new technique of magnetic insulation, which diverts the electron flow in vacuum (that would otherwise be responsible for an electrical breakdown in a device) by means of the Lorenz force arising from the interaction of the electrons with a magnetic field. If the magnetic field is produced by the current in the device itself, magnetic self-insulation is obtained.

Magnetic insulation has provided the basis for the development of many of the modern components that are now extensively used in large pulsed-power projects, such as transmission lines [1.14], ion diodes [1.15], electron beams [1.16], magnetrons [1.17] and plasma opening switches [1.18]. However, the technique is not so far well developed in high-power transformers, because of a number of apparently insurmountably difficulties.

Winterberg [1.19] proposed the first magnetically insulated transformers in 1970; but his idea was not translated into a practical device because of a number of significant issues. No working transformer was in fact reported prior to the Loughborough helical secondary design of 2002 [1.20], which demonstrated that a magnetically insulated transformer is possible, although the levels of voltage and power were limited and the topology was greatly simplified. The present work investigates the extension of both of these features to the levels required in most pulse power applications and in a more realistic conductor arrangement, firstly by means of magnetic self insulation and secondly by means of magnetic insulation.

1.2 Magnetic insulation technique

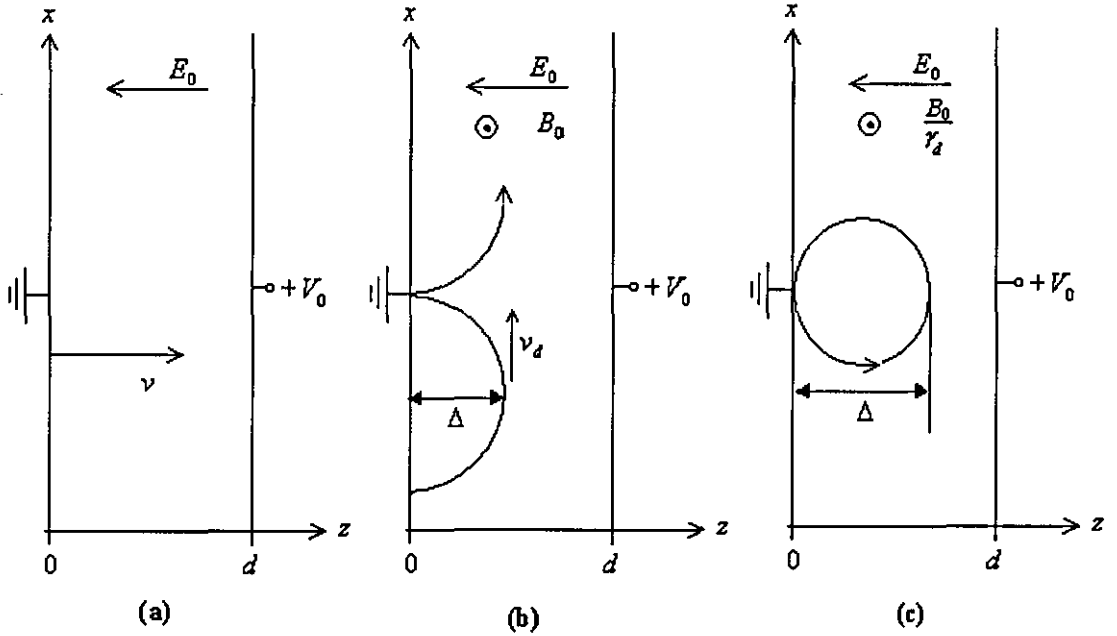


Figure 1.9 Magnetic insulation principle with vector B parallel to plates and orthogonal to electric field showing (a) $B = 0$ and (b) scalloped drift orbit viewed in the stationary frame (c) drift orbit viewed in a frame of reference moving at the electron drift velocity

A high electrical stress ($>100 \text{ kV/cm}$) can cause electron emission from a cathode, with the electrons being accelerated to the anode by the electric field and leading to electrical breakdown (flashover) between cathode-anode gaps. Magnetic insulation can prevent the motion of electrons across a gap with a high-applied voltage, as illustrated by Figure 1.9. With attention limited to only single electron motion, neglecting the contribution of free electrons to the field, electrons emerge from the cathode at $z = 0$. The anode at $z = d$ has a bias voltage V_0 , so that the electric field is:

$$E_z = -E_0 = -(V_0/d) \quad (\text{Eq.1.3})$$

For magnetic insulation, a uniform magnetic field is applied in the y direction:

$$B_y = B_0 \quad (\text{Eq.1.4})$$

Figure 1.9 (a) illustrates the trajectory of an electron emerging from the cathode with zero kinetic energy in the absence of a magnetic field. The electric field attracts the particle toward the anode and leads to electrical breakdown. If however a magnetic field is applied in a direction orthogonal to the electric field, once the electron gains velocity in the z direction its orbit is bent by the magnetic field in the x direction. Ultimately, the electron returns to the cathode. If the electron is not absorbed, it follows the scalloped orbit shown in Figure 1.9 (b). Note that the motion in the z direction is periodic, and the electrons have a cumulative displacement along the x direction. This type of motion is called particle drift.

If the maximum distance the electron moves away from the cathode is Δ , this is controlled by the magnitude of the magnetic field, which must exceed a minimum value if the electron flow is to be prevented from making contact with the anode. When Δ is less than the anode to cathode separation, electrons cannot cross to the anode and the gap is magnetically insulated. Moreover, the transverse magnetic field can inhibit the motion of cathode and anode generated plasmas, which, if left to themselves, move across the cathode-anode gap, causing undesirable closure by an electrical shorting of the system.

Both Δ and the drift velocity v_d can be found in terms of B_0 and E_0 by making a relativistic transformation to a frame of reference that moves with the velocity v_d in the positive x direction. Equations 1.5 and 1.6 present the electric and magnetic fields in the moving frame for given quantities in the stationary frame [1.21].

$$E_z' = \gamma_d(E_z + v_d B_y) \quad (\text{Eq.1.5})$$

$$B_y' = \gamma_d(B_y + v_d E_z / c^2) \quad (\text{Eq.1.6})$$

where primed symbols indicate quantities measured in the moving frame. The quantity γ_d is a function of the drift velocity, thus

$$\gamma_d = \left[\frac{1}{1 - (v_d/c)^2} \right]^{1/2} \quad (\text{Eq.1.7})$$

Equation 1.5 shows that the electric field vanishes in the moving frame if the transformation velocity equals

$$v_d = E_0/B_0 \quad (\text{Eq. 1.8})$$

In this case the electron motion is a simple gyration in the transformer magnetic field as shown in Figure 1.9 (c). This velocity is called the $E \times B$ drift velocity and its direction is parallel to the cross product of field vectors. Note that if $E_0 \geq cB_0$ then the velocity exceeds the speed of light and the transformation is invalid.

When $E_0 < cB_0$, the quantity Δ can be calculated by applying the following facts:

1. Equation 1.6 implies that the magnitude of the magnetic field in the moving frame is lower by a factor of γ , with $B_y' = B_0/\gamma$.
2. The electron follows a circular gyration orbit in a uniform magnetic field.
3. At the point of contact with the cathode, an electron has zero velocity in the stationary frame; it has therefore a velocity $v = -v_d x$ in the moving frame.

The radius of the circular electron orbit in the moving frame is

$$r_g = \frac{\gamma m_0 |v|}{e B_0 / \gamma} = \frac{\gamma^2 m_0 v}{e B} \quad (\text{Eq.1.9})$$

The maximum excursion distance from the cathode is twice the gyro radius,

$$\Delta = 2r_g \quad (\text{Eq.1.10})$$

The criterion for magnetic insulation is that $\Delta \leq d$. The critical magnetic field B_{crit} is the field magnitude that gives $d = \Delta$. For a given electric field, a magnetic field greater than B_{crit} prevents electrons from crossing to the anode. B_{crit} can be obtained by combining Equations 1.3, 1.7, 1.9 and 1.10. Thus

$$B_{crit} = B^* \left[1 + \frac{eV_0}{2m_e c^2} \right]^{1/2} \quad (\text{Eq.1.11})$$

where

$$B^* = \frac{1}{d} \left[\frac{2V_0 m_0}{e} \right]^{1/2} \quad (\text{Eq.1.12})$$

Equation 1.11 is in terms of a non-relativistic factor B^* and a relativistic correction term. The relativistic term is significant when $V_0 \geq m_0 c^2 / e = 0.511 \text{ MV}$.

In cylindrical geometry the insulation criterion is given by Equation 1.12 with d replaced by the effective gap $d_{eff} = (r_a^2 - r_c^2) / 2r_a$, where r_c and r_a are the cathode and anode radii, respectively ($r_c < r_a$), and $d_{eff} = (r_a^2 - r_c^2) / 2r_c$ when the cathode radii is the larger. The critical magnetic field as a function of the voltage for a 10 mm gap is shown in Figure 1.10, which provides a comparison between the relativistic theory and the non-relativistic treatment, and confirms that quite moderate magnetic fields can insulate high-voltage gaps.

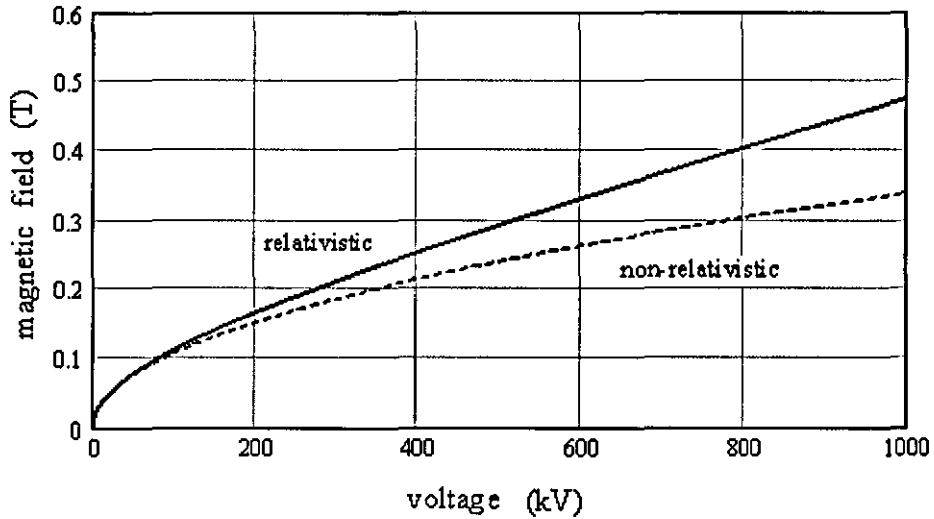


Figure 1.10 Critical magnetic field strength for magnetic insulation versus voltage between anode-cathode gap ($d = 10 \text{ mm}$)

1.3 Thesis objectives

The present research is concerned with novel insulation techniques for high-voltage pulse transformers. Two novel arrangements are presented that overcome the problems associated with the earlier designs. The resulting arrangement is both lightweight and compact in comparison with any alternative presently available, and opens the way to multi-MV level self-insulation transformer.

The two transformer arrangements considered are:

- a) A 500 kV transformer with self-magnetic insulation [1.11]

The transformer has a single turn-primary surrounding an eight-turn secondary spiral-strip winding. The secondary winding was designed with a variable pitch to achieve an approximately even average electric field strength distribution over the

windings. The primary is powered by a capacitor bank in which an exploding wire array is used as an opening switch to generate the high dI/dt which enables the secondary to produce an output voltage of 500 kV, and the magnetic field induced by the primary current is the source of magnetic insulation.

b) The second is a 1 MV Tesla transformer with external magnetic insulation [1.10].

A main capacitor bank is connected to the single-turn primary winding through a spark gap switch and a short flat transmission line. The secondary winding is a 50-turn helical coil, connected to another inductively-coupled damped resonant circuit, to form a Tesla transformer. One internal conductor, powered by an auxiliary capacitor bank, produces the required magnetic field and, as a demonstration of the field strength that is necessary, it will be assumed that the transformer is required to generate a secondary voltage of 1.5 MV.

Both 2-dimensional filamentary modelling and ANSYS software are used in the design and in providing detailed performance predictions of the transformer characteristics. The two prototype transformers are believed to be the first working high-power magnetically insulated transformers in the world, and they have provided reliable experimental data for verification of the theoretical predictions. The experimental work was supported by EPSRC and MoD through their Joint Grant Scheme (Research Grant GR/T01044/01).

Many major pulsed power laboratories worldwide are devoting much effort to the development of power sources for applications such as the production of powerful X-ray, electron, ion and microwave generators, with the magnetically insulated transformer being seen as a key element leading towards a very lightweight and compact system. Beneficiaries from the research will include research groups engaged in fundamental experimentation in areas such as high-energy particle accelerators, magneto and electro optical solid-state physics, plasma physics (fusion) and astrophysics. Once the technology is proven, it can be adopted in other important

research areas relating to medicine, electromagnetic metal forming and the aerospace industry.

1.4 Thesis organisation

Chapter 2 of the thesis introduces filamentary modelling, which takes magnetic diffusion fully into account and enables the resistances and self and mutual inductances of the transformer windings that are effective under fast transient conditions to be calculated. The general formulation and governing equations for the electrical properties of θ -current circuits and z-current circuits are described in detail. Besides a detailed description of the solutions applied to a number of electromagnetic issues such as inductance calculation, skin and proximity effect, magnetic field, electromagnetic forces, capacitance calculation, electric field etc, two-dimensional models for spiral-strip and helical HVTs are presented and the models are benchmarked with experiment results.

In Chapter 3, Finite Element Analysis is used to analyze the electric field and potential distribution in both spiral-strip and helical transformers, which is very important for the design and development of high voltage equipment and electrical insulation. Results from an extensive study of field enhancement at the winding edge are presented and discussed, to find an optimum design parameter, and a simple technique is introduced for grading the electric field in a spiral-strip transformer.

Chapter 4 describes the detailed design of a spiral-strip wound 500 kV transformer that uses self-magnetic insulation. A description is given of the novel technique used to grade the electric fields internal to the secondary winding and so prevent an electrical breakdown. Two-dimensional filamentary modelling and ANSYS finite element software are both used in the design and prediction of the overall performance.

Chapter 5 describes the arrangement of a 1 *MV* Tesla transformer with external magnetic insulation. Again both two-dimensional filamentary modelling and ANSYS finite element software are used in the design. The resulting arrangement is both lightweight and compact in comparison with any alternative presently available and opens the way to multi *MV* level self-insulating transformers.

Chapter 6 summarizes the large numbers of experiments carried out to verify the designs of Chapters 4 and 5. Details of the construction of both 500 *kV* spiral-strip magnetic self-insulation transformer and 1 *MV* Tesla transformer with magnetic insulation are given. Experiment results are presented, analyzed and compared with predictions made by numerical modelling.

Conclusions and suggestions for future work are given in Chapter 7.

2 Filamentary modelling

2.1 Introduction to filamentary modelling

Pulsed power physics and technology has become increasingly important in a wide range of high-power applications, which might be either repetitively pulsed or single shot. In either case it is essential to know the response of the electrical conductors that comprise the system network, in order that any potential damage can be assessed. The currents involved may be up to several MA, and even during the very short time scales involved these may give rise to dangerous movement of the conductors, together with melting and possible vaporization and plasma formation. A computer code is therefore required that includes as complete a description as possible of the basic physics that is involved, and which can be used to investigate the multi-dimensional parameter space of the situation, to establish the optimum conditions, to interpret the experimental data, and to indicate how the system efficiency can be improved. Without such a reliable code, far more experimentation would be needed, and to obtain the optimized design for the overall system would require a long, tedious and costly process.

When electrical pulses are present in an electromagnetic field, the transient behaviour of both the electric currents and magnetic fields are fully described by Maxwell's Equations. For low-frequency problems these can be reduced to the diffusion equations, which are commonly used to describe the classical physics of electric current and magnetic field penetration into a conductor. Depending on the details of the problem under investigation, the diffusion equation can be solved using several different methods with judiciously selected boundary conditions. Magnetohydrodynamic modelling is the conventional technique. Unfortunately it is a very demanding task to apply this technique to a complex arrangement or to determine the ohmic heating and the electromagnetic forces. In the past such considerations have

led to the development of extremely complex numerical codes, run on large computers in laboratories developing nuclear weaponry. On occasions, the costs involved have even been so high as to exceed the cost of an actual experiment. Alternative codes that employ finite element analysis (FEA) are available commercially, and are used currently at Loughborough to solve difficult multi-physics problems [2.1], but they are again invariably complex and costly.

Filamentary modelling is a simple but accurate and general-purpose numerical technique that enables a full description of electromagnetic, thermal and dynamic interactions to be included in a model, while still preserving considerable mathematical simplicity. It provides a very useful tool when more advanced codes are either unavailable or too costly, or when fast preliminary designs of complex implosion machines are required. It owes much to the work reported previously by the Institute of Solid State Physics, Japan [2.2-2.3] and developed at Loughborough University [2.4-2.9], with a long history of progressively more complicated and refined theoretical models, all attempting to reproduce as accurate as possible reliable experimental data.

In essence, filamentary modelling is a systematic numerical procedure for solving the assembly of ordinary differential equations that arises in, for example, electromagnetic problems. It is applicable to systems in which the temporal and spatial variations of the current distribution carry the most important information about the system. Once this distribution has been established, the performance of the system can be specified. In its basic form, the filamentary approach originated with Maxwell's inductance calculation [2.10]. In recent times, developed forms have been used in modelling both electromagnetic launchers [2.11] and ultrahigh magnetic field generators [2.3]. It has also been demonstrated that the method is able very accurately to calculate both skin [2.12] and proximity effects [2.4]. Loughborough has recently introduced a number of novel features into the modelling, mostly related to the fast dynamics of imploding/exploding structures, and has successfully applied the technique in a very wide range of pulsed power applications, including explosively driven flux-compression generators [2.5], multi and single-turn inductive launchers [2.6-2.7], and electromagnetic flux-compression [2.8]. The technique has also been

used to provide an improved understanding of a novel electromagnetic technique developed for remote activation across thick metallic shields [2.9].

2.2 General formulation

A filamentary model can be produced by following a well-defined process. Initially, the given assembly of conductors is divided into an assembly of filaments in the direction of the current paths through them, once these are known. The filaments must be sufficiently small for the current distribution in their cross sections to be regarded as uniform and, as a rule of thumb, the dimensions will be much less than the equivalent skin depth. The number of filaments required to describe accurately their properties under transient conditions is obtained by calculating the parameters for a relatively small number of filaments, and then repeating the calculations for a progressively increased number, until the differences between successive calculations are less than say 1%. A practical example is discussed later.

Once the replacement of the solid conductors by the current filaments is complete, the ohmic resistance of each filament is determined from its cross-sectional area, length and temperature dependent resistivity. By assuming a uniform current distribution across the cross-section of the filaments, the self-inductances can readily be calculated from well-known formulae, as can the mutual inductance between every possible pair of filaments. Thereby the electromagnetic problem is reduced to a simple circuit problem, in which the solid conductors are represented by an assembly of current filaments. The currents in each branch are defined as state variables, and the circuit equations are written as a set of linear first order differential equations that have to be solved for the circuit currents. A typical set of equations will appear in matrix form as:

$$\frac{d}{dt} \begin{bmatrix} L_1 & M_{1,2} & \cdots & M_{1,N} \\ M_{2,1} & L_2 & \cdots & M_{2,N} \\ \vdots & \vdots & \ddots & \vdots \\ M_{N,1} & M_{N,2} & \cdots & L_N \end{bmatrix} \cdot \begin{bmatrix} I_1 \\ I_2 \\ \vdots \\ I_N \end{bmatrix} = \begin{bmatrix} V_1 \\ V_2 \\ \vdots \\ V_N \end{bmatrix} \quad (\text{Eq.2.1})$$

where N is the number of filaments, $\frac{d}{dt}$ is the time derivative, I_i ($i=1..N$) is the current in the i_{th} filament, V_i ($i=1..N$) is the complete inductive voltage term in the circuit containing the i_{th} filament and $M_{i,j}$ ($i,j=1..N$) is the mutual inductance between the i_{th} and the j_{th} filaments. When $i=j$, $M_{i,j}$ become L_i , the self-inductance of the i_{th} filament.

Equation 2.1 can be written in the abbreviated form:

$$\frac{d}{dt} \left(\sum_{j=1}^N M_{i,j} I_j \right) = V_i, (i=1..N) \quad (\text{Eq.2.2})$$

or even more compactly as:

$$\frac{d}{dt} (\mathbf{M} \cdot \mathbf{I}) = \mathbf{V} \quad (\text{Eq.2.3})$$

in which \mathbf{M} , \mathbf{I} , \mathbf{V} are the inductance, current and voltage matrices. Any electromagnetic problem will be either dynamic or static, and in the most general dynamic case Equation 2.3 can be expressed as:

$$\mathbf{M} \cdot \frac{d\mathbf{I}}{dt} + \frac{d\mathbf{M}}{dt} \cdot \mathbf{I} = \mathbf{V} \quad (\text{Eq.2.4})$$

while for the simpler static problem, in which the mutual inductance matrix is time invariant, it takes the reduced form:

$$\mathbf{M} \cdot \frac{d\mathbf{I}}{dt} = \mathbf{V} \quad (\text{Eq.2.5})$$

The set of first-order differential equations that corresponds to the filamentary circuit model is solved using numerical ordinary differential equation solvers such as the Runge-Kutta or block iterative Newton methods, with the filamentary currents thus calculated providing the current distribution in the conductors. If some material properties and discretization geometries create circuit branches with different time scales, causing the differential equations to be stiff and difficult to solve using the Runge-Kutta integrator, the Gear method can be used to overcome the stiffness problem.

Any non-linear considerations that arise in the numerical modelling process are normally dealt with by transforming the corresponding non-linear equations into equivalent linear equations. Finally, from the knowledge of the filamentary currents, the magnetic and electrical field distribution, the electromagnetic forces between filaments, the energy deposited in the conductors, the temperature distribution and so on can all be obtained.

Most of the EM devices encountered in pulsed-power work have rotational symmetry about one axis, which is conventionally termed axial symmetry. Because of this fortunate situation, the models developed in this thesis are restricted to conductor arrangements capable of being defined in cylindrical co-ordinates (ρ, z, θ) , with symmetry about the z -axis. Therefore, in the most general case, the effect of an arbitrary current path through the symmetrical conductors can be defined in terms of a combination of z and θ currents.

In the thesis, specific approaches are described for the current path followed by both z and θ currents. It is shown that, in the case of z (axial) currents, integrals are obtained that can be readily evaluated, leading to analytical solutions for the corresponding resistances and inductances.

However, an exact analytical solution is extremely difficult to obtain for the θ -currents, although a very good solution can be obtained by the numerical evaluation of a system of differential equations.

2.3 Electrical properties of θ -current circuits

Circular coils are widely used in various electromagnetic applications such as coil guns, tubular linear motors, single-layer coils, coils with rectangular cross section, current reactors, and antennas. No matter if it is single-layer or multi-layer, helical or spiral, cylinder or conical, all can be divided into circular rings, and the problem is to solve a set of ordinary differential equations. In the following section, consideration is given to the electric and magnetic parameters of conductors with θ -current, i.e. circular circuit elements in the form of rings or loops.

2.3.1 Magnetic vector potential of a circular current loop

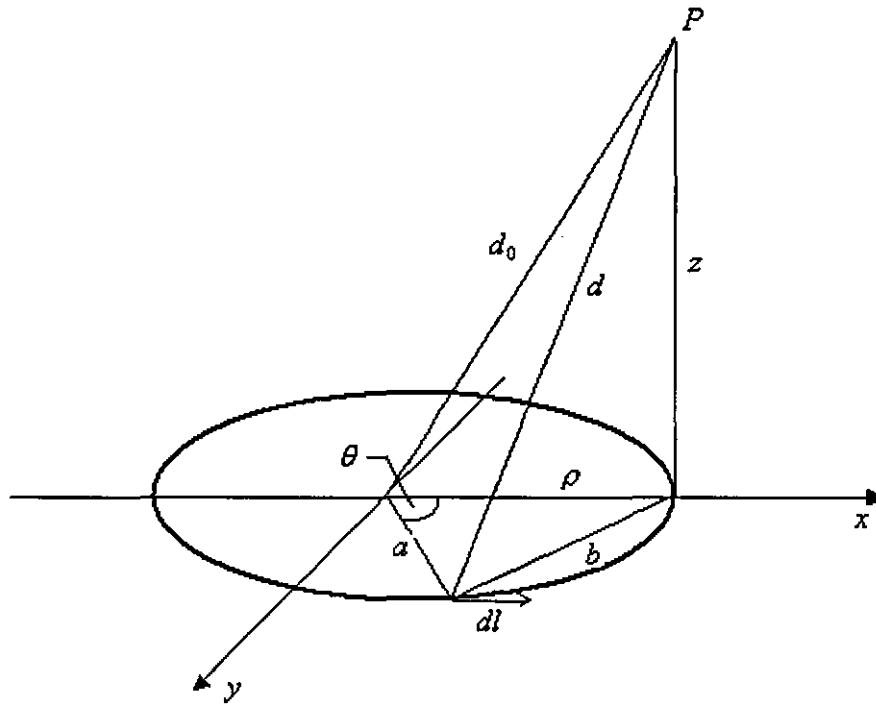


Figure 2.1 Circular current loop

To determine the properties of an axially symmetric system, the magnetic vector potential \bar{A} is calculated at a point P , remote from the circular current loop shown in Figure 2.1 as [2.13]

$$A_\theta(a, b, z) = \frac{\mu_0 I}{\pi k} \sqrt{\frac{a}{b}} \left[\left(1 - \frac{1}{2}k^2\right) K(k) - E(k) \right] \quad (\text{Eq.2.6})$$

where

$$k^2 = \frac{4ab}{(a+b)^2 + z^2} \quad (\text{Eq.2.7})$$

and $K(k)$ is the complete elliptic integral of the first kind, given in [2.14] as:

$$K(k) = \int_0^{\pi/2} \frac{d\varphi}{\sqrt{1 - k^2 \sin^2 \varphi}} \quad (\text{Eq.2.8})$$

and $E(k)$ is the complete elliptic integral of the second kind, given in [2.14] as:

$$E(k) = \int_0^{\pi/2} \sqrt{1 - k^2 \sin^2 \varphi} \cdot d\varphi \quad (\text{Eq.2.9})$$

Values for both the above elliptic integrals are available in standard tables. Alternatively, they can be calculated using either numerical integration or, for faster results, specially designed numerical procedures [2.15].

2.3.2 Magnetic flux density of a circular current loop

Since the relation between magnetic flux density \bar{B} and magnetic vector potential \bar{A} is: $\bar{B} = \nabla \times \bar{A}$, the magnetic flux density can be specified by the two equations [2.13]:

$$B_i^\rho = \frac{\mu_0 I_l}{2\pi} \frac{z}{\rho[(r_l + \rho)^2 + z^2]^{1/2}} \left[-K + \frac{(r_l)^2 + \rho^2 + z^2}{(r_l - \rho)^2 + z^2} E \right] \quad (\text{Eq.2.10})$$

$$B_i^z = \frac{\mu_0 I_l}{2\pi} \frac{1}{[(r_l + \rho)^2 + z^2]^{1/2}} \left[K + \frac{(r_l)^2 - \rho^2 - z^2}{(r_l - \rho)^2 + z^2} E \right] \quad (\text{Eq.2.11})$$

since a circular loop will produce no θ -directed component of magnetic flux density.

2.3.3 Forces between two parallel coaxial loops

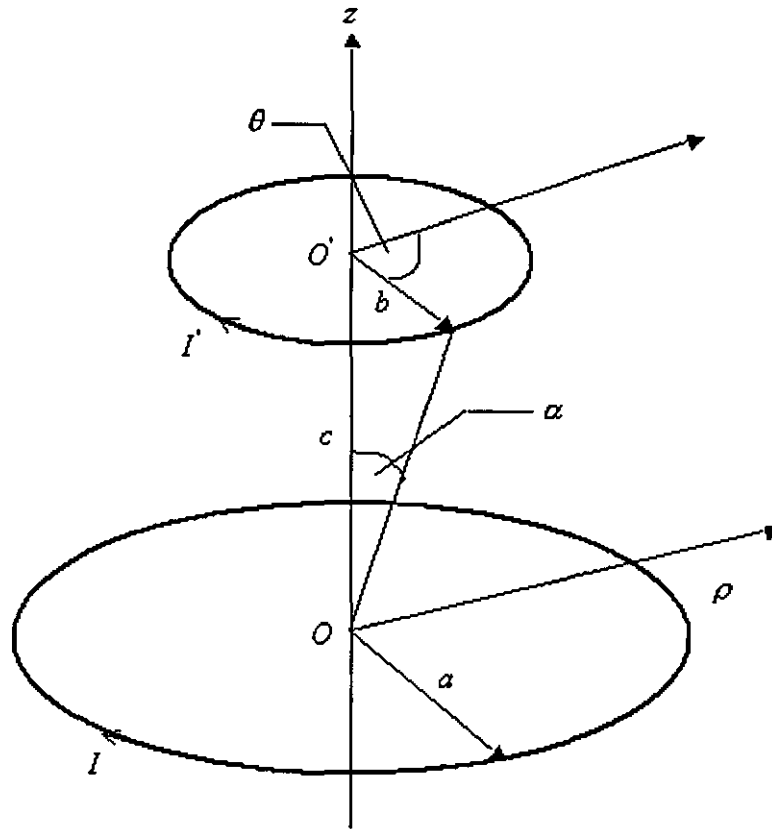


Figure 2.2 Forces between two parallel coaxial loops

The magnetic forces acting on a small loop of wire in a magnetic field are exactly like those acting on an electric dipole in an electric field, and any electrical

circuit may be considered as a mesh of such loops. Figure 2.2 shows two parallel coaxial loops of wire of radii a and b , carrying currents I and I' . The mutual forces can be specified as [2.13]:

$$F_{i,j}^{\rho} = 2\pi r_i I_i B_j^z \quad (\text{Eq.2.12})$$

$$F_{i,j}^z = 2\pi r_i I_i B_j^{\rho} \quad (\text{Eq.2.13})$$

Substituting into Equations 2.12 and 2.13 from Equations 2.10 and 2.11 leads to :

$$F_{\rho}(a,b,c) = -\frac{\mu_0 I \cdot I' b}{\sqrt{(a+b)^2 + c^2}} \left[K(k) + \frac{a^2 - b^2 - c^2}{(a-b)^2 + c^2} E(k) \right] \quad (\text{Eq.2.14})$$

$$F_z(a,b,c) = \frac{\mu_0 I \cdot I' c}{\sqrt{(a+b)^2 + c^2}} \left[-K(k) + \frac{a^2 + b^2 + c^2}{(a-b)^2 + c^2} E(k) \right] \quad (\text{Eq.2.15})$$

2.3.4 Mutual inductance of two parallel and coaxial circular loops

Because of the relatively low rise-time of the currents occurring in the pulsed power applications considered in this thesis, it will be acceptable to use only simple low frequency formulae when calculating both self and mutual inductances.

When the filamentary cross section is neglected, the mutual inductance between two coaxial filaments having radii r_i and r_j and an axial separation d_{ij} can be calculated from Neumann's formula [2.13]:

$$M = \frac{\mu_0}{4\pi} \iint \frac{\overline{ds} \cdot \overline{ds'}}{r} \quad (\text{Eq.2.16})$$

where ds and ds' are incremental sections of the filaments, the dot implies a scalar product, and r is the distance between the filaments. The exact integral is obtained from an adequate parameterization of the geometry of the filaments as [2.13]

$$M_{ij} = 2\mu_0 k^{-1} (ab)^{1/2} \left[\left(1 - \frac{1}{2}k^2\right) K(k) - E(k) \right] \quad (\text{Eq.2.17})$$

where k , K and E are defined by Equations 2.7, 2.8 and 2.9 respectively,

Although Equation 2.15 was developed for conductors of negligible cross-sectional area, it nevertheless provides a good approximation in many other cases when the mean radii of the loops are used in the calculations.

2.3.5 Self inductance of circular loop

2.3.5.1 Finite rectangular cross-section conductors

At low frequency, the self-inductance of a ring of rectangular cross-section is given to a very good approximation by [2.16]

$$L_i = \mu_0 r_i \left[\ln(8r_i / (h_i + t_i)) - 0.5 \right] \quad (\text{Eq.2.18})$$

where r_i is the mean radius of the ring, h_i and t_i are respectively the axial and radial dimensions of the cross section and $r_i \gg h_i + t_i$.

2.3.5.2 Finite circular cross-section conductors

The self-inductance of a ring of circular cross-section can be taken as [2.16]:

$$L(r_m, r_s) = \mu_0 r_m \left[\ln \frac{8r_m}{r_s} - \frac{7}{4} + \frac{r_s^2}{8r_m^2} \left(\ln \frac{8r_m}{r_s} + \frac{1}{3} \right) \right] \quad (\text{Eq.2.19})$$

where r_m is the mean radius, r_s is the radius of the cross-section, and terms of order $(\frac{r_s}{r_m})^4$ and above are neglected. For $r_m \gg r_s$, Equation 2.16 may be reduced to:

$$L(r_m, r_s) = \mu_0 r_m \left(\ln \frac{8r_m}{r_s} - \frac{7}{4} \right) \quad (\text{Eq.2.20})$$

2.3.5.3 Finite ribbon cross-section conductors

When $h_i \gg t_i$, more accurate expressions are available. For a circular ribbon with a radius r_i and an axial length $2t$, under the approximation $t \ll a$, the self-inductance can be expressed as [2.3]

$$L_i = \mu_0 r_i (0.3862944 + 0.1730840q^2 - \ln q - 0.2538683q^2 \ln q) \quad (\text{Eq.2.21})$$

where

$$q = t / 2r_i \quad (\text{Eq.2.22})$$

2.3.6 Resistance

Here we only discuss the resistance, as in a DC calculation. This implies that is necessary to investigate the relationship:

$$R = \eta(\rho_d, T) \frac{l}{S} = \frac{2\pi r}{S} \eta(\rho_d, T) \quad (\text{Eq.2.23})$$

where r is the mean radius of the circular loop of length l , S is its conductor cross-sectional area and $\eta(\rho_d, T)$ is the resistivity of the conductor at a density ρ_d and a temperature T .

2.4 Electrical properties of z-current circuits

For the z -current circuits, consider the case of a typical simple rail gun. Because of symmetry, both the upper and lower rails can be partitioned in the same manner into a number of filaments of finite cross-sectional areas such that each filament in the upper rail has a corresponding one in the lower rail as shown in Figure 2.3. The following sections investigate the magnetic and electrical properties of conductors carrying a z -current distribution, i.e. cylindrical and conical circuits, with stationary magnetic fields.

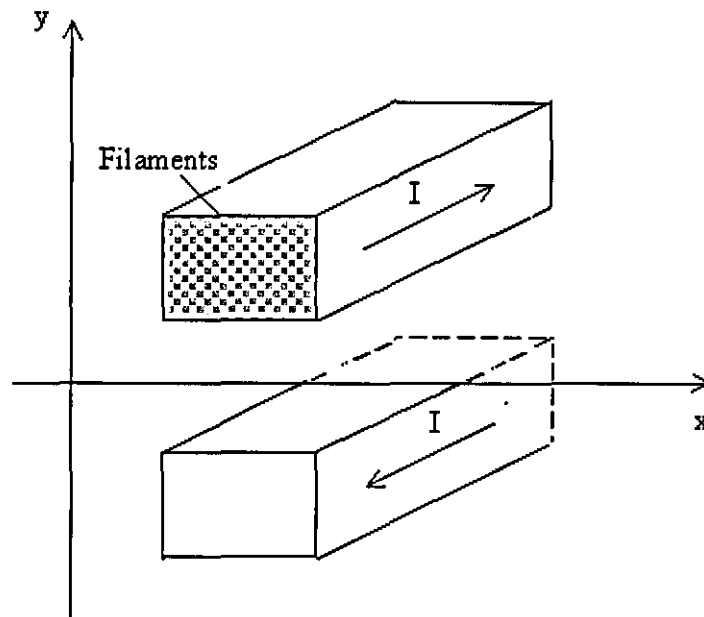


Figure 2.3 Hypothetical rail gun configuration used for filamentary modelling

2.4.1 Magnetic flux density of straight conductor in z -current circuits

As a consequence of the assumption of a stationary magnetic field, the current in the situation investigated below is assumed to be uniformly distributed throughout the cross-sectional area of the conductor.

The flux density \bar{B} produced by a long straight circular conductor of radius r_0 will be determined. To do this, a closed circular path of radius r is selected, at right angles to the conductor and with its centre on the axis of the conductor. Applying Ampere's circuital law, and performing the necessary integration, leads to the result for the circular component of the magnetic flux density B_θ as:

$$B_\theta(r) = \begin{cases} \frac{\mu_0}{2\pi} \frac{r}{r_0^2} I, & r \leq r_0 \\ \frac{\mu_0}{2\pi} \frac{I}{r}, & r > r_0 \end{cases} \quad (\text{Eq.2.24})$$

The radial component B_r of \bar{B} can be obtained by integration of \bar{B} over the surface of a Gaussian cylinder of radius r . Since no current flows through this surface area, the radial component B_r must always be zero.

2.4.2 Forces between two parallel filaments

For two parallel straight wires distance a apart, and carrying currents I and I' , the repulsive force per unit length is

$$F = \pm \frac{\mu_0 II'}{2\pi a} \quad (\text{Eq.2.25})$$

The positive sign is taken when I and I' are in opposite directions, and the negative sign when they are in the same direction.

2.4.3 Mutual inductance of two parallel filaments

To calculate the mutual inductance between two parallel filaments of finite length, it is assumed that the filaments can be regarded as having zero cross-sectional area, regardless of whether they belong to the same or to different loops. With reference to Figure 2.2, the mutual inductance [2.16] is then

$$M = \frac{\mu}{2\pi} I \left[\ln\left(\frac{l}{d} + \sqrt{1 + \frac{l^2}{d^2}}\right) - \sqrt{1 + \frac{d^2}{l^2}} + \frac{d}{l} \right] \quad (\text{Eq.2.26})$$

2.4.4 Self inductance of coaxial structures

The self-inductance of a system is defined as the flux linkages produced with the system by a unit current. For the self-inductance of a single filament of finite length and of circular cross section of finite radius, the formula is [2.16]

$$L = \frac{\mu}{2\pi} I \left[\ln\left(\frac{2l}{\rho}\right) - \frac{3}{4} \right] \quad (\text{Eq.2.27})$$

2.4.5 Resistance of cylindrical conductor geometry

For a hollow cylindrical conductor of length l_z , inner radius r_i and outer radius r_o ,

$$R = \eta(\rho_d, T) \frac{l_z}{S} = \eta(\rho_d, T) \frac{l_z}{\pi(r_o^2 - r_i^2)} \quad (\text{Eq.2.28})$$

When it is necessary to account for skin depth, it is more convenient to replace $r_o - r_i$ by δ , giving

$$R(r_o, \delta, l_{cyl}) = \eta(\rho_d, T) \frac{l_{cyl}}{\pi(r_o - r_i)(r_o + r_i)} = \eta(\rho_d, T) \frac{l_{cyl}}{\pi\delta(2r_o - \delta)} \quad (\text{Eq.2.29})$$

2.5 HVT inductance calculations

2.5.1 The textbook formula

Usually, calculation of the inductance of a winding is performed with the aid of ready-to-use expressions [2.16]. These include coefficients that are derived under the assumption that each layer of the winding can be replaced by a cylindrical shell in which the current is uniformly distributed. The coefficients are tabulated as a function of the winding geometry. But when the current rise time in the coil is very short, the assumption that the current is uniformly distributed may not be satisfied, and this method is then not sufficiently powerful. Especially when the inductor is very large, the predicted inductance may be inaccurate, as is the case in many high power transformers.

2.5.2 The Energy Method

Once the filamentary currents of, say, the high-voltage transformer are known, the magnetic energy stored in all the filamentary self and mutual inductances can be calculated at any time during a discharge of the capacitor bank. The total energy stored in a winding can be found directly by adding the magnetic energy associated with each of the filaments, and the result obtained must be equal to the energy stored in the corresponding element of the lumped component model (i.e. $\frac{LI^2}{2}$). The self-inductance of the single-turn primary winding is then given by

$$L_p = \frac{\sum_{i=1}^{N_p} \sum_{j=1}^{N_p} M_{ij} I_i I_j}{\left(\sum_{i=1}^{N_p} I_i \right)^2} \quad (\text{Eq.2.30})$$

and that of the multi-turn secondary winding (represented by N concentric cylinders) by

$$L_s = \frac{\sum_{i=Np+1}^{Nt} \sum_{j=Np+1}^{Nt} M_{ij} I_i I_j}{\left(\sum_{i=Np+1}^{Nt} I_i \right)^2} \quad (\text{Eq.2.31})$$

Similarly, the mutual inductance between the primary and secondary windings is

$$M = \frac{\sum_{i=1}^{Np} \sum_{j=Np+1}^{Nt} M_{ij} I_i I_j}{\sum_{i=1}^{Np} I_i \left(\sum_{i=Np+1}^{Nt} I_i \right)} \quad (\text{Eq.2.32})$$

Although the above '*energy method*' is necessary to account accurately for dynamic changes in the HVT inductance due to current redistribution during a fast transient process, it may demand lengthy calculations on a PC. If however a very fast answer is required, particularly during a multi-parameter investigation at the early stage of a transformer design, a simplification may be introduced by considering the filamentary currents in a winding as all equal i.e., a homogeneous current distribution. No differential equations now need to be solved, and the results can be obtained on a PC by a simple summation, usually taking only a small fraction of a second. Although this '*simplified energy method*' is obviously less precise, a number of comparisons have shown that the results provided are normally adequate for initial investigations.

2.5.3 The Magnetic Flux Method

Another technique that is potentially useful is to consider the magnetic field distribution in the coils. To calculate the inductance, the single-turn primary winding can be considered as a cylinder and the secondary winding regarded as a set of multi-turn concentric cylinders. The z axis field distribution $H_z(r, z)$ inside a cylinder of length l is [2.2].

$$\begin{aligned}
H_z(r, z) = & (I/l) \frac{1}{4\pi} \int_0^\pi \frac{1 - x \cos \psi}{1 + x^2 - 2x \cos \psi} \\
& \times \left\{ \frac{1 - z'}{[y^2(1 + x^2 - 2x \cos \psi) + (1 - z')^2/4]^{1/2}} \right. \\
& \left. + \frac{1 + z'}{[y^2(1 + x^2 - 2x \cos \psi) + (1 + z')^2/4]^{1/2}} \right\} \quad (\text{Eq.2.33})
\end{aligned}$$

where $y = a/l$, $x = r/a$, and $z' = z/(l/2)$.

The self-inductance of one cylinder can be calculated from

$$L_i = \frac{\mu_0}{I} \int_0^a H_z(r, 0) 2\pi r dr \quad (\text{Eq.2.34})$$

where a is the radius of the cylinder, I and $H_z(r, 0)$ are the current in the cylinder and the magnetic field that it produces.

The mutual inductance $M_{i,j}$ between two concentric cylinders is calculated from

$$M_{i,j} = \frac{\mu_0}{I_j} \int_0^{a_i} H_z'(r, 0) 2\pi r dr \quad (\text{Eq.2.35})$$

where a_i is the radius of the inner cylinder, I_j and $H_z'(r, 0)$ are the current in the outer cylinder and the magnetic field that it produces.

In general, the self-inductance of the primary winding is

$$L_p = \frac{\mu_0}{I_p} \int_0^a H_z(r, 0) 2\pi r dr \quad (\text{Eq.2.36})$$

The self-inductance of a multi-turn secondary winding represented by n concentric cylinders is

$$L_s = \sum_{i=1}^n L_i + \sum_{i,j=1}^n M_{i,j} \quad (\text{Eq.2.37})$$

where L_i is the inductance of the i_{th} of the secondary cylinders and $M_{i,j}$ is the mutual inductance between the i and j cylinders.

The mutual inductance between the primary and secondary windings is

$$M_{ps} = \sum_{i=1}^n M_{pi} \quad (\text{Eq.2.38})$$

where M_{pi} is the mutual inductance between the primary and the i_{th} of the n secondary cylinders.

2.6 Skin and proximity effects

In an electromagnetic field in which electrical pulses are involved, eddy current effects may have a major influence on the system behaviour and characteristics. These effects are normally termed skin effect and proximity effect. Skin effect is a tendency for an alternating current to flow mostly near the outer surface of a solid electrical conductor. This effectively limits the cross-sectional area available to carry the current, increasing the resistance of that conductor above what it would normally be for direct current. Proximity effect is the tendency for current to flow in other undesirable patterns, such as loops or concentrated distributions, due to the presence of magnetic fields generated by nearby conductors. The relative magnitudes of skin effect and proximity effect losses in a coil will depend on the number of turns, on the spacing between the turns and on the shape of the winding. In transformers and inductors, proximity effect losses normally dominate skin effect losses.

Usually, skin and proximity effects in the coil are included as loss mechanisms, based on familiar handbook formulae [2.17], developed for round wire single-layer coils carrying a steady sinusoidal current, but these gross over-simplifications can

introduce extremely large errors. It has been demonstrated however that the filamentary model can very accurately calculate both skin [2.6] and proximity [2.7] effect, and a practical example of the filamentary method applied to the two-dimensional current diffusion analysis of a single turn coil is discussed later.

2.7 Magnetic field, forces and other issuers

Evaluation of the distribution and strength of the magnetic fields in various pulsed power systems consisting of massive conductors is very important. For example, magnetic coupling with nearby metallic elements may have a significant affect on the overall behaviour of the system, (and can readily be introduced if these are non-ferrous), or the response of inductive magnetic pick-up probes may need to be predicted. The strength and the complete magnetic field map can be obtained easily from filamentary model by adding the individual flux densities produced by all the different filaments, and the radial and axial components of each filament are defined by Equations 2.10 and 2.11.

When large currents are present, the forces between the windings of a transformer may be sufficient to cause them to become distorted, so that it is important to evaluate the size of the forces between windings. The forces can be calculated by summing the individual filamentary contributions, with the axial and radial forces between the i_{th} filament of one winding and the j_{th} filament of the other using the formula Equations 2.14 and 2.15.

If required, the time variation of the resistances of both windings during a transient loading can also be calculated by considering the Joule energy deposited in each filament [2.7]. In the same way the temperature distribution inside the conductors can be predicted. In addition, the inevitable coil movement can be estimated by adding the appropriate mechanical equations of motion.

2.8 Capacitance calculation

Once the cross section of conductor is decomposed into a set of n infinitely thin circles positioned at heights z_i with radii r_i , and if each ring has a uniform charge distribution with a total charge q_i , the potential ψ due to ring i at any given position r_0, z_0 is given by:

$$\Psi_i(r_0, z_0) = \frac{q_i}{4\pi^2 \epsilon_0 \sqrt{r_0 r_i}} Q_{-1/2}\left(\frac{2}{k^2} - 1\right) = \frac{q_i}{2\pi^2 \epsilon_0 R_i} K \quad (\text{Eq.2.39})$$

$$\text{where } k = \frac{2\sqrt{r_0 r_i}}{R_i}, R_i = \sqrt{(|r_i| + |r_0|)^2 + (z_0 - z_i)^2}$$

Considering then the mutual influences between all the rings, a matrix P can be computed that allows calculation of the potentials v_i at each ring once the charge q_i is known [2.10]:

$$\begin{aligned} v &= Pq \\ P_{i,j} &= P_{j,i} = \frac{\Psi_i(r_j, z_j)}{q_i} \\ P_{i,i} &= \frac{\Psi_i(r_i, z_i + R)}{q_i} \end{aligned} \quad (\text{Eq.2.40})$$

For the calculation of the “self-potentials” P_{ii} , the radius of the rings R is defined as

$$R = \frac{a}{\pi} \sin \frac{\Delta\theta}{2} \quad (\text{Eq.2.41})$$

This radius makes the area of the surface of the ring identical to the flat area represented by it.

Assuming that the conductor has uniform potential V , the charge distribution at all the rings can be calculated by inverting the matrix P . Using the influence coefficients $k_{i,j}$ to represent the coefficients of C [2.10], Equation 2.40 can be written as

$$q_i = V \sum_{j=1}^n k_{i,j}$$

$$C = P^{-1} \quad (\text{Eq.2.42})$$

and the capacitance of the whole assembly is simply the sum of all the elements of C :

$$C_{total} = \sum_{i=1}^n \sum_{j=1}^n k_{i,j} \quad (\text{Eq.2.43})$$

The capacitance matrix around an electrical system including a series of objects with axial symmetry can also be easily calculated if the objects are decomposed into series of rings. To obtain the capacitance matrix is merely a matter of adding the terms of the total capacitance matrix that corresponds to the rings that belong to each object, instead of adding them all to obtain the capacitance of the entire system. The charges on all the rings can be obtained from the complete equation $q = CV$, with the assigned voltages of the objects arranged in correspondence with the rings that belong to the objects. The potential anywhere around the objects (with assigned voltages) is obtained by adding Equation 2.39 for all the rings.

For the whole electrical system, the terms in the diagonal of the capacitance matrix correspond to the capacitances of an object to ground, when all the other objects are grounded. The off-diagonal influence coefficients express the relation between the charge induced in one object and the voltage in another, when all the other objects are grounded. From the capacitance matrix, a model of the circuit using lumped capacitors can be derived, by observing the equivalence [2.10]:

$$\begin{aligned}
 C &= \begin{bmatrix} k_{11} & k_{12} & \cdots & k_{1n} \\ k_{12} & k_{22} & \cdots & k_{2n} \\ \vdots & \vdots & \ddots & \vdots \\ k_{1n} & k_{2n} & \cdots & k_{nn} \end{bmatrix} \\
 &= \begin{bmatrix} C_{11} + C_{12} + \cdots + C_{1n} & -C_{12} & \cdots & C_{1n} \\ -C_{12} & C_{22} + C_{12} + \cdots + C_{2n} & \cdots & C_{2n} \\ \vdots & \vdots & \ddots & \vdots \\ -C_{1n} & -C_{2n} & \cdots & C_{nn} + C_{nn-1} + C_{1n} \end{bmatrix} \quad (\text{Eq.2.44})
 \end{aligned}$$

C_1, C_2, \dots, C_n are direct capacitances between the elements and the ground, and the other elements are the negative of the floating capacitances between the objects. The direct capacitance to ground for the object i is simply the sum of the elements in the line, or column, i of C .

2.9 Electric field and potential distribution

The electric field at any point can be calculated by adding the electric fields due to the rings. From Equation 2.39, the radial and axial components of the electric field can be calculated by differentiation, resulting in:

$$\begin{aligned}
 E_{\text{radial}} &= -\frac{d\Psi_i}{dr_0} \\
 &= -\frac{q_i \sin r_i}{2\pi^2 \epsilon_0 R_i^3} \left\{ -(r_i - |r_0|)K + \frac{E - k^2 K}{kk'^2} \left[\frac{2|r_0|}{k} - k(r_i - |r_0|) \right] \right\} \quad (\text{Eq.2.45})
 \end{aligned}$$

$$E_{\text{axial}} = -\frac{d\Psi_i}{dz_0} = \frac{q_i(z_i - z_0)E}{2\pi^2 \epsilon_0 R_i^3 k'^2} \quad (\text{Eq.2.46})$$

$$E_{\text{total}} = \sqrt{E_{\text{radial}}^2 + E_{\text{axial}}^2} \quad (\text{Eq.2.47})$$

where the derivative of the elliptic integral K with respect to the modulus k is used:

$$\frac{dK}{dk} = \frac{E - k'^2 K}{kk'^2}; \quad \frac{dE}{dk} = \frac{E - K}{k}; \quad k'^2 = 1 - k^2 \quad (\text{Eq.2.48})$$

The potential anywhere around the objects is obtained by adding Equation 2.39 for all the rings, and the electric field by adding Equations 2.45 and 2.46 using Equation 2.47.

2.10 2D modelling of HVT

2.10.1 HVT basic geometries

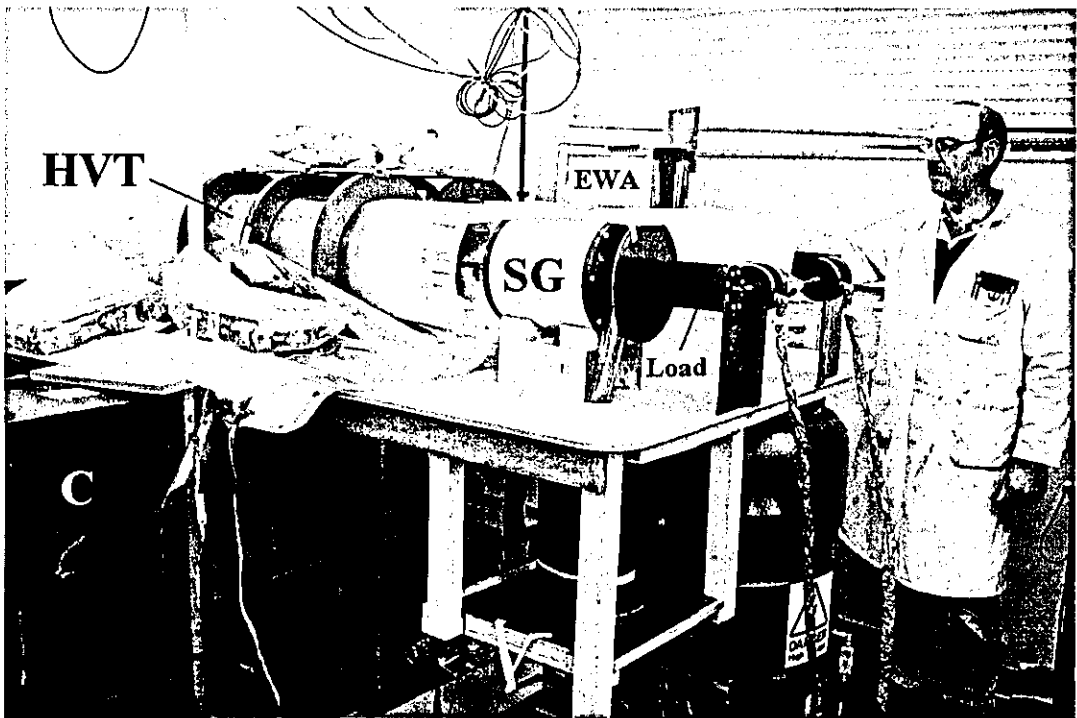


Figure 2.4 Loughborough based pulsed power system including a spiral-strip HVT

[2.18]

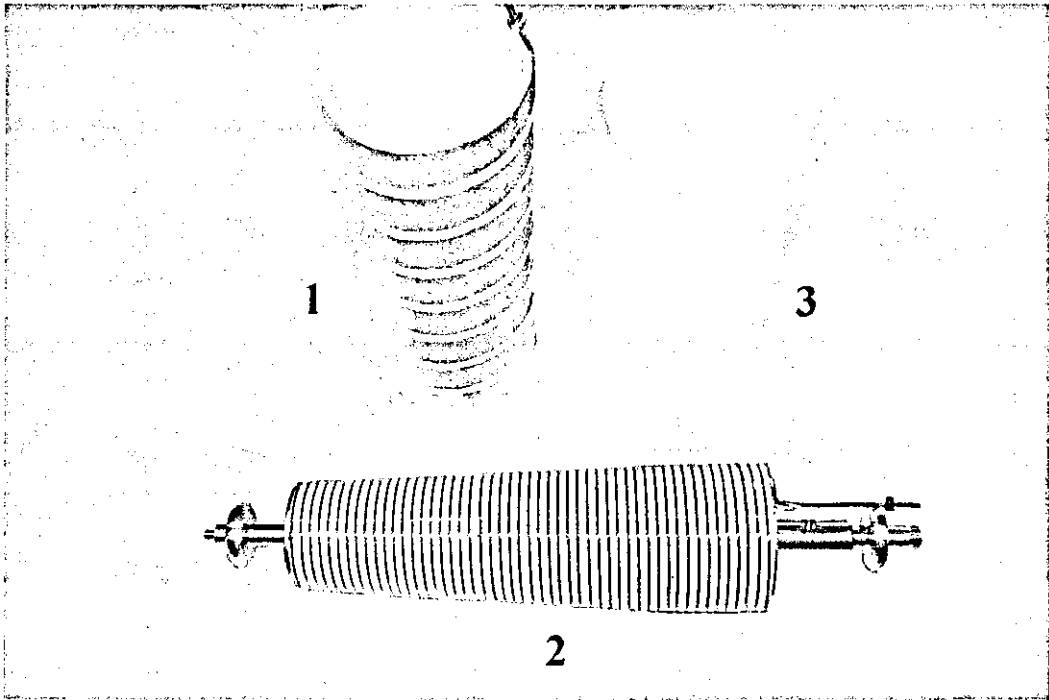


Figure 2.5 Helical HVT developed at Texas Tech University (TTU), USA [2.19]

1- primary, 2- secondary, 3- outer insulator (Photo courtesy of Dr. Michael Giesselmann. The TTU work was funded by the Explosive-Driven Power Generation MURI program funded by the Director of Defense Research & Engineering and managed by the Air Force Office of Scientific Research).

When used in high power systems, HVTs are normally constructed in either the spiral-strip configuration of Figure 2.4, in which both the primary and secondary windings are usually wound from copper sheet, or the helical arrangement of Figure 2.5, in which at least the secondary winding is in the form of a relatively thin conductor. The merits and drawbacks of both configurations are summarized in Table 2.1.

2.10.2 2D modelling of a spiral-strip HVT

Figure 2.6 shows a simplified view of a typical spiral-strip HVT, with a single-turn thick primary winding connected to a flat transmission line (TL) and the secondary winding represented by an assembly of N thin, concentric slotted cylinders connected in series. The two windings have a common ground connection. The radius of the cylinder is given by

$$r_s^k = r^m + (N - k + \frac{1}{2}) \times p \quad (\text{Eq.2.49})$$

Table 2.1 Relative merits and drawbacks of HVT designs for use in high-power systems

HVT type	Advantages	Disadvantages
Spiral-strip	<ul style="list-style-type: none"> -large coupling coefficient possible (>0.9) -can carry large currents ($>1 \text{ MA}$) in both winding circuits -coaxial output, as required by most loads -can be scaled for multi-MV operation 	<ul style="list-style-type: none"> -primary winding cannot accept a parallel transmission line feed and a 'fish-tail' adaptor is needed to couple to a coaxial configuration -relatively complex to manufacture -high secondary capacitance
Helical	<ul style="list-style-type: none"> -relatively easy to manufacture -can be easily adapted to a coaxial geometry -low secondary winding capacitance -can have extremely high secondary/primary turns ratio 	<ul style="list-style-type: none"> -low coupling coefficient (<0.8) -difficult to scale to above 1 MV -cannot drive large currents in the secondary winding

where $k=1,2,\dots,N$, and r^m is the radius of the plastic mandrel (not shown) that supports the secondary winding. The pitch p of the secondary winding is determined by the combined thickness of the winding conductor and the inter-layer insulation provided

by thin Mylar foils, and takes into account air that is always present between the layers and represents some 20% to 30% of the total insulator thickness.

In many applications, the low frequency of the transformer currents enables the magnetic field to diffuse easily through the thin secondary winding conductor, and the effective skin depth is greater than one half of the conductor thickness. It is then possible to represent the winding by a single layer of filaments, and on this basis Figure 2.7 shows a filamentary representation for a spiral-strip HVT. Due to axial symmetry it is only necessary to calculate the currents in one half of the transformer, say the upper part, which considerably reduces the time needed for the numerical analysis. The model requires a total of $Nt = Np + Ns$ filaments, with the number in the primary winding given by $Np = np \times mp$, the product of the number of rows np and columns mp , and the number in the N secondary windings by the corresponding

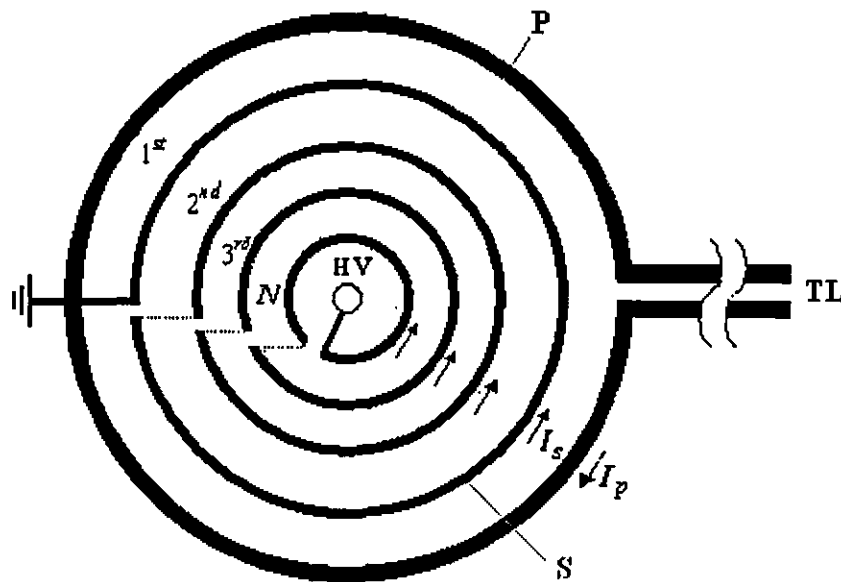


Figure 2.6 Simplified view of spiral-strip HVT circuit for use in filamentary modelling

P-primary, S-secondary, TL-flat transmission line(input), HV-high voltage output

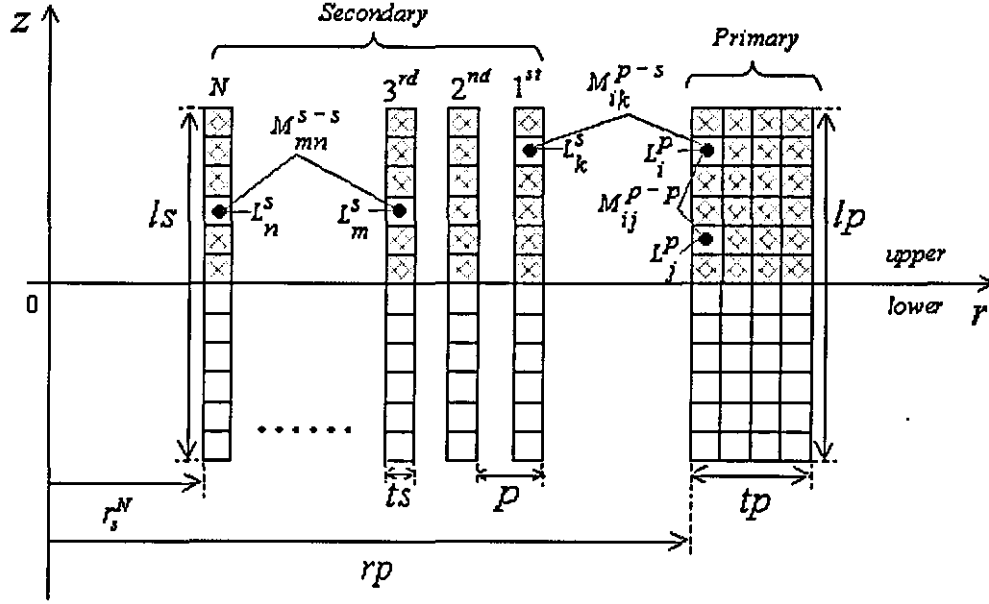


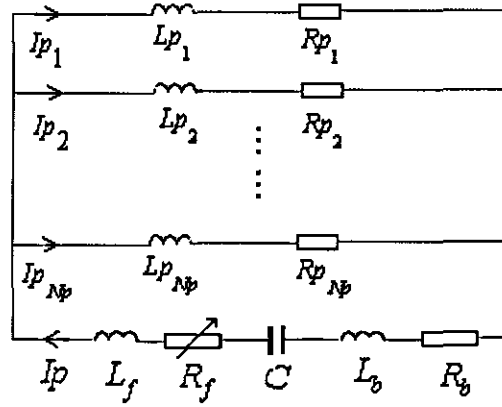
Figure 2.7 Filamentary representation of the spiral-strip HVT

product $Ns = ns \times ms \times N$. It follows from Figure 2.7 that the equivalent circuits for the primary and secondary windings are as in Figure 2.8, when the corresponding set of first-order differential equations that has to be solved is

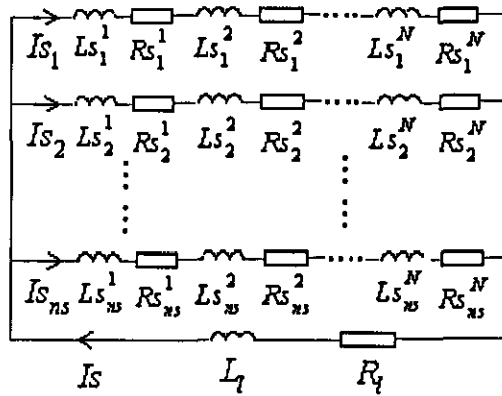
$$V_0 - \frac{Q}{C} = L_b \frac{dI_p}{dt} + R_b I_p + L_f \frac{dI_p}{dt} + R_p I_i + \sum_{j=1}^{Np} M_{ij}^{p-p} \frac{dI_j}{dt} - \sum_{j=Np+1}^{Nt} M_{ij}^{p-s} \frac{dI_j}{dt} \quad (i=1, \dots, Np) \quad (\text{Eq.2.50})$$

$$L_l \frac{dI_s}{dt} + R_l I_s + \sum_{k=1}^N R_s^k I_i + \sum_{j=Np+1}^{Nt} M_{ij}^{s-s} \frac{dI_j}{dt} - \sum_{j=1}^{Np} M_{ij}^{s-p} \frac{dI_j}{dt} = 0 \quad (i=Np+1, \dots, Np+ns) \quad (\text{Eq.2.51})$$

$$\frac{dQ}{dt} = I_p \quad (\text{Eq.2.52})$$



(a)



(b)

Figure 2.8 Equivalent filamentary circuit diagram for a spiral strip HVT

(a) primary circuit (b) secondary circuit. For clarity mutual inductances are omitted.

In the equations above C , V_0 and Q are respectively the capacitance and initial voltage of the capacitor bank and the charge delivered to the circuit. Resistances R_b , R_i and inductances L_b , L_i arise from the capacitor bank (including the transmission line and closing switch) and the load. The primary and secondary

currents I_p and I_s are given by the sum of the filamentary currents I_i as $I_p = 2 \sum_{i=1}^{Np} I_i$ and $I_s = 2 \sum_{i=Np+1}^{Nt} I_i$, while the filamentary resistances in the primary and in the secondary k_{th} winding are $R_{p_i} = \frac{2\pi r_i}{\sigma_i \cdot ap}$ and $R_{s_i}^k = \frac{2\pi r_k}{\sigma_i \cdot as}$ where σ_i is the electrical conductivity at the temperature of the i_{th} filament. As shown in Figure 2.7, r_i is the radius of the i_{th} filament of cross sectional area $ap = \frac{hp \cdot tp}{2np \cdot mp}$ in the primary winding and $as = \frac{hs \cdot ts}{2ns \cdot ms}$ in the secondary. The self inductance of the i_{th} filament is given by Equation 2.21, while the mutual inductance between the i_{th} and j_{th} filaments with an axial displacement d_{ij} is from Equation 2.17. The superscripts identify the inductively connected elements e.g. M_{p-s} is for a mutual inductance between a pair of filaments situated respectively in the primary and secondary winding, and for convenience $M_{ij} = L_i$ is the self inductance of the i_{th} filament. Since in Equations 2.50 and 2.51 only half of the currents are considered, when terms containing filamentary mutual inductance are evaluated the sum must include filaments situated in both the upper and the lower part of the transformer, thus

$$M_{ij} = (M_{ij})_{upper-upper} + (M_{ij})_{upper-lower} \quad (\text{Eq.2.53})$$

2.10.3 2D modelling of a helical HVT

A typical helical HVT comprises a multi-turn primary winding made from copper sheet and a secondary winding of thin copper wire. As a consequence of the loss of symmetry resulting from the tapered secondary winding diameter adopted in most designs to reduce the electric field stress, all the filamentary winding currents have now to be calculated. A filamentary representation of the helical HVT is given in Figure 2.9, the equivalent circuits for the primary and secondary windings are shown in Figure 2.10 and the corresponding set of first-order differential equations is

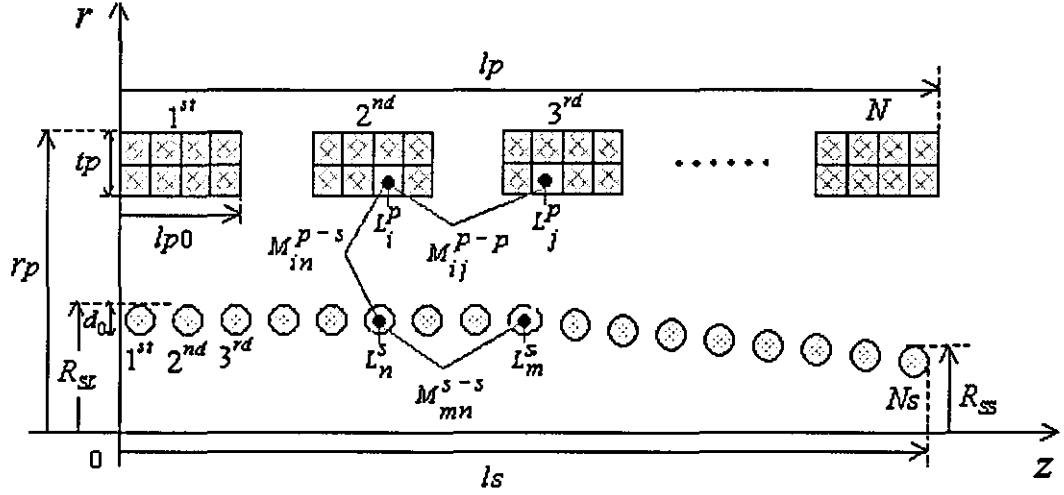


Figure 2.9 Filamentary representation of the helical HVT

R_{SL} and R_{SS} are the greatest and smallest radii of the secondary winding plastic mandrel (not shown).

$$V_0 - \frac{Q}{C} = L_b \frac{dl_p}{dt} + R_b I_p + L_f \frac{dl_p}{dt} + \sum_{k=1}^N R_{p_i}^k I_i + \sum_{j=1}^{N_p \times N} M_{ij}^{p-p} \frac{dl_j}{dt} - \sum_{j=N_p \times N+1}^{Nt} M_{ij}^{p-s} \frac{dl_j}{dt} \quad (i=1, \dots, N_p) \quad (\text{Eq.2.54})$$

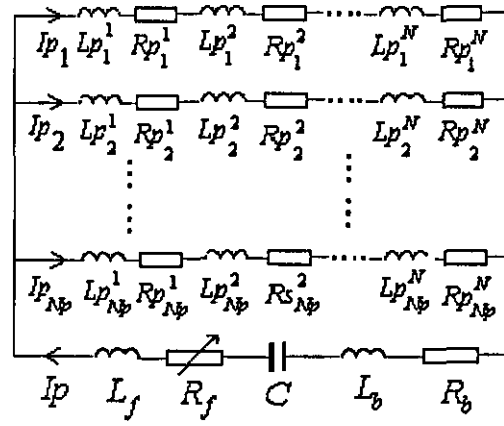
$$L_l \frac{dls}{dt} + R_l I_s + \sum_{k=N_p \times N+1}^{Nt} R_{s_k} I_i + \sum_{j=N_p \times N+1}^{Nt} M_{ij}^{s-s} \frac{dl_j}{dt} - \sum_{j=1}^{N_p \times N} M_{ij}^{s-p} \frac{dl_j}{dt} = 0 \quad (i=N_p+1) \quad (\text{Eq.2.55})$$

$$\frac{dQ}{dt} = I_p \quad (\text{Eq.2.56})$$

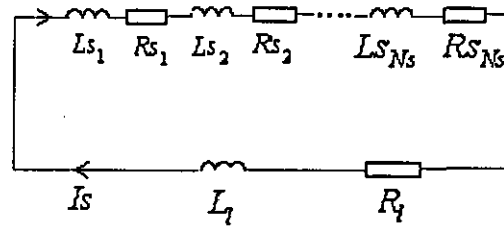
where the terms are as defined in Equations 2.50-2.52, except for (with reference to Figure 2.9):

$$Nt = N_p \times N + N_s, \quad I_p = \sum_{i=1}^{N_p} I_i, \quad I_s = I_{N_p+1}, \quad R_{p_i}^k = \frac{2\pi r_k}{\sigma_i \cdot ap}$$

$$R_{s_i} = \frac{2\pi r_i}{\sigma_i \cdot as}, \quad ap = \frac{lp_0 \cdot tp}{np \cdot mp} \quad \text{and} \quad as = \frac{\pi (d_0)^2}{4}.$$



(a)



(b)

Figure 2.10 Equivalent filamentary circuit diagram for a helical HVT

(a) primary circuit (b) secondary circuit. For clarity mutual inductances are not shown.

2.11 Benchmarking with experimental results

2.11.1 Inductance calculations

The inductances of a range of transformers have been calculated by all the methods mentioned here, and the results obtained for a typical spiral-strip HVT developed for the Loughborough pulsed power system shown in Figure 2.4 are presented in Table 2.2, where they are also compared with experimental measurements. The single-turn primary winding of this transformer is made from a copper sheet for which $r_p = 139.485 \text{ mm}$, $l_p = 600 \text{ mm}$ and $t_p = 0.25 \text{ mm}$. The $N=15$ turn secondary winding is wound on a cylindrical plastic mandrel from a $l_s = 600 \text{ mm}$ strip of copper sheet, for which $t_s = 0.1 \text{ mm}$, $p = 0.812$ and $r^m = 125 \text{ mm}$. Calculations based on the 2D model show that, in this case, the time variation of the HVT inductances predicted by the energy method for the particular transient loading that it experiences are negligible. The number of filaments chosen for evaluating the inductances by both energy methods was 100 for which, as presented in Figure 2.11, a change of the filament number by ± 20 gives a change in the calculated inductance of less than 1%.

A similar comparison was made for the helical HVT shown in Figure 2.5 that was developed at Texas Tech University, with the results obtained being presented in Table 2.3. It is important to note that, due to the thin conductors usually used in the secondary windings, the magnetic flux technique is not applicable to helical HVTs.

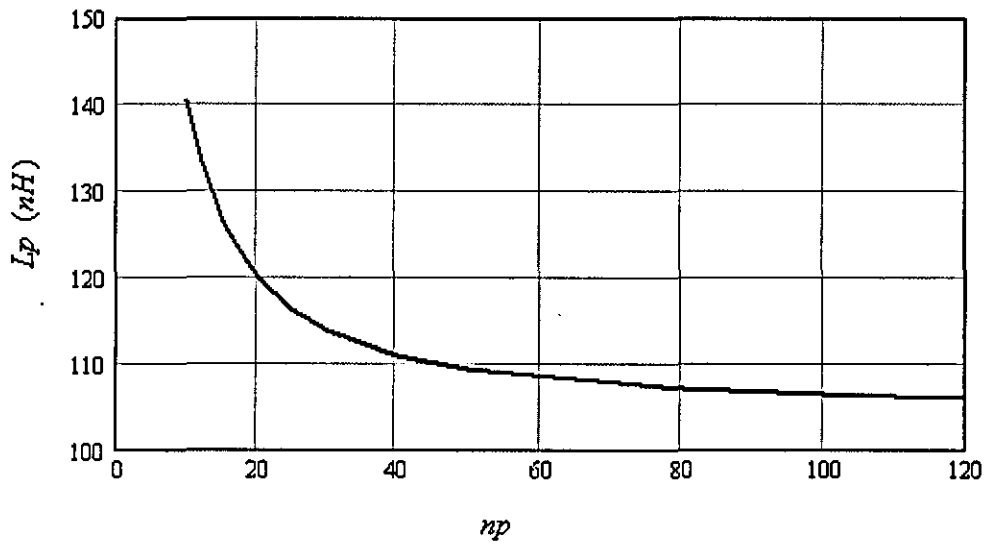


Figure 2.11 Variation of primary inductance L_p with the number of filaments in the axial direction n_p

(the technique used in finding the optimum number of filaments for the Loughborough 15 turn spiral-strip HVT is to choose $n_p=100$ for which a variation by ± 20 units gives a difference in L_p of less than 0.7 %.)

Table 2.2 Calculated and measured inductances for the Loughborough spiral-strip HVT

	Energy method	Simplified energy method	Magnetic flux technique	Textbook formulae [2.16]	Measured result
L_p (nH)	106.278	107.438	117.369	106.324	103 \pm 3%
M (μ H)	1.393	1.399	1.554	1.398	1.32 \pm 3%
L_s (μ H)	20.437	20.611	25.698	20.557	20 \pm 3%

Table 2.3 Calculated and measured inductances for the Texas Tech University helical HVT [2.19]

	Energy method	Simplified energy method	Textbook formulae[2.16]	Measured result [2.19]
$L_p (\mu H)$	3.470	3.479	3.406	3.46
$M (\mu H)$	88.922	88.922	90.52	86
$L_s (\mu H)$	13.2343	13.210	13.99	13.02

2.11.2 Dynamic HVT performance in a conditioning system

To benchmark the 2D filamentary modelling predictions, the simulated load voltage corresponding to the conditioning circuit in Figure 2.12 was compared with published results [2.20] in Figure 2.13. For modelling the opening switch, in this case an aluminium foil, the data given in [2.21] was used. A similar comparison is shown in Figure 2.14 for the Loughborough pulsed power system presented in Figure 2.4, with the complete system data presented elsewhere [2.18].

The agreement evident in both Figures 2.13 and 2.14 confirms that the present 2D filamentary model can successfully be used to predict accurately the dynamic performances of HVTs in high power conditioning systems.

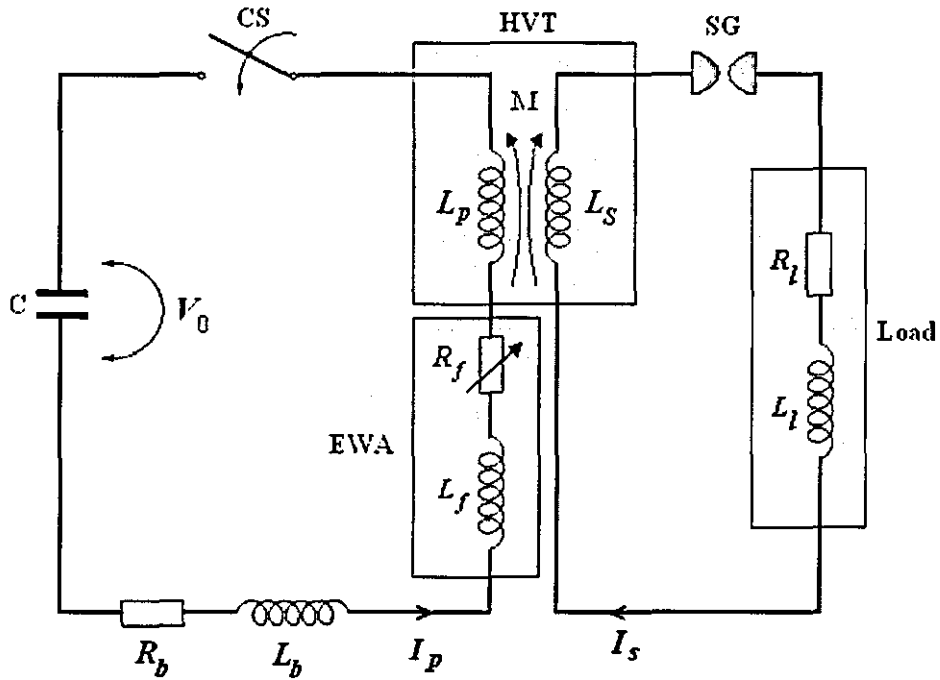


Figure 2.12 Equivalent lumped circuit of a laboratory based pulsed power system

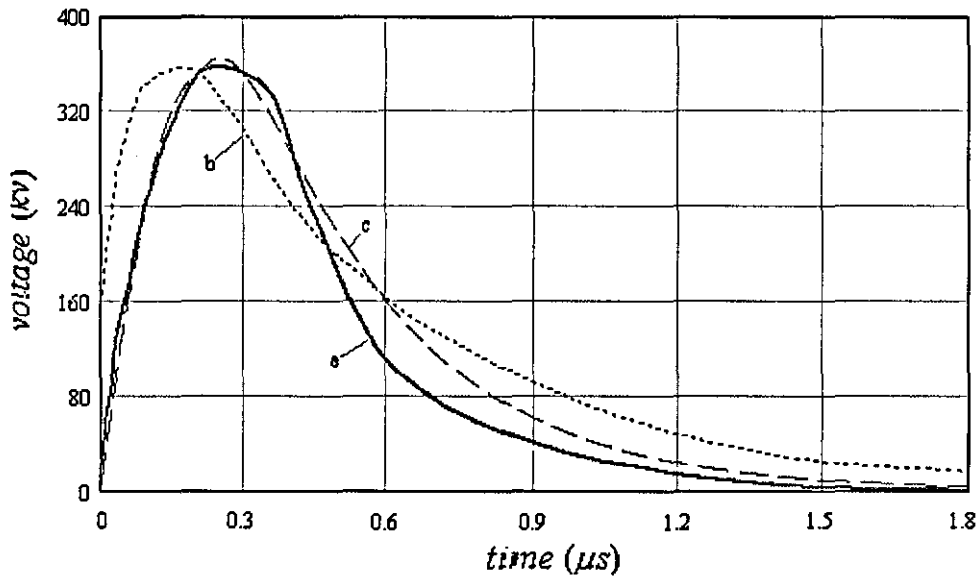


Figure 2.13 Load voltage for the laboratory based system presented in [2.20]

- (a) experimental load voltage from [2.20] (b) theoretical prediction from [2.20] (c) theoretically predicted using the present 2D filamentary model

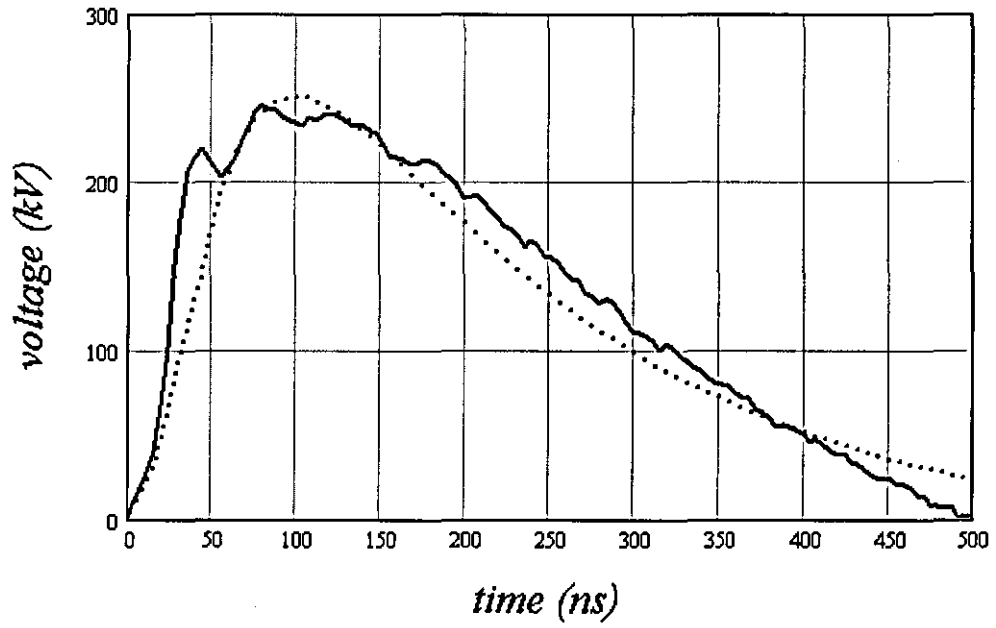


Figure 2.14 Load voltage for the Loughborough system presented in Figure 2.3
full line-measured load voltage, dotted line-theoretical prediction using the 2D
filamentary model [2.18]

3 Finite element analysis

3.1 Introduction to FEA

Finite Element Analysis (FEA) is a computer-based numerical technique developed originally for calculating the strength and behaviour of engineering structures. Such structures may have complex geometry and loading, and consequently may either be very difficult to analyze or even to have no analytical solution. However, by using FEA, a structure of this type can be readily analysed numerically. It is not only useful for analysing classical static structural problems, but also in such diverse areas as mass transport, heat transfer, dynamics, stability, and radiation problems.

The term “finite element” distinguishes the technique from that of the infinitesimal “differential elements” used in calculus, differential equations, and partial differential equations. The method is also distinguished from finite difference equations, in which, although the shapes into which space is divided are finite in size, there is little freedom in the selection of these shapes. FEA provides a way of dealing with more complex structures than is possible with partial differential equations and it deals with complex boundaries better than finite difference equations. FEA also makes it possible to evaluate a detailed and complex structure on a computer, and it can be used in many disciplines for optimizing new designs, verifying the fitness of existing facilities, performance predictions and evaluating new concepts. A computer demonstration of the adequate strength of the structure and the possibility of improving the design during planning can easily justify the cost of the work involved.

In the Finite Element Method, a structure is broken down into many small simple blocks or elements. These are connected at discrete joints called nodes, which together form a grid termed a mesh. This is programmed to contain the material and structural properties that define how the structure will react to certain loading conditions. For each element in the model, equations can be written relating the

displacements and forces at each node. As all the elements are joined together to form the structure, the equations describing the behaviour of the individual elements are combined into an extremely large set of equations that describe the behaviour of the whole structure. From a computer solution of these equations, the behaviour of the individual elements can be extracted and the deflection of all the parts of the structure can be determined.

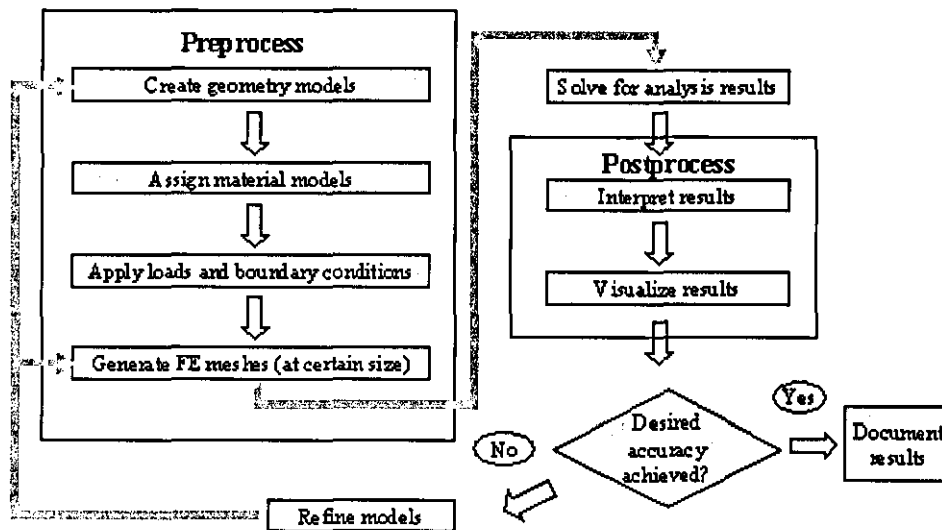


Figure 3.1 Typical FEA process

A typical FEA process includes the steps shown in Figure 3.1. The first decision is to use either a 2-D or a 3-D program to model the engineering structure, which is then divided graphically into small elements so that the mechanical behaviour of each and every element can be defined by a set of differential equations. The differential equations are converted into algebraic equations and then into matrix equations suitable for a computer-aided solution. The element equations are combined and a global structural equation is obtained. After appropriate load and boundary conditions are introduced, the resulting deflection is calculated at the nodes. A node can be shared by several elements, and the deflection at the shared node represents the deflection of the sharing elements at the node location. The deflection at any other

point in the element is calculated by an interpolation of all the node points in the element. Both linear higher order interpolation function and the individual element matrix equations are assembled into a combined structure. Although the evidence at the postprocessing stage may give the impression that the solution is accurate, it may not in fact predict the correct behaviour. FEA will always give some sort of solution, even for a poorly developed model; however, the resulting solution may be highly incorrect for the analysis of the physical phenomenon. The usefulness of the FEA result depends significantly on the preprocessing stage.

Commercial FEA programs are written so that the user can solve complex engineering problems without knowing the governing equations or the mathematics; the user is required only to know the geometry of the structure and its boundary conditions. For the studies in this thesis the commercially available program ANSYS (www.ansys.com) was used. ANSYS is a widely available general-purpose finite element analysis program for engineering analysis, that can solve a wide range of structural, mechanical, electromagnetic, thermal, fluid and biomedical problems and can provide the appropriate values of displacements, forces, stresses, strains, temperatures and magnetic fields. Analysis types available range from a simple, linear, static analysis to a complex, nonlinear, transient dynamic analysis.

3.2 Field computations

Finite Element Methods permit the calculation of electric potentials and fields in complicated geometries. The ANSYS program provide a set of drawing tools which allow the user to input the geometry in as much detail as desired. More sophisticated programming even allows a parametric input, so that changes in one or more geometric parameters, such as the distance between electrodes in an electro-dynamic problem, can be easily accomplished without redoing the entire geometry. Both 2D and 3D versions are available, although the input to the 3D version is, of course, far more complicated. For many problems, a 2D geometry can provide an adequate approximation to the real configuration, and it usually allows consideration of an

axisymmetric geometry by inputting the relevant cross section. In this sense, it is really solving a 3D problem which happens to have cylindrical symmetry. The (x,y) 2D geometry is, in reality, modelling an infinitely long object having the specified 2D cross-section.

The basic geometry that the user inputs is subdivided into a triangular mesh, with smaller triangles used in regions where the potential is expected to change most rapidly. Larger triangles can adequately describe more slowly varying potential regions. ANSYS is able to perform automatically the triangular meshing and, through an iterative process, even to refine the mesh in critical regions until the desired solution accuracy is achieved. When linear triangles are used, the potential is solved only at the triangle nodes and a linear interpolation scheme is used to approximate inside the triangle. For higher-order triangles additional nodes are added per triangle, and higher order polynomial approximations are used to find the potential inside the triangles.

The geometric input to the solution represents an important step. Very often, full details are unnecessary for a determination of the fields in critical regions. Thus the user must know when it is reasonable to ignore certain geometric details that are irrelevant to the problem. This not only saves the labour involved in inputting the geometry but it can also considerably reduce both the computer memory and solution times required

Finite element programs require that the user input sources and the appropriate boundary conditions for the problem are at hand. In the case of electric potential calculations, the sources are electric charges and the boundary conditions include specifying the voltage at one or more electrode surfaces. These are often the surfaces of metallic objects and they thus have a constant potential throughout. It is therefore unnecessary to model their interiors. Typically, the program will allow the user to declare such metallic objects to be nonexistent, so that the solution is not considered in their interiors. Their surface is however still included as an equipotential surface. Sometimes this is a boundary surface, so that it already has no interior. A metallic object can also be allowed to float, so that its potential becomes part of the problem solution.

On external boundaries, where no specification is made, the assumption is that these have natural or Neumann boundary conditions. This means that the normal derivative of the potential vanishes along them and implies that the potential lines (in 2D) or surfaces (in 3D) enter the boundary at right angles. This type of boundary is usually used to express some symmetry condition. For instance, a long conducting cylinder can be modelled by means of a circle. However, by symmetry, only a quarter of the geometry needs be modelled, and natural boundary conditions are imposed on the new boundaries created by isolating this region. Another boundary condition, the balloon boundary, is also allowed. This type of boundary is equivalent to saying that a boundary does not exist and that the solution continues beyond it, as if there was empty space out to infinity.

3.3 General formulation

When the Finite Element Method is used for field computation, it results in a set of linear equations that are solved by direct matrix or iterative methods. The electric stress in any element is calculated by differentiating the approximated polynomial function.

When the time-derivative of the magnetic flux density $\left\{\frac{\partial B}{\partial t}\right\}$ (the quasistatic approximation) is neglected, the electric field is governed by the following Maxwell's equations [3.1]:

$$\nabla \times \{H\} = \{J\} + \left\{\frac{\partial D}{\partial t}\right\} \quad (\text{Eq.3.1})$$

$$\nabla \times \{E\} = \{0\} \quad (\text{Eq.3.2})$$

$$\nabla \cdot \{B\} = 0 \quad (\text{Eq.3.3})$$

$$\nabla \cdot \{D\} = \rho \quad (\text{Eq.3.4})$$

It follows from Equation 3.2 that the electric field $\{E\}$ can be derived from:

$$\{E\} = -\nabla V \quad (\text{Eq.3.5})$$

where V = electric scalar potential

Without velocity effects, the constitutive relations for the electric field are:

$$\{J\} = [\sigma]\{E\} \quad (\text{Eq.3.6})$$

$$\{D\} = [\varepsilon]\{E\} \quad (\text{Eq.3.7})$$

where

$$[\sigma] = \begin{bmatrix} \frac{1}{\rho_{xx}} & 0 & 0 \\ 0 & \frac{1}{\rho_{yy}} & 0 \\ 0 & 0 & \frac{1}{\rho_{zz}} \end{bmatrix} = \text{electrical conductivity matrix}$$

ρ_{xx} = resistivity in the x-direction

$$[\varepsilon] = \begin{bmatrix} \varepsilon_{xx} & 0 & 0 \\ 0 & \varepsilon_{yy} & 0 \\ 0 & 0 & \varepsilon_{zz} \end{bmatrix} = \text{permittivity matrix}$$

ε_{xx} = permittivity in the x-direction

The conditions for $\{E\}$, $\{J\}$, and $\{D\}$ at a material interface are:

$$E_{n1} - E_{n2} = 0 \quad (\text{Eq.3.8})$$

$$J_{tn} + \frac{\partial D_{tn}}{\partial t} = J_{tn} + \frac{\partial D_{tn}}{\partial t} \quad (\text{Eq.3.9})$$

$$D_{tn} - D_{tn} = \rho_s \quad (\text{Eq.3.10})$$

where

E_{t1}, E_{t2} = tangential components of $\{E\}$ on both sides of the interface

J_{n1}, J_{n2} = normal components of $\{J\}$ on both sides of the interface

D_{n1}, D_{n2} = normal components of $\{D\}$ on both sides of the interface

ρ_s = surface charge density

In quasistatic electric analysis, the relevant governing equations are Equation 3.5 and the continuity equation:

$$\nabla \cdot \left(\{J\} + \left\{ \frac{\partial \{D\}}{\partial t} \right\} \right) = 0 \quad (\text{Eq.3.11})$$

Substituting the constitutive Equations 3.6 and 3.7 into Equation 3.11, and taking into account Equation 3.5, leads to the differential equation for electric scalar potential:

$$-\nabla \cdot ([\sigma] \nabla V) - \nabla \cdot \left([\epsilon] \nabla \frac{\partial V}{\partial t} \right) = 0 \quad (\text{Eq.3.12})$$

Equation 3.12 takes into account both conductive and dielectric effects in electric materials and it can be used to approximate a time-varying electric field. Neglecting any time-variation in the electric potential, Equation 3.12 reduces to the governing equation for steady-state electric conduction:

$$-\nabla \cdot ([\sigma] \nabla V) = 0 \quad (\text{Eq.3.13})$$

In the case of a time-harmonic electric field analysis, Equation 3.12 can be rewritten as:

$$-\nabla \cdot ([\epsilon] \nabla V) + \frac{j}{\omega} \nabla \cdot ([\sigma] \nabla V) = 0 \quad (\text{Eq.3.14})$$

where:

$$j = \sqrt{-1}$$

ω = angular frequency

In electrostatic analysis, the electric scalar potential equation for electrostatic analysis is derived from the governing Equations 3.4 and 3.5, and the constitutive Equation 3.7 as:

$$-\nabla \cdot ([\varepsilon] \nabla V) = \rho \quad (\text{Eq.3.15})$$

The finite element matrix equations can be derived by variational techniques, which exist for linear and nonlinear material behaviour as well as for the static and transient response. Based on the presence of linear or non-linear materials, the appropriate Newton Raphson Method is chosen for the derivation of the electromagnetic matrices; when transient affects are to be considered a first-order time integration scheme must be involved.

The electric scalar potential V is approximated over the element by:

$$V = \{N\}^T \{V_e\} \quad (\text{Eq.3.16})$$

where:

$\{N\}$ = element shape function

$\{V_e\}$ = nodal electric scalar potential

The application of the variational principle and finite element discretization to the differential Equation 3.12 produces a matrix equation in the form:

$$[C]\{V_e\} + [K]\{V_e\} = \{I_e\} \quad (\text{Eq.3.17})$$

where:

$$[K] = \int_{vol} (\nabla \{N\}^T)^T [\sigma] (\nabla \{N\}^T) d(vol) = \text{electrical conductivity coefficient}$$

matrix

$$[C] = \int_{vol} (\nabla \{N\}^T)^T [\varepsilon] (\nabla \{N\}^T) d(vol) = \text{dielectric permittivity coefficient}$$

matrix

vol = element volume

$\{I_e\}$ = nodal current vector

A time-harmonic electric analysis can also be performed. In this case, the variational principle and finite element discretization are applied to the differential Equation 3.14 to produce:

$$(j\omega[C] + [K])\{V_e\} = \{Q_e^n\} \quad (\text{Eq.3.18})$$

where:

$$[K] = \int_{vol} (\nabla\{N\}^T)^T [\varepsilon] (\nabla\{N\}^T) d(vol) = \text{dielectric permittivity coefficient}$$

matrix

$$[C] = -\frac{1}{\omega^2} \int_{vol} (\nabla\{N\}^T)^T [\sigma] (\nabla\{N\}^T) d(vol) = \text{electrical conductivity}$$

coefficient matrix

$$\{Q_e^n\} = \text{nodal charge vector}$$

The matrix equation for an electrostatic analysis is derived from Equation 3.15:

$$[K]\{V_e\} = \{Q_e\} \quad (\text{Eq.3.19})$$

$$[K] = \int_{vol} (\nabla\{N\}^T)^T [\varepsilon] (\nabla\{N\}^T) d(vol) = \text{dielectric permittivity coefficient}$$

matrix

$$\{Q_e\} = \{Q_e^n\} + \{Q_e^c\} + \{Q_e^{sc}\}$$

$$\{Q_e^c\} = \int_{vol} \{\rho\} \{N\}^T d(vol)$$

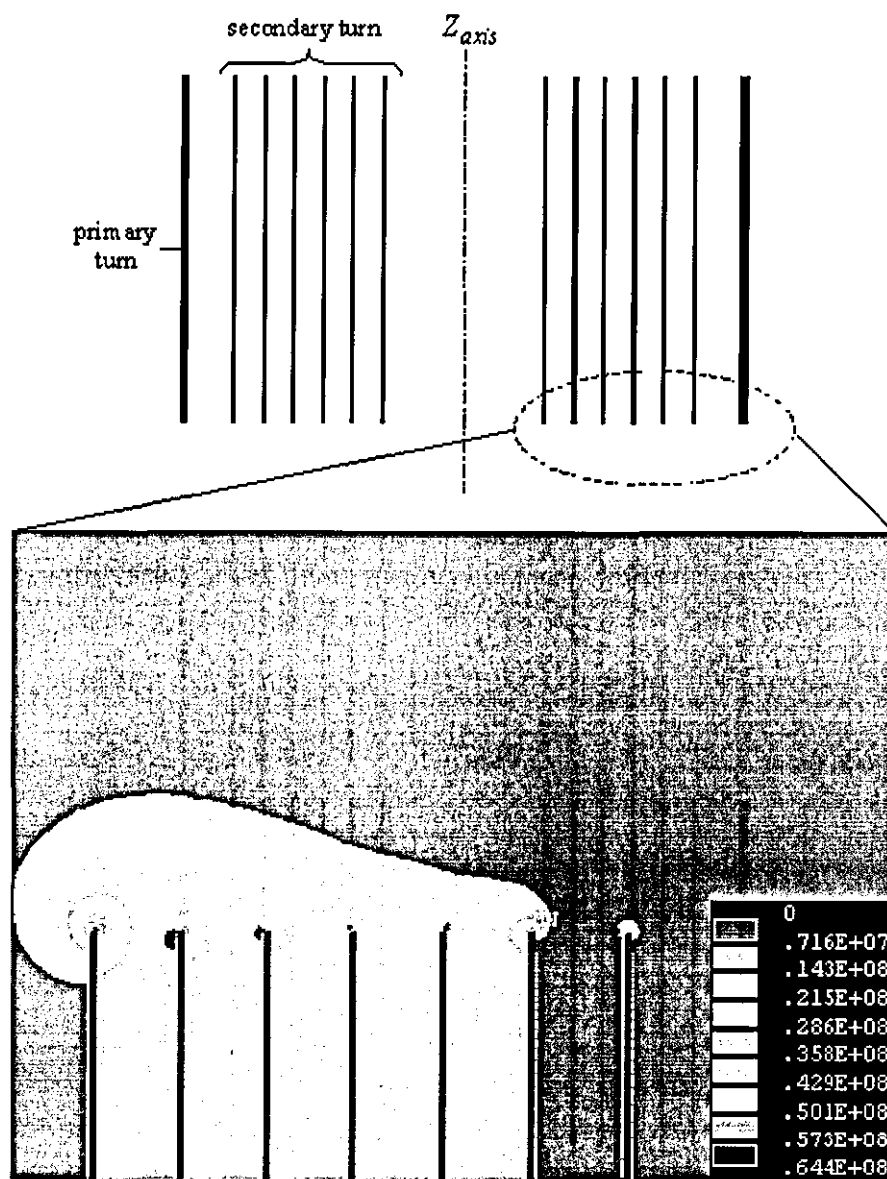
$$\{Q_e^{sc}\} = \int_s \{\rho_s\} \{N\}^T d(vol)$$

$$\{\rho\} = \text{charge density vector}$$

$$\{\rho_s\} = \text{surface charge density vector}$$

3.4 Electrical field analysis of spiral strip pulse transformer

Understanding the electric field and potential distribution is very important in the design and development of high voltage equipment and electrical insulation, since it is the intensity of the electric field that determines the onset of breakdown and the rate of increase of current before breakdown.



(a)

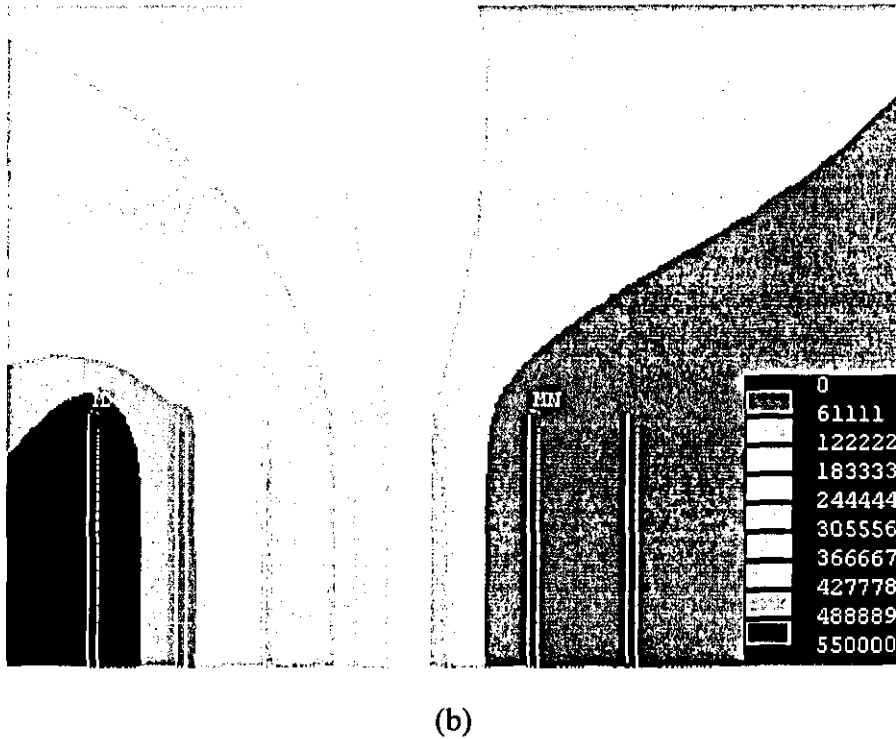


Figure 3.2 A spiral winding arrangement showing (a) electric field distribution (b) equipotential lines

Once the electric stress and distribution are properly estimated, special care can be exercised in eliminating the stress in those regions where it is expected to be high, such as in the presence of sharp points. Electric field control methods form an important component of the overall design of equipment, otherwise higher stresses will trigger or accelerate aging of the insulation and lead to its failure.

The spiral winding arrangement shown as an example in Figure 3.2 is a seven parallel cylindrical conductor electrode system, with the outside cylinder representing the single-turn primary coil and connected to the ground at 0 kV . The other six cylinders represent the 6-turn spiral-strip secondary coil with the outside turn also connected to the ground. The voltage of the cylinders are set at 500 kV , 400 kV , 300 kV , 200 kV , 100 kV and 0 kV respectively. The radius of the concentric secondary turns can normally be considered to be much greater than the pitch of the spiral, when the inter-turn electric field is almost radial and is very close to that produced by two flat parallel plates having an area equal to the surface area of two adjacent turns regarded as cylinders. With spiral-strip transformers, the voltage standoff is largely a

function of the radial thickness of the secondary winding, because the turns directly overlay each other. The winding stack has therefore a radial voltage gradient between the high-voltage inner turns and the low-voltage outer turns. The principal weakness of simple spiral strip windings is their tendency to break down from the thin edges of the strip. An arc breakdown typically emanates from the edge of one of the final turns, flashes across the insulation margin, and closes with the low-voltage primary. Such breakdowns practically always damage the insulating film in the margin and leave a heavy carbon path through the oil.

3.4.1 Edge effect

Although the ideal electric field between two parallel plates will be perpendicular to the plates and have a uniform distribution, near the edges there will be some distortion of the field and a corresponding enhancement. That is associated with equipotential lines emerging from between the turns and bending sharply around the edges, as shown in Figure 3.2 (b), which shows how severe the edge effect are, i.e. how different the edge field is compared with the interior field.

In a spiral-strip HVT, thin copper foil is normally used as the winding conductor. Since the foil is very thin, often less than a millimetre, a very large field enhancement occurs at the edges of the winding conductors. In FEA, for electrodes with a very small radius or a sharp edge, higher order polynomials can be used to approximate the potential distribution within the corresponding elements when a much finer mesh must be used. But the accuracy is sometimes inadequate, because of the limitation on the smallest size of element that can be used and the approximation to a curved path by small line segments. Attention must clearly be paid to this, since the electric stress may in reality be higher than the simulation predicts. From practical experience, field enhancement in the edge regions limits operation of a bare spiral strip to 300 to 400 *kV*, even with the best insulating films and oils.

3.4.2 Field enhancement factor

It is often possible to obtain a good estimate of the electric field in a certain region of a transformer by idealizing the geometry to such an extent that the field can be calculated analytically. This has the advantage of exhibiting the field as a function of several parameters so that the effect of changing these and the corresponding affect on the field can be appreciated.

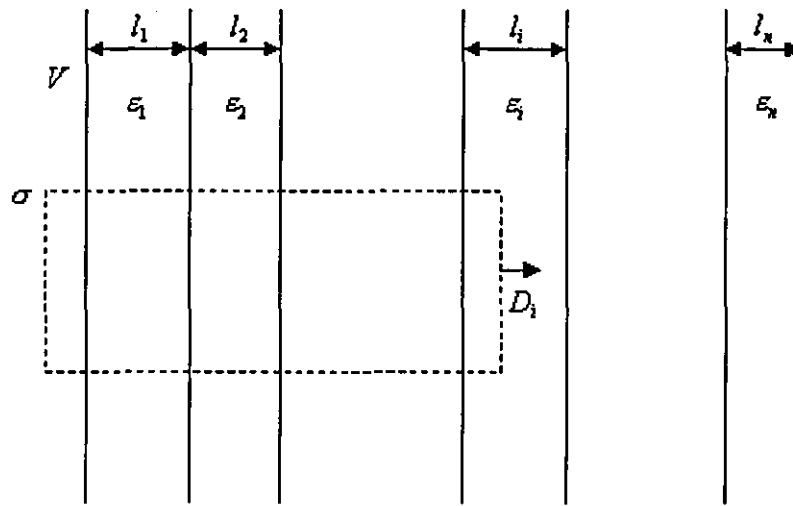


Figure 3.3 Geometry of a planar layered insulation structure

As an example, consider the layered insulation structure having the planar geometry shown in Figure 3.3. This could represent the major insulation structure between two cylindrical windings having large radii. The disc structure can be further approximated as a smooth surface, so that the resulting field calculation would be representative of the field away from the corner of the discs.

$$\int_S \mathbf{D} \cdot d\mathbf{A} = q \quad (\text{Eq.3.20})$$

where \mathbf{D} is the displacement vector, $d\mathbf{A}$ is a vectorial surface area with an outward normal, and q is the charge enclosed by the closed surface S .

One of Maxwell's equations is used to solve Equation 3.20. Because of the assumed ideal planar geometry, the surface charge density on the electrode at potential V is uniform and, for example, is designated σ in Figure 3.3. An opposite surface charge of $-\sigma$ exists on the ground electrode. Note that both electrode potentials could be raised by an equal amount without changing the results. Only the potential difference matters. The materials are assumed to have linear electrical characteristics so that

$$D = \varepsilon E \quad (\text{Eq.3.21})$$

holds within each material, where the permittivity ε can differ within the various layers as shown in Figure 3.3.

Because of the planar geometry, the D and E fields are perpendicular to the planes of the electrodes and layers. Thus if we take our closed surface to be the dotted rectangle shown in Figure 3.3, which has a certain depth into the figure, so that the two vertical sides actually represent surfaces of area A , the only contribution to the integral of Equation 3.20 which is non-zero is that part over the right vertical surface where the displacement vector has the uniform value labeled D_i in the figure. Thus, for this closed surface Equation 3.20 becomes

$$D_i A = q = \sigma A \Rightarrow D_i = \sigma \quad (\text{Eq.3.22})$$

Using Equation 3.21 applied to layer i , Equation 3.23 becomes

$$E_i = \frac{\sigma}{\varepsilon_i} \quad (\text{Eq.3.23})$$

The potential V can be written by definition as

$$V = - \int E \cdot dl \quad (\text{Eq.3.24})$$

where the line integral starts at the 0 potential electrode and ends on the V potential electrode. In terms of the E fields in the different materials and their thickness l_i , Equation 3.24 becomes

$$V = E_1 l_1 + E_2 l_2 + \dots = \sum_{j=1}^n E_j l_j \quad (\text{Eq.3.25})$$

Using Equation 3.23, this can be written

$$V = \sigma \sum_{j=1}^n \frac{l_j}{\epsilon_j} \quad (\text{Eq.3.26})$$

solving for σ and substituting into Equation 3.23 yields

$$E_i = \frac{V}{\epsilon_i \left(\sum_{j=1}^n \frac{l_j}{\epsilon_j} \right)} \quad (\text{Eq.3.27})$$

Letting l be the total distance between the electrodes so that $l = l_1 + l_2 + \dots$ and defining the fractional lengths by $f_i = \frac{l_i}{l}$, Equation 3.27 can be expressed as

$$E_i = \frac{(V/l)}{\epsilon_i \left(\sum_{j=1}^n \frac{f_j}{\epsilon_j} \right)} = \frac{E_0}{\epsilon_i \left(\sum_{j=1}^n \frac{f_j}{\epsilon_j} \right)} \quad (\text{Eq.3.28})$$

where E_0 is the electric field between the electrodes if there is only one layer of uniform material between them.

A somewhat better estimate can be made of the electric field in the major insulation structure between two coils if the geometry is considered to be cylindrical, which is also useful when approximating to the field around a long cable of circular cross section. The general case of a multi-layer concentric cylindrical insulation structure is shown in Figure 3.4. The innermost cylinder is at a potential V and the outermost at zero potential, although it is only their potential difference that matters.

From symmetry, the D and E fields are directed radially. Assuming that there is a surface charge per unit length along the inner cylinder of λ , Equation 3.20 can be applied to the broken line cylindrical surface in Figure 3.4, which is assumed to extend a distance L along the axis with disc like surfaces at either end. The only contribution to the integral is along the lateral sides of the cylinder.

$$2\pi r L D_i = \lambda L \Rightarrow D_i = \frac{\lambda}{2\pi r} \quad (\text{Eq.3.29})$$

Assuming linear material, we get for layer i ,

$$E_i = \frac{\lambda}{2\pi\epsilon_i r} \quad (\text{Eq.3.30})$$

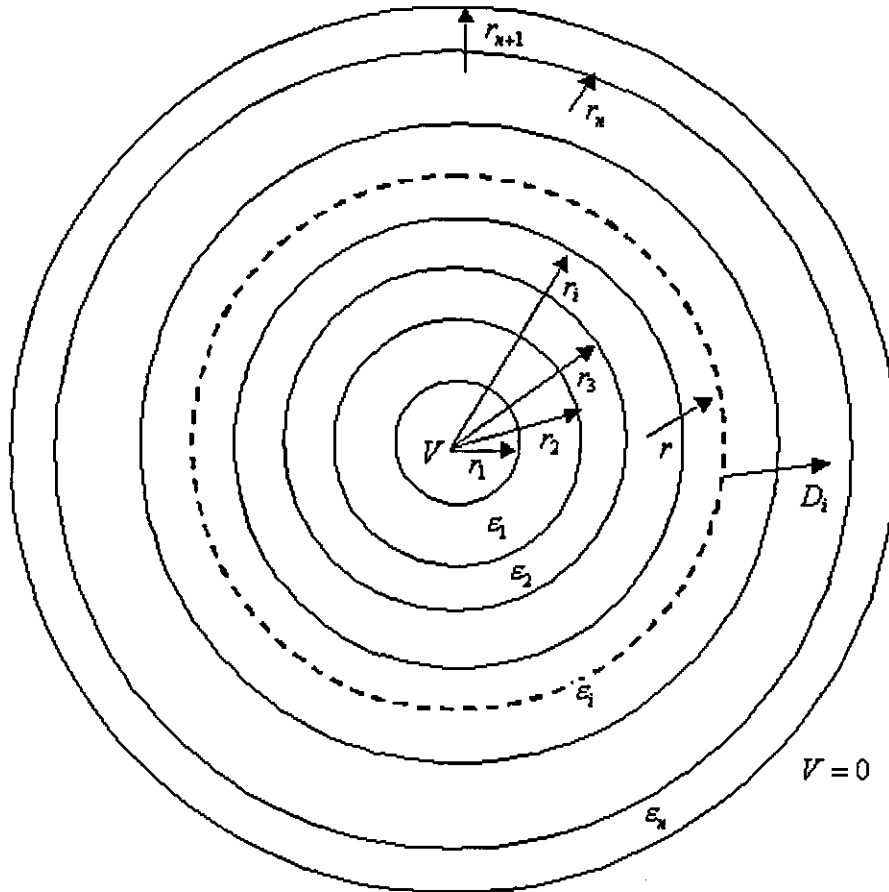


Figure 3.4 Ideal layered cylindrical insulation structure

Using Equation 3.30 and starting the line integral from the outer zero potential electrode, Equation 3.24 becomes

$$\begin{aligned}
 V &= -\frac{\lambda}{2\pi} \left\{ \frac{1}{\varepsilon_n} \int_{r_{n+1}}^{r_n} \frac{dr}{r} + \dots + \frac{1}{\varepsilon_i} \int_{r_{i+1}}^{r_i} \frac{dr}{r} + \dots + \frac{1}{\varepsilon_1} \int_{r_2}^{r_1} \frac{dr}{r} \right\} \\
 &= \frac{\lambda}{2\pi} \sum_{j=1}^n \frac{1}{\varepsilon_j} \ln \left(\frac{r_{j+1}}{r_j} \right)
 \end{aligned} \tag{Eq.3.31}$$

Solving for λ and substituting into Equation 3.30 gives

$$E_i = \frac{V}{\varepsilon_i r \left[\sum_{j=1}^n \frac{1}{\varepsilon_j} \ln \left(\frac{r_{j+1}}{r_j} \right) \right]} \tag{Eq.3.32}$$

For non-uniform fields (e.g., a cylindrical conductor-plane configuration), the maximum macroscopic field strength E_{\max} of an electrode system is more likely to be at the conductor surface. The increase in stress value as compared to that under the uniform field condition is characterized by a field enhancement factor h , thus

$$h = \frac{E_{\max}}{E_a} \tag{Eq.3.33}$$

where E_{\max} is the maximum electric field in the layer and E_a is the average electric field between two winding conductor layers, which is the same as the electric field between two infinite parallel plate. The field enhancement factor can be obtained as a function of the dielectric material factor η , area effect δ and edge effect factor β . The dielectric material factor η is determined by the dielectric constants of the insulation layer and the thickness of the multi-layered dielectric material in an inhomogeneous field configuration as stated in Equation 3.28. In a homogeneous field configuration, η is 1.

In practice, all conductors exhibit a rough surface, with the degree of roughness being dependent upon the production process [3,4]. This inherent microscopic surface roughness leads to an increase in the field strength, which can be quantified in terms of an area factor δ . The influence of different geometric parameters upon δ can be assessed by examining roughness models, which incorporate simple protrusion geometries. However, as the microscopic geometry of

practical surfaces is extremely complex, analytical studies cannot provide the actual δ values associated with such surfaces.

To reduce any edge effects, the edge of the winding conductor is always made as round as possible, and the relation between the radius of the edge and the field enhancement has been investigated [3.2]. As an example, if the thickness of the conductors in a spiral strip winding is 0.01 cm , their length is 45 cm and the gap is 0.09 cm , the relation between radius r and the edge effect factor β is:

$$\beta = 1.0 + 1.63e^{-120r} \quad (\text{Eq.3.34})$$

where the r is in centimetres. The edge effect factor decays exponentially and approaches 1 as the radius of the edge increases.

3.4.3 Field enhancement optimisation

Extended study results of field enhancement optimization by finite element method are presented below and discussed to find an optimum design parameter of the spiral-strip pulse transformer. Several techniques had been introduced which reduce the field enhancement at the edge of the windings, with the first being to make the winding conductor edges as round as possible. The second was to control the properties of the insulation material around the winding conductor [3.3] and the third to add a coaxial shield across the margins of the secondary windings [3.4].

3.4.3.1 Round edge

To avoid the possibility of undesirable “edge effects”, such as arise from a local enhancement of the uniform gap field at the highly sharp edge of an electrode [3.5], it is essential to machine the outer edges of plane-parallel electrodes so that they have a rounded profile. The effect is illustrated in Figure 3.5. which contrasts the distribution of electric field lines associated with pairs of unprofiled and profiled

electrodes. In an ideal form, the profile must ensure that the electrode surface field never exceeds its uniform mid-gap value. This generalized requirement can be quantified by detailed field computations, which are defined in terms of the electrode separation and show that short gaps require a more highly radiussed profile than large gaps. As a result of the proven operational advantages to be gained from this precaution, electrode profiling is now adopted as standard practice in high voltage engineering.

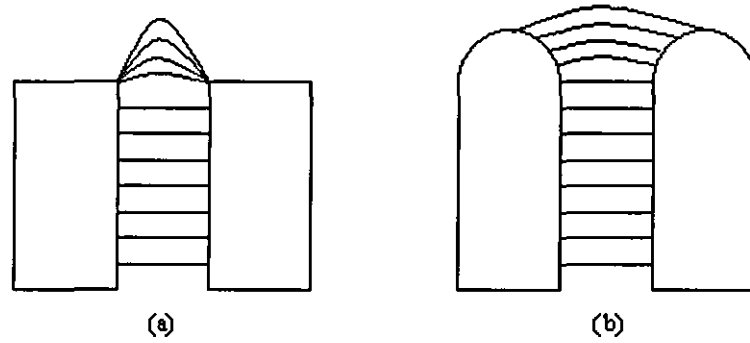


Figure 3.5 The distribution of electric field lines with (a) unprofiled electrode (b) profiled electrode

3.4.3.2 Insulation material

In an example of a paper-oil layering in planar geometry, with all the paper lumped into one layer for calculational purposes, and with subscript 1 referring to the paper layer and subscript 2 to the oil layer, the enhancement factor $\eta = E/E_0$, i.e., the ratio of the fields with and without a paper layer can be written from Equation 3.28 as

$$\eta = \frac{1}{\epsilon_2 \left(\frac{f_1}{\epsilon_1} + \frac{f_2}{\epsilon_2} \right)} \quad (\text{Eq.3.35})$$

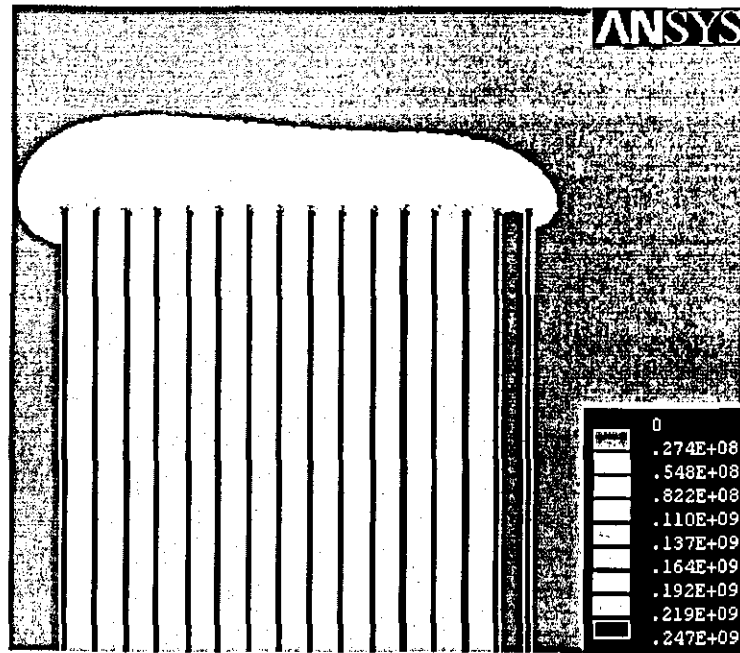
where $f_1 = l_1/l$, $f_2 = l_2/l$ with $l = l_1 + l_2$ are the fractional lengths of materials 1 and 2 respectively.

Control of the properties of the dielectric constants or the thicknesses of the layer of insulation material around the winding conductors can reduce the electric field stress. In the case of solids, breakdown originates within the volume, except possibly for thin films, so that the effect depends on the volume of the dielectric and not the electrode area. However, for liquids and gases the breakdowns generally originate from the electrodes, when the relevant parameter is the area of the electrodes. Generally, liquid and solid dielectrics have standard deviations of $>10\%$ of the mean field, and even for gases an area effect has been found in large, high-pressure dc systems.

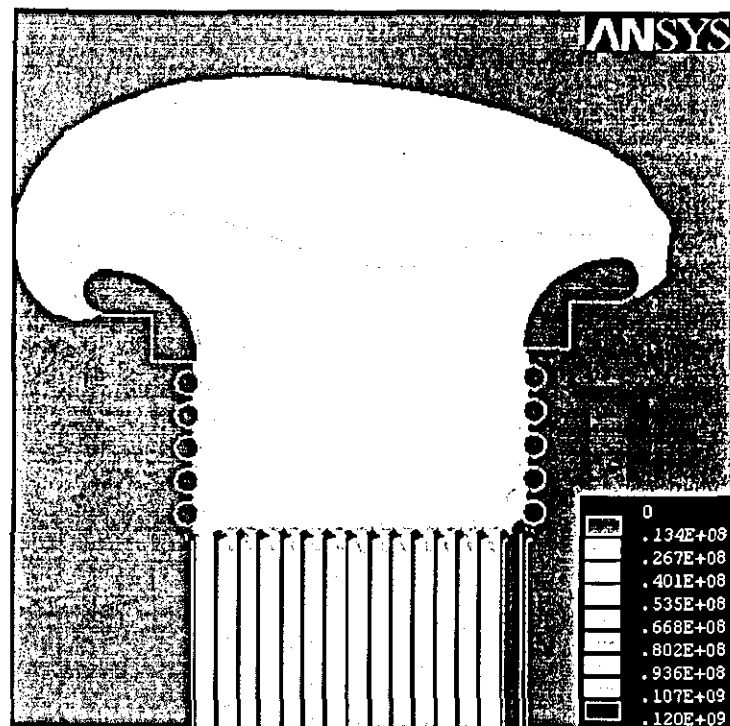
3.4.3.3 Cage techniques

If a HVT is operated in air and at a voltage above 200 kV , extremely long breakdown tracking paths have been observed along the surface of the Mylar insulator. Increasing the width of the edge of the Mylar is certainly not practical, and the best solution was demonstrated in the development of a 3 MV HVT [3.4], where a collection of axially connected split rings were used in a structure termed a ‘cage’. Cages, positioned at each end of both the primary and secondary windings (the cages for the secondary winding are mounted on the plastic mandrel), control the electric field grading in the HVT by straightening the lines of equal electric potential at the ends of the windings. Consequently, the field enhancement is greatly reduced and the edge breakdown can be prevented.

Figure 3.6 demonstrates the remarkable improvement brought about in the Loughborough 15-turn spiral-strip HVT (shown in Figure 2.3 and with the complete system data presented in [2.21]) by the cage configuration similar to that suggested in [3.4]. In Figure 3.6 the small rings have a cross-sectional diameter of 1 mm and the space between them is 1.5 mm . However, a drawback in field experimentation, where the HVT is destroyed at every shot, is the rather expensive end ring of Figures 3.6 and 3.7 confirms that this can be replaced by a simple ring of 4 mm diameter without losing any of the benefits of the original cage. Even more important, Figure



(a)



(b)

Figure 3.6 Map of electric field equal potentials for the spiral-strip Loughborough HVT

a) no cage present: maximum electric field is 247 MV/m b) using complete cage configurations similar to those in [24]; maximum electric stress is halved, 120 MV/m

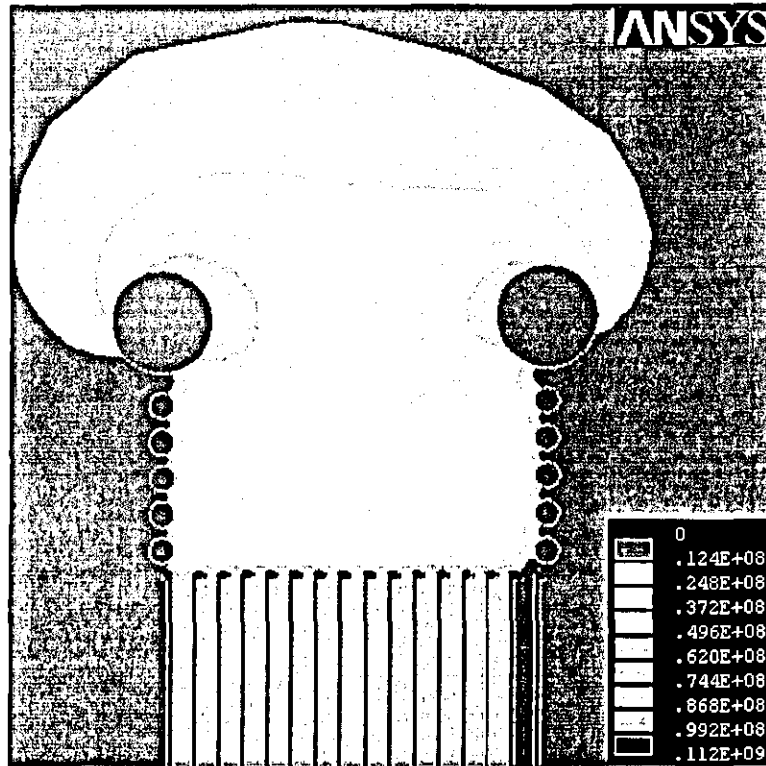


Figure 3.7 Same as Figure 3.6, but using simplified end rings: maximum electric field 112 MV/m

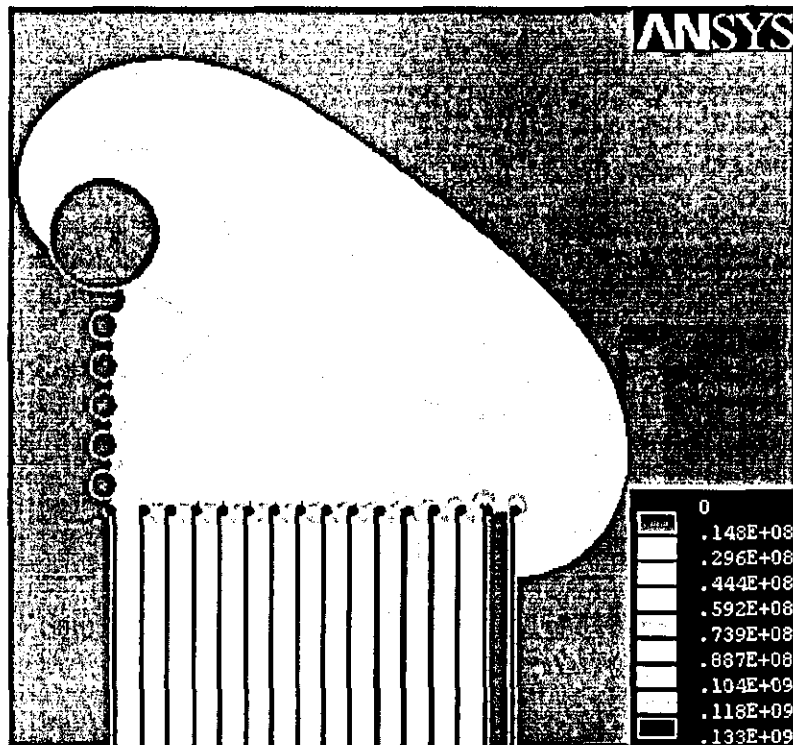


Figure 3.8 Same as Figure 3.6, but only one cage present: maximum electric field 133 MV/m

3.8 shows that the substantial reduction of the electric field intensity that is still obtained if only the secondary winding cage structures are present, could, in some cases, be sufficient to enable a MV output HVT to operate under oil. Figure 3.9 compares the smoothing of the electric field along the HVT edge using the different cage structures discussed above, that shows that the ring cage technique not only reduces the maximum electric field strength but also produces a more homogeneous distribution.

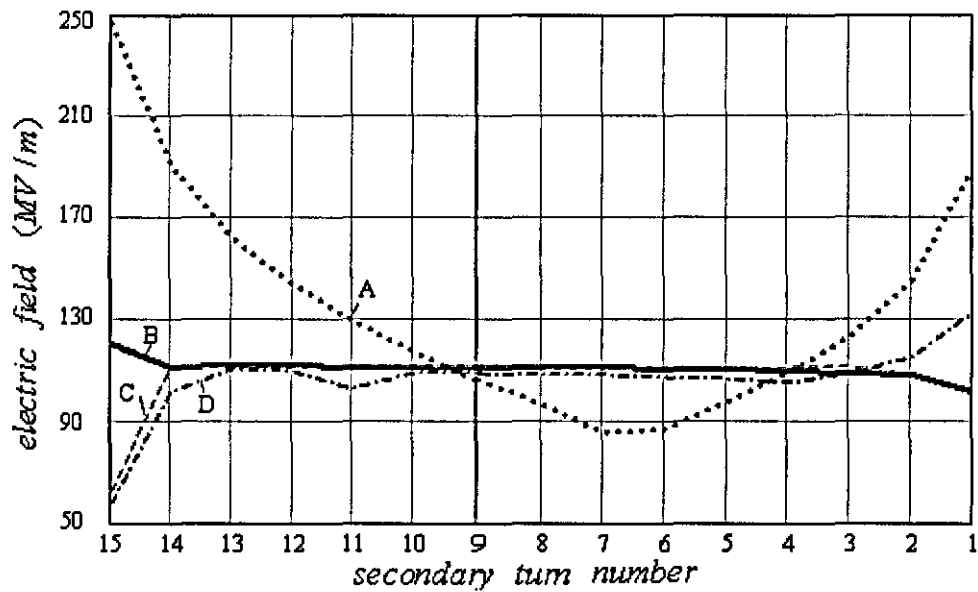


Figure 3.9 Electric field distribution along the edge of Loughborough spiral-strip HVT 15 turn secondary using various cage structures corresponding to A) Figure 3.6 (a), B) Figure 3.6 (b), C) Figure 3.7 D) Figure 3.8

3.5 Electrical field analysis of helical pulse transformer

With helical transformers, a high-voltage standoff between the primary and secondary windings is ensured by an insulated space between the windings, that can be either uniform or tapered in the longitudinal direction. When tapered, the insulation thickness increases with the voltage along the length of the coil. Turn-to-turn breakdown is common with helical transformers, arising from fast-rising voltage transients (usually less than 10 ns duration). Unlike the spiral-strip transformer, the inner-turn capacitances are all directly connected in series to ground as shown in Figure 3.10 (a) and thus a fast voltage pulse can be capacitively graded through the thickness of the winding. The turns of a helical winding are inductive as shown in Figure 3.10 (b), and the capacitance between turns and from each turn to ground are insufficient to grade fast-rising transients. Consequently, a voltage pulse approaching the full amplitude of the transient can momentarily appear across the final turns of the secondary and cause breakdown.

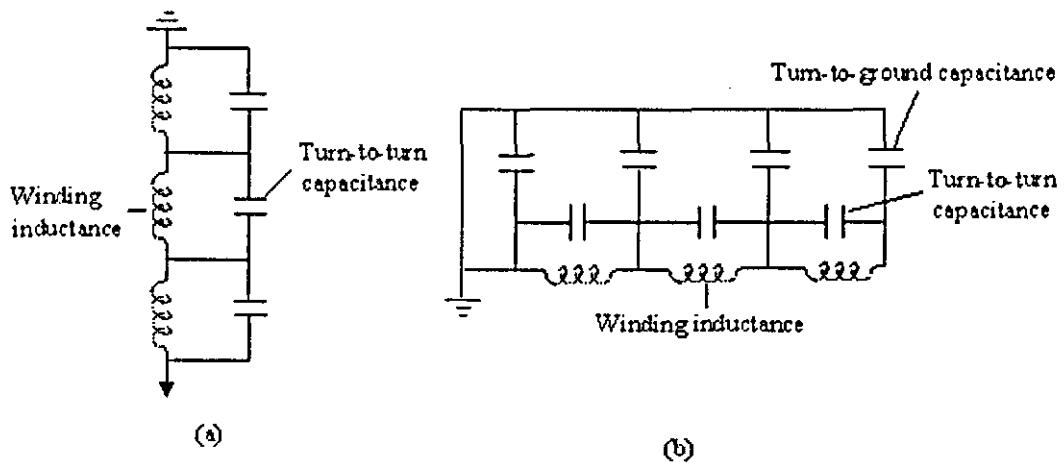
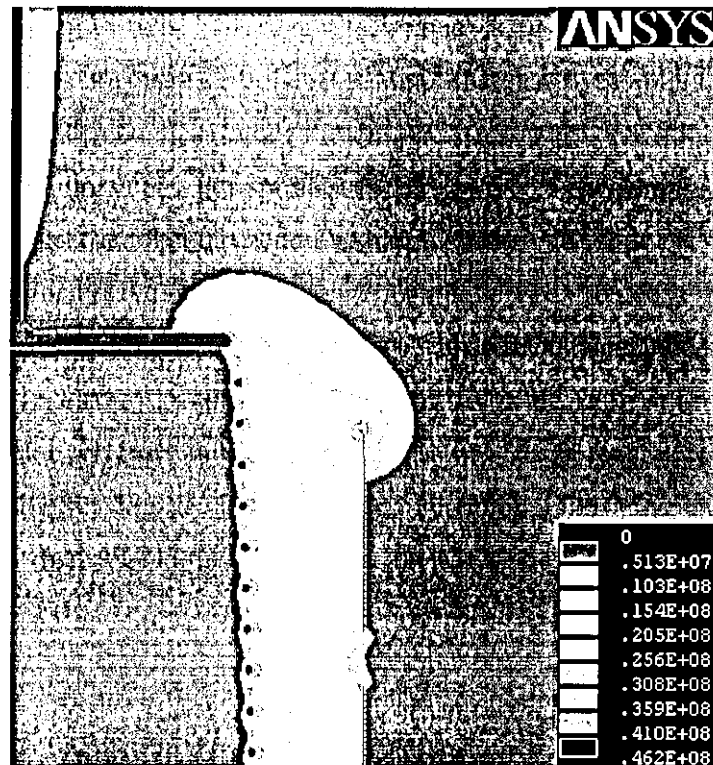


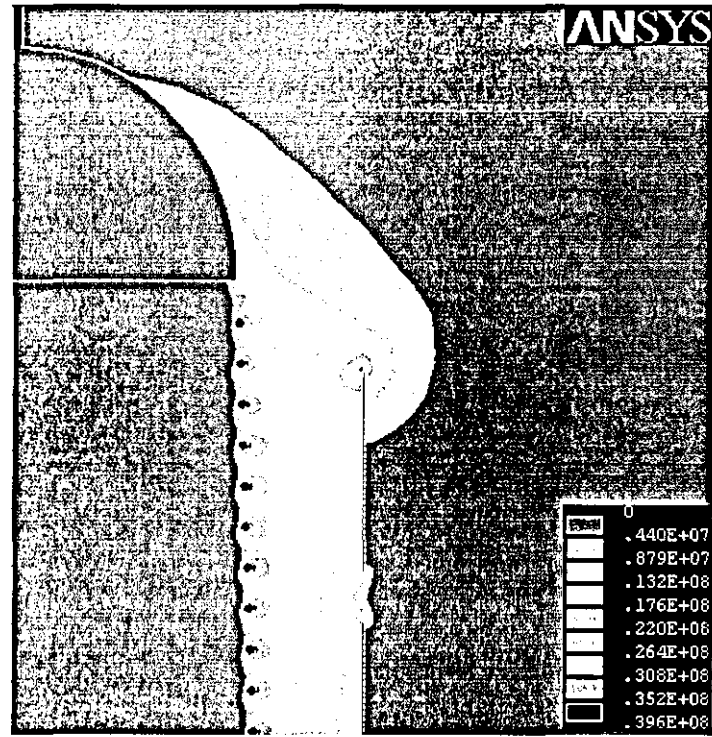
Figure 3.10 Equivalent circuit with (a) spiral-strip winding (b) helical winding

One example considered here is a helical HVT developed at Texas Tech University (TTU) [3.6] shown earlier in Figure 2.4, which has a primary winding consisting of eight turns made of copper sheet wound in a spiral and a secondary

winding located inside of the primary winding, with 50 helical turns made of copper wire. During analysis, the helical coil is decomposed into an array of parallel rings lying along a common axis. The cage technique is also applied to the helical transformer, which is a capacitive voltage-grading dish across the output turns of the helical transformer. The comparison of the electric stress with or without the grading dish is shown in Figure 3.11. For spiral-strip HVTs, the cage technique can prevent the lines of equal electric potential bending sharply at the ends of the windings which is the fatal cause for breakdown, so the cage technique is extremely efficient. While for the helical HVTs, breakdown arises mainly because the capacitance between turns and that from each turn to ground are insufficient to grade fast-rising transients, so only smoothing the electric field distribution as the cage technique does is not adequate. As show in Figure 3.11, the cage technique introduces only a small improvement less than 15% in the case of helical HVT designs.



(a)



(b)

Figure 3.11 Map of electric field equal potentials for the helical TTU (a) with grading technique (b) without grading technique

4 Design of 500 kV spiral-strip transformers with magnetic insulation

Fast and portable pulse power systems, especially in the mega volt range, have been in demand for many years, with high-voltage high-current transformers being key elements of many of the associated conditioning systems. They provide an attractive financial alternative to the Marx generator in applications such as charging the high voltage pulse forming transmission lines used with high power electron or ion beam accelerators, or driving portable X-ray sources and free electron lasers. In general, transformer systems are more compact than Marx generators, because the low-voltage primary capacitor bank is inherently a compact assembly and is not ordinarily operated in a tank of insulating oil. The resulting system requires substantially less floor space and does not involve separate oil storage and handling facilities. These simplifications yield a system that costs less to build and operate than does a Marx assembly.

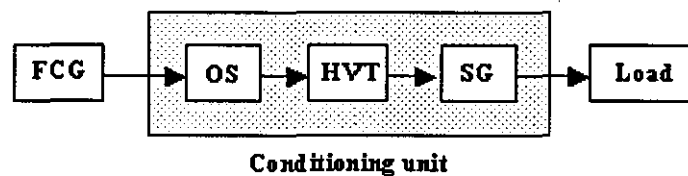


Figure 4.1 Schematic of an explosively-driven single-shot power supply for a HPM load (FCG- flux-compression generators, OS- opening switch, HVT- high voltage transformer, SG-spark gap,)

Air-cored pulse transformers can be used up to very high peak power levels (up to 10^{11} W) or ultrahigh RF frequencies. The lack of a magnetic core means they

are not limited either by magnetic saturation or the composition of the core. In a typical practical example [4.1], they form part of the energy source for a high-power microwave (HPM) system based on explosively driven flux-compression generators (FCG). In this application, an output pulse of between 0.5 and 1 MV is required to drive a microwave generator (a vircator or a MILO) and, when a substantial microwave output is required, the voltage has to be maintained almost constant for up to about 1 μs . There is no simple technical solution that would enable the opening switch (OS) that forms a vital part of such a system to operate at the high output voltage required, and the simplest way to reduce the demand on the switch is to include an air-cored step-up transformer (HVT) in the pulse-conditioning circuit [4.1], as shown in Figure 4.1.

There are two types of winding for an air-cored transformer, one being helical and the other spiral strip. The advantages of the spiral-strip type are that they can be scaled for multi-MV operation and can carry large currents ($>1\text{ MA}$) in both windings. With a spiral-strip transformer, the separation between the windings should be very small to achieve both a high flux linkage between the primary and secondary windings and a compact device. Considerable attention is however needed to prevent breakdown between the transformer windings. Since the thickness of the winding conductors is likely to be less than a millimetre, field enhancement at the edges of the winding conductor can cause a high electrical stress, resulting in electron emission and leading to electrical breakdown (flashover) between the windings. To prevent this, Mylar-polyethylene insulation can be used [4.2], but the technique is difficult to extend to voltage above 500 kV . Oil insulation can overcome this limitation [4.3] but inevitably leads to relatively heavy and bulky equipment.

The spiral-strip geometry is chosen for its high coupling coefficient and mechanical simplicity. Moreover, it is extremely favourable for the adoption of magnetic insulation, as the inter-turn electric field is radial and the magnetic field will utilize the major axial component of the single-turn primary coil rather than the much smaller radial components that would be used in a helical transformer [4.4].

The presence of a transverse magnetic field (either self-generated or externally imposed) can divert a majority of electrons from a cathode and so prevent them from reaching an anode. This so-called “magnetic insulation” has been utilized to inhibit electrical breakdown in transmission lines [4.5], ion diodes [4.6], electron beams [4.7], magnetrons [4.8], and plasma opening switches [4.9]. Unfortunately, the technique has not previously been used in high power transformers, because of a number of apparently insurmountably difficulties. However, based on previous pioneering work at Loughborough [4.4], this chapter describes the arrangement of a spiral-strip wound 500 kV transformer that uses magnetic insulation and is both lightweight and compact. The approach described can also be exploited in transformers with quite different geometries, such as high-current impedance-matching transformers [4.10] and the Tesla transformers used in electron beam accelerators and compact repetitive microwave power sources [4.11-4.12].

4.1 Transformer arrangement

4.1.1 Description of transformer arrangement

When pulsed power is fed to a high-impedance load from a low-impedance source, power-conditioning devices are required to provide impedance matching between the source and the load, and those most widely used are opening switches, closing switches and transformers. In an elementary transformer system, a low-impedance source drives the primary winding and the load resistance is connected directly to the secondary winding, with matching achieved by adjusting the primary to secondary turns ratio. This approach is simple, but limits the opportunity for shaping the waveform applied to the load.

An inductive energy storage transformer can be used as a combined impedance matching and power-conditioning system, which is particularly useful when the

timescale which characterizes the primary current source is long compared to the time scale required by the load. This approach can increase the peak power to the load, shorten its rise time and permit very compact geometry, in comparison to the capacitive discharge circuit. As shown in Figure 4.2, the transformer is fed by a pulse-conditioning circuit. The high-energy capacitor bank C is discharged through the closing switch (CS) and the transmission line (R_b and L_b) into the exploding wire array (EWA) that acts as an opening switch (OS), with the circuit being completed by the single-turn primary winding of the high-voltage transformer (HVT). When the EWA explodes, the resulting very fast dI/dt excursion generates a high secondary winding voltage. At the optimum time, the high-voltage spark-gap (SG) closes the secondary circuit of the HVT, and a fast-rising voltage pulse is produced across the high resistance load. The corresponding set of first-order differential equations are obtained from Figure 4.2 as

$$V_0 - \frac{Q}{C} = (L_b + L_f + L_p) \cdot \frac{dI_p}{dt} + (R_b + R_f) \cdot I_p - M \cdot I_s \quad (\text{Eq.4.1})$$

$$0 = R_l \cdot I_s + (L_s + L_l) \cdot I_s - M \cdot I_p \quad (\text{Eq.4.2})$$

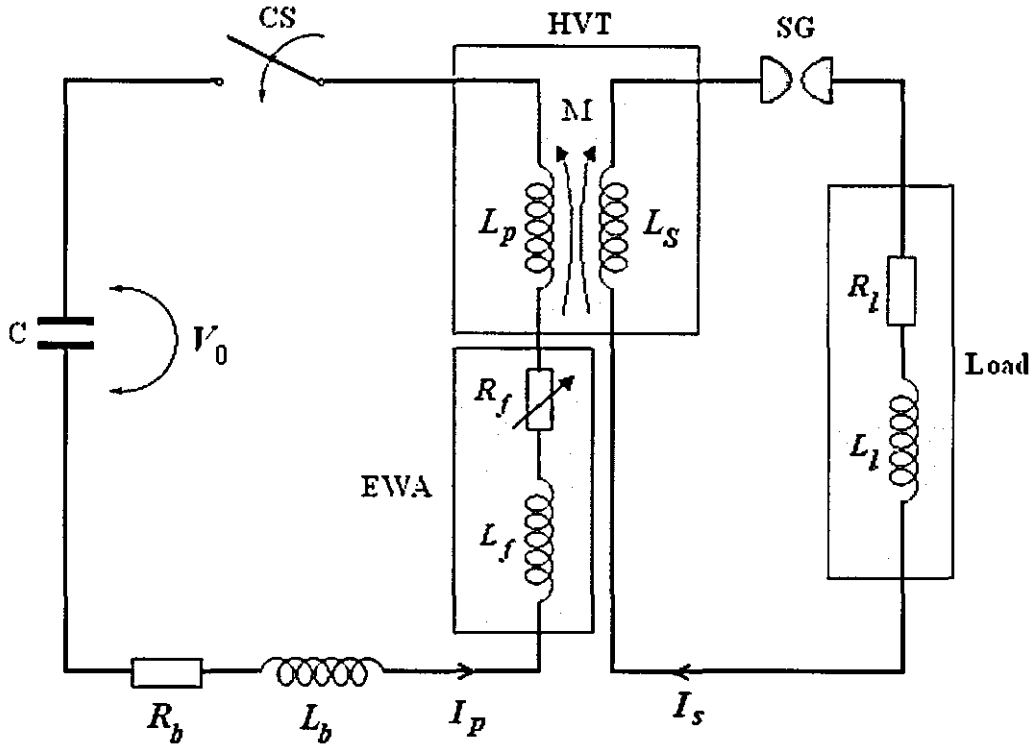


Figure 4.2 Equivalent lumped circuit of a laboratory based pulsed power system

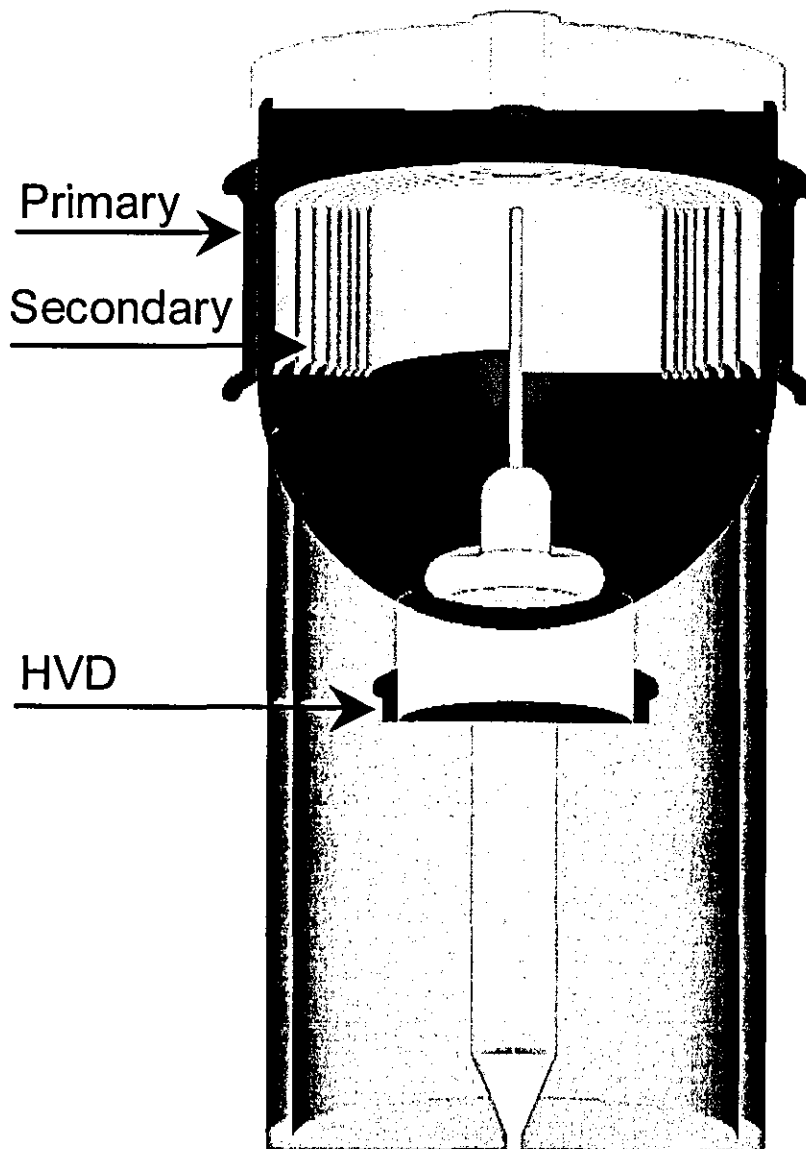


Figure 4.3 Cross section of magnetically self-insulated HVT winding arrangement and capacitive voltage divider (HVD) [4.13]

Figure 4.3 shows the physical arrangement of the magnetically-self-insulated HVT developed at Loughborough [4.13], including the built in capacitive voltage

divider on the output, and which is also illustrated in detail in Figure 4.4. A glass bell jar, positioned inside the single-turn primary, houses the 8-turn stainless steel secondary winding. The built-in high-voltage capacitive divider (HVD) (see Figure 4.3) enables the secondary voltage to be recorded.

4.1.2 Primary and secondary coil parameters and material selection

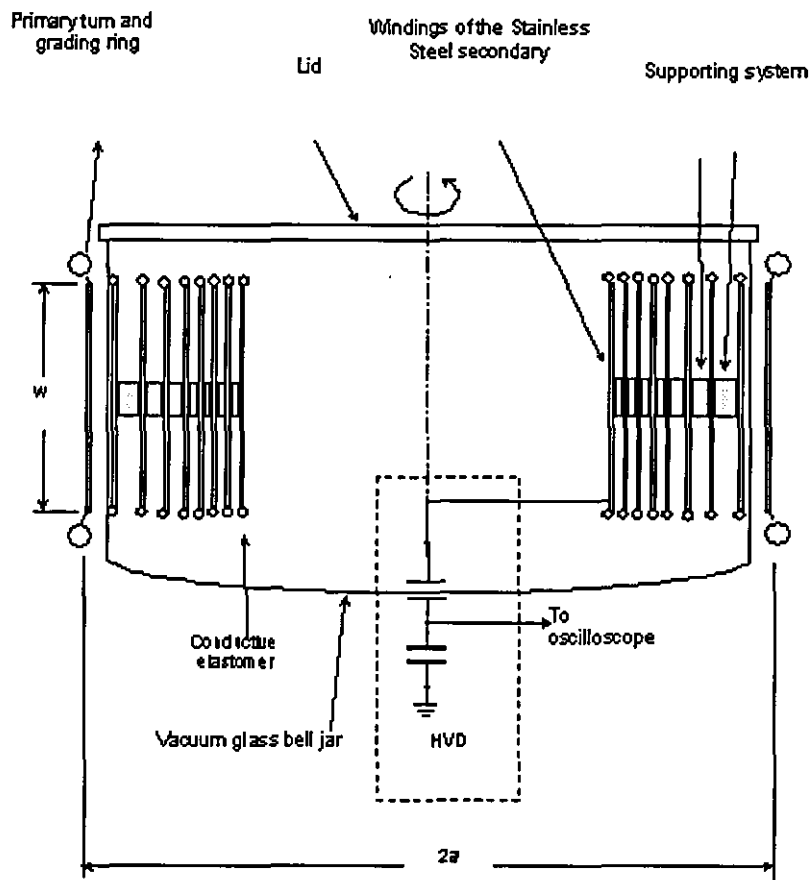


Figure 4.4 Cross section of MSI-HVT [4.13]

Much is known about the optimization of the technological parameters of a process for optimal inductor performance, though optimization of the geometry of inductors and transformers is difficult. Even for simple structures such as spirals, there are several parameters to optimize, including the radius of the spiral, the conductor width, the spacing, and the number of turns. Not much can be said in general, since the optimal geometry depends on the frequency of operation and also the required voltage.

The transformer has coaxial geometry with a single-turn primary winding to achieve a fast rise time and a multi-turn secondary winding to provide a high output voltage. The transformer secondary inductance is determined by its geometry and number of secondary turns, and increasing the number of turns results in an increased secondary inductance. To attain high reliability and repeatability, a trade off has to be made between a good coupling coefficient and a high voltage stand off. The edge of the foil is polished and has rounded edges to minimize local field enhancement and arcing.

Transformer windings are made extensively of high-conductivity copper, which in addition to its excellent mechanical properties has the highest conductivity of the commercial available metals. But copper is very soft and malleable, whereas an alternative, stainless steel is hard, which is helpful in preserving the approximately cylindrical geometry under strong electromagnetic forces. Moreover stainless steel is a very versatile material, which can maintain a significantly longer lifespan than other materials with less maintenance costs. In the present case, the primary winding is made from high conductivity copper for efficiency, and the secondary spiral-wound coil from stainless steel sheet, which is mounted vertically to preserve its approximately cylindrical geometry under the strong electromagnetic forces. This arrangement offers a simple and effective geometry for use in a high-current design that needs only a few secondary winding turns.

4.1.3 Primary conditioning system and EWA design

The primary circuit of a pulse transformer must possess a low resistance to obtain a large value of current and a low inductance to ensure a high time rate-of change of the current. The low impedance discharge path incorporates an opening switch, acting as a pulse conditioning system, with the opening switch being necessary to produce the large and rapid negative excursions of current needed to ensure the required high-voltage pulses are fed to the output load.

A fuse opening switch was used for the primary pulse conditioning system. The fuse is an electrical conductor, which during the opening process experiences a very rapid rise in resistance as a result of heating. The heating is driven by the current which the fuse is intended to interrupt, and the heating leads to melting and eventually to vaporization of the conductor. A fuse consists of a relatively thin conductor usually in a form of a foil or an array of wires, with some form of relatively heavy terminal block at each end and in a medium which may be a bulk solid, a granular solid, a liquid, a gas, or even vacuum, surrounding the conductor. Here exploding wires are used, because they are more efficient than the foils used in the earlier low-energy system [4.14], and they were designed to synchronize the occurrence of large values of current and changing current with time.

A large number of experiments were performed [4.15] to establish the optimum-tamping element for the wires. Air, water, sand (glass beads between 10 and 100 μm in diameter), epoxy and various gels (sealant) were all investigated, together with exploding wire arrays (EWAs) of copper wire with diameters between 50 and 250 μm . The well-known fact that thinner wires produce higher voltages when they explode was confirmed, although the difference between the extremes of wire size used was only 10%. Because a large number of parallel wires were required if the thinnest (and most fragile) wires were used in the EWAs, it was decided to adopt the more robust 250 μm diameter wire. It was somewhat unexpectedly found that air was the best medium in which to operate the arrays, although the normal assumption is that higher voltages are generated when the medium is water. This is probably

attributable to the fact that only very thin wires (well below $50\text{ }\mu\text{m}$ diameter) respond better in water and to the relatively short rise time of the current in the present system, which are not the conditions that applied when most of the data reported in the literature was obtained. Also from [4.15], a further important finding was that two parallel connected EWAs can generate a much higher voltage than a single EWA, which could bring about major improvements in conditioning techniques using opening switches.

A high dI/dt pulse was generated by the EWA, with a high negative dI/dt excursion. It is well known that the behaviour of exploding wires depends on a number of parameters, including the material and dimensions of the wires [4.16-4.17], the time profile of the current [4.17] and the confining medium. A model is needed to optimize the EWA parameters as a compromise with the discharge circuit performance, which is described in detailed in next section.

4.2 Filamentary modelling

Filamentary modelling was used to predict the response of the circuit incorporating the vacuum transformer and to optimize the design, which was discussed in detail in Chapter 2. The preliminary tasks were to model the behaviour of the primary conditioning system, including the EWA opening switch, to calculate the self-inductance of both primary and secondary and also the mutual inductance between them, and to solve the set of linear differential equations describing the discharge system. The final stage was to tune the parameters of the discharge circuit within achievable limitations and geometry parameters of the transformer to satisfy all the requirements.

Calculation of the self-inductances of the primary and secondary windings and also the mutual inductance between them is described in Section 2.5.2 and the filamentary representation of the spiral-strip HVT is shown in Figure 2.6 with a detailed explanation given in Section 2.10.2. System optimization was obtained and the final design was as follows. The single-turn primary winding of the transformer is of 1.2-*mm* copper sheet, with a length of 100 *mm* and an outside diameter of 328 *mm*. The 6-turn secondary winding is of 1.2-*mm* stainless steel foil, wound on a 162.2 *mm* mandrel with a length of 100 *mm* and a pitch of 10 *mm*. The 2-dimensional filamentary model gives the primary inductance as 430 *nH*, the secondary inductance as 12 μH , and the mutual inductance between the windings as 1.37 μH .

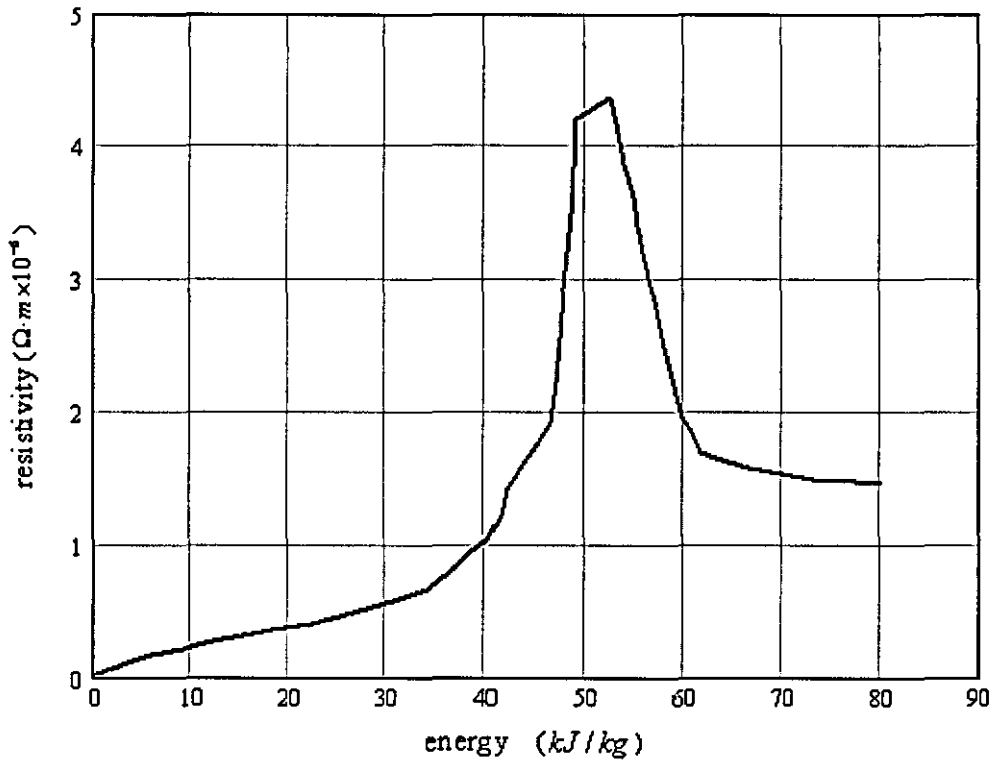


Figure 4.5 Dependence of the energy on the EWA resistivity

As an aid to the development of the EWA switching stage of the conditioning system, a simple experimentally derived curve of the EWA resistivity against input

energy (Figure 4.5) was obtained for a copper wire, from experiments using a fast-discharge capacitor bank. This model was subsequently used in the filamentary modelling program to interpret data provided by further experiments, in which an EWA opening switch was connected at the input of the transformer primary winding. Figure 4.6 shows a simplified view of the EWA, with the transmission line as a ground plate. A filamentary representation is given in Figure 4.7. The mutual inductance between two filaments and the self inductance and resistance of each filament can be calculated respectively from Equations 2.26-2.28. The total inductance L_f can be calculated from the energy method presented in Section 2.5.2 and the resistance R_f can be calculated based on the resistivity $\rho(W)$ shown in Figure 4.5. EWA optimization was obtained by matching the number of exploding wires and their length with the total system inductance.

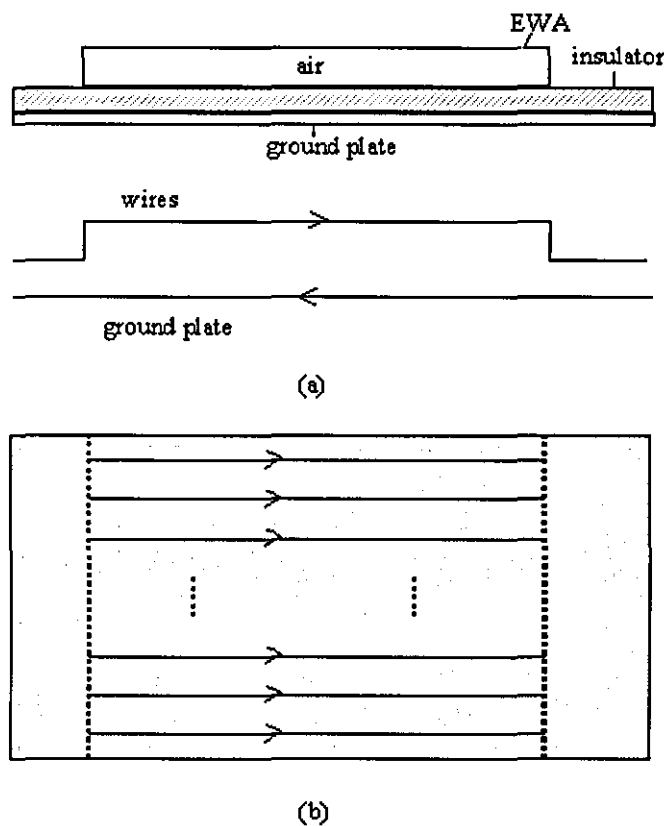


Figure 4.6 Simplified view of EWA for use in filamentary modelling

(a) side view (b) front view

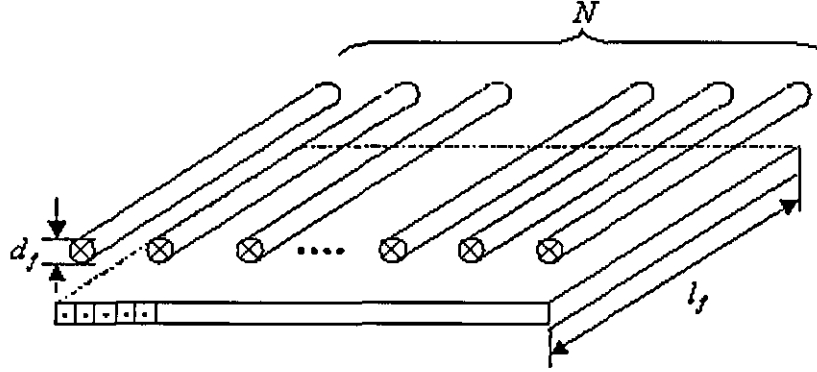


Figure 4.7 Filamentary representation of EWA

The process of building a 2D filamentary model of a transformer is described in detail in Section 2.10.2. When incorporating an EWA, Equations 2.50-2.52 can be written as

$$V_0 - \frac{Q}{C} = L_b \frac{dI_p}{dt} + R_b I_p + L_f \frac{dI_p}{dt} + R_f^{(W)} I_p + R_{p_i} I_i + \sum_{j=1}^{Np} M_{ij}^{p-p} \frac{dI_j}{dt} - \sum_{j=Np+1}^{Nt} M_{ij}^{p-s} \frac{dI_j}{dt} \quad (i = 1, \dots, Np) \quad (\text{Eq.4.3})$$

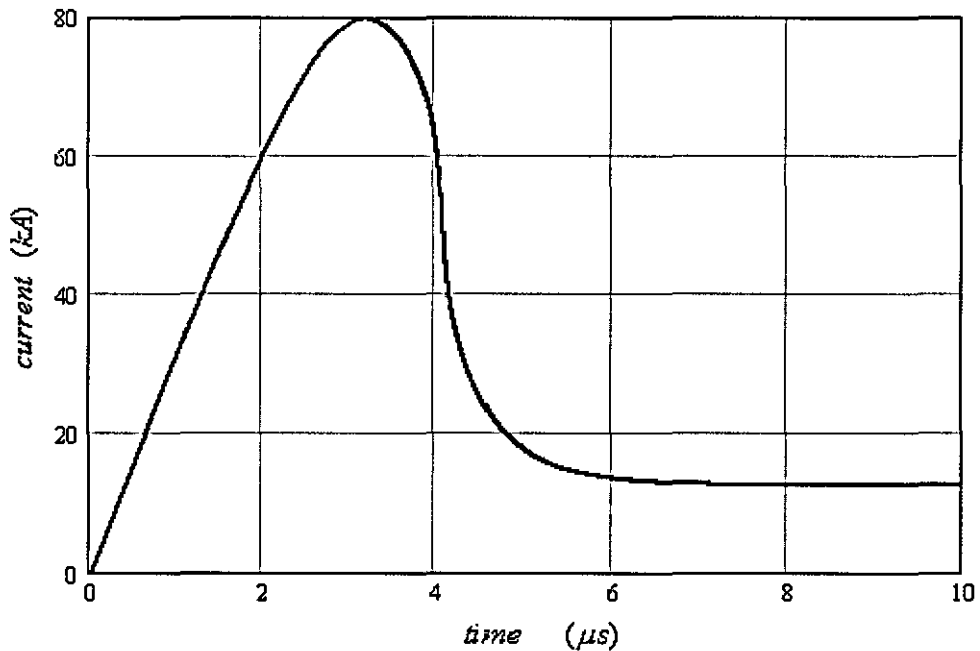
$$L_l \frac{dI_s}{dt} + R_l I_s + \sum_{k=1}^N R_{s_i}^k I_i + \sum_{j=Np+1}^{Nt} M_{ij}^{s-s} \frac{dI_j}{dt} - \sum_{j=1}^{Np} M_{ij}^{s-p} \frac{dI_j}{dt} = 0 \quad (i = Np+1, \dots, Np+ns) \quad (\text{Eq.4.4})$$

$$\frac{dQ}{dt} = I_p \quad (\text{Eq.4.5})$$

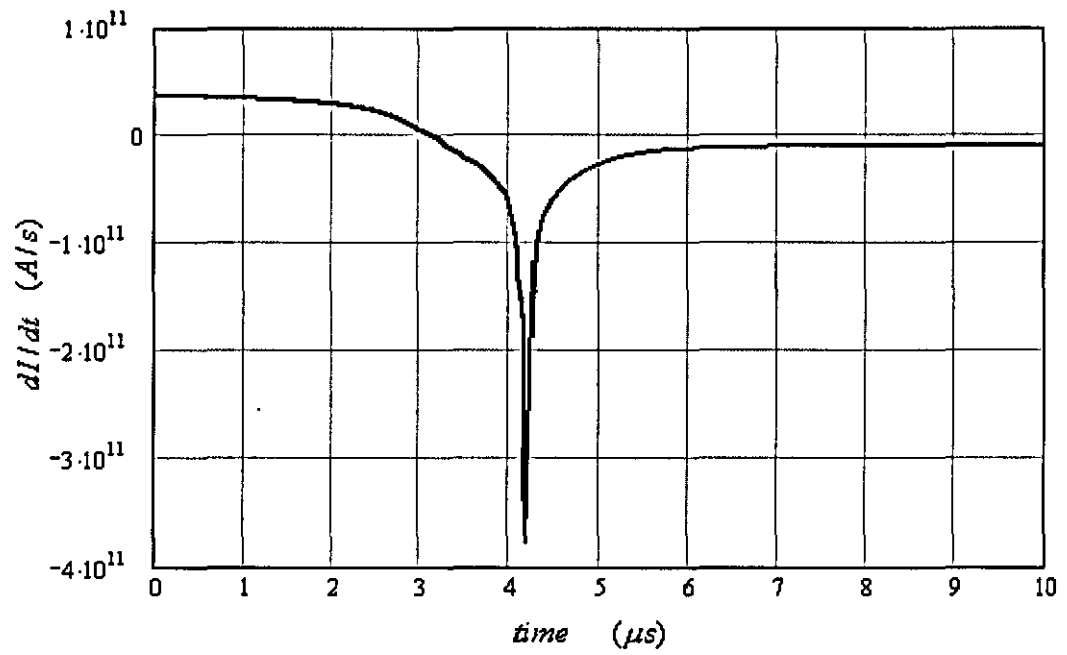
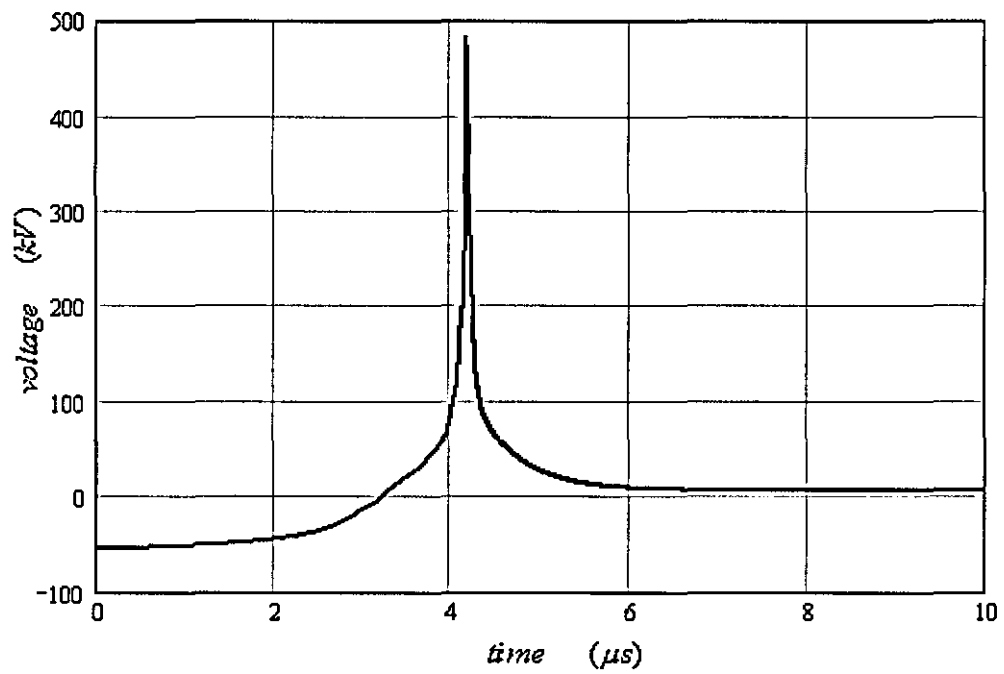
$$\frac{dW}{dt} = \frac{R_f(W)}{\text{mass}} I_p^2 \quad (\text{Eq.4.6})$$

The discharge circuit is shown in Figure 4.2, the main capacitor bank is one 52.47 μF capacitor, with an internal inductance of 7.2 nH and a resistance of 1.3 m Ω , charged to a voltage of (0-25) kV (V_0). The fuse package comprises an

exploding wire array of two to eleven OFHC copper wires of diameter $250\ \mu\text{m}$ and length $135\ \text{mm}$ - $250\ \text{mm}$. A model for the EWA opening switch resistance (R_f) was created as described in Section 4.1.3, with the experimentally derived curve of resistivity against energy being shown in Figure 4.5. The inductance of the EWA opening switch (L_f) is calculated from the model as an approximation of two parallel plates using the principle explained in Section 2.4 (filamentary model with z-current circuits). The equivalent resistance and inductance of the bank circuit, including the transmission lines is $10\ \text{m}\Omega$ (R_b) and the inductance is $20\ \mu\text{H}$ (L_b). When the initial capacitor voltage (V_0) is set at $25\ \text{kV}$ and the EWA opening switch uses 6 copper wires with length $135\ \text{mm}$, the primary current, its time rate of change and voltage output can be obtained from the filamentary model as shown in Figure 4.8, from which we can see during pulsed operation, the very high rate of change with time of the primary winding current, leading to a correspondingly high voltage V being induced in the secondary winding shown in Figure 4.8 (c).



(a) primary current

(b) di/dt of primary current

(c) load voltage

Figure 4.8 Primary current, its time rate-of-change and voltage output from the spiral-strip transformer

4.3 Breakdown analysis

The breakdown mechanism of a high voltage vacuum gap is physically complex. Not only does its behaviour depend on a large number of macroscopic parameters, e.g. the electrode material, their geometry and separation, the residual gas pressure etc., but also upon the ill-defined microscopic properties of electrode surfaces as for example determined by their preparation procedures and the operational history of the gap. Equally, there is a wide range of physical phenomena, such as electron emission, microparticle emission, electrode heating and thermal diffusion processes, which can operate in such a complex regime and significantly influence the performance of a gap.

The final stage of vacuum breakdown is an arc discharge due to an ionization/multiplication process in the metal vapour generated by the two electrodes. However, there is no unified approach to describing the breakdown initiating mechanisms. The prevalent explanations can be classified as electron emission-induced and micro-particle-initiated breakdown, which can also be classified as cathode-initiated breakdown and anode-initiated mechanism. Generally speaking, for short gaps of $d \leq 2\text{ mm}$, where instabilities predominantly stem from electron emission processes, the breakdown is field-dependent, with the minimum d-spacing being determined by a critical breakdown field that is typically $3 - 5 \times 10^7 \text{ V/m}$ [4.18]; in practical terms this equates to 20 kV being safely supported by a 1 mm gap. On the other hand, for large gaps with $d \geq 5 \text{ mm}$, where micro-particle processes are thought to become dominant [4.18], the breakdown becomes voltage-dependent so that the minimum d-spacing has to be determined from a relation of the form $V_b \propto d^m$. Actually, to understand the breakdown initiation mechanism in practical HV vacuum insulation, a number of other physical processes must be accounted for, such as electrode material and surface preparation, ion bombardment, surface diffusion, and surface contamination as well as electrode surface micro-topography changes.

The breakdown voltage is also influenced by atmospheric pressure. For two uniformly spaced parallel-plane electrodes, the breakdown voltage decreases with the barometric pressure until a 340 *V* minimum value is reached. This phenomenon is due to the fact that, as the molecular density of the air is reduced, there is a greater likelihood that a free ion can traverse the space between electrodes without running into some other particle. However, as the pressure is reduced even further, the required voltage for breakdown increase once again, because the more limited number of air molecules makes ionization more difficult.

In a spiral-type structure with thin-film electrodes, the electrode field at the film edge is considerably enhanced; hence the breakdown initiation will be dominated by the electron field-emission process. In fact, no matter which process initiates the edge breakdown in thin-film electrodes, they are all very similar in their outcome, with the extremely high electric field at the edge causing electron or charged particle emission (including ions) from the edge area, which are accelerated by the electrical field and hence gain energy. They will finally hit the opposite electrode, causing a breakdown if their energy is sufficiently high. On the basis of the above process, possible solutions to improving the insulation capability of the thin-film vacuum gap are to reduce the electric field at the thin film edge to eliminate the electron/charged particle emission, as discussed in Chapter 3, or to block electron/charged-particle movement in the vacuum gap. Using a magnetic field to change the trajectory is one of the solutions.

4.4 Implementation of magnetic insulation technique

It is well known that the presence of a transverse magnetic field can increase the electric strength of vacuum insulation [4.19-4.20]. In spiral-strip geometry, the inter-turn electric field is radial and the magnetic field will utilize the major axial

component of the single-turn primary coil rather than the much smaller radial component. In addition, the undesirable space charge gradients caused by charge accumulation occurring in the case of planar geometry are avoided [4.21]. Bunching of the drifting electrons at the edges of the cathode can result in a buildup of space charge electric field E_r parallel to the surface of the cathode. Unless this field is shorted out by a sufficiently high conductivity of the cathode or covered by the cathode plasma, an undesirable $E_r \times B$ drift of electrons toward the anode will take place. A group of electrons then crosses to the anode followed by the growth of another electron clump at the edge as shown in Figure 4.9 (a), which is blamed for the failure of magnetic insulation in planar geometry. The space charge accumulation also happens at the end of cathode in cylindrical geometry, with insulation resulting from the azimuthal magnetic field B_θ crossed with the radial electrical field E_r . The electrons are induced to drift toward the end of the cathode region when an axial electric field is established, which when crossed with B_θ forces the electrons to drift radially towards the anode.

In spiral-strip geometry, as shown in Figure 4.9 (b), the insulation is provided by the axial magnetic field B_z crossed with the radial electrical field E_r ; the electrons flow radially and drift axially, which is later confirmed by the MAGIC simulation.

4.4.1 Magnetic self-insulation

4.4.1.1 Theoretical description

Figure 4.10 shows a simplified model of the MSI-HVT. For a single-turn primary winding carrying a current I_p , the magnetic flux density generated inside the coil is mostly axial, and because the secondary winding current is negligible the field will be mostly axial within the whole transformer. Neglecting any spatial field variation, the axial magnetic flux density is given by $B_p = KI_p$, where the coefficient K depends only on the coil geometry. To simplify the approach, the secondary winding

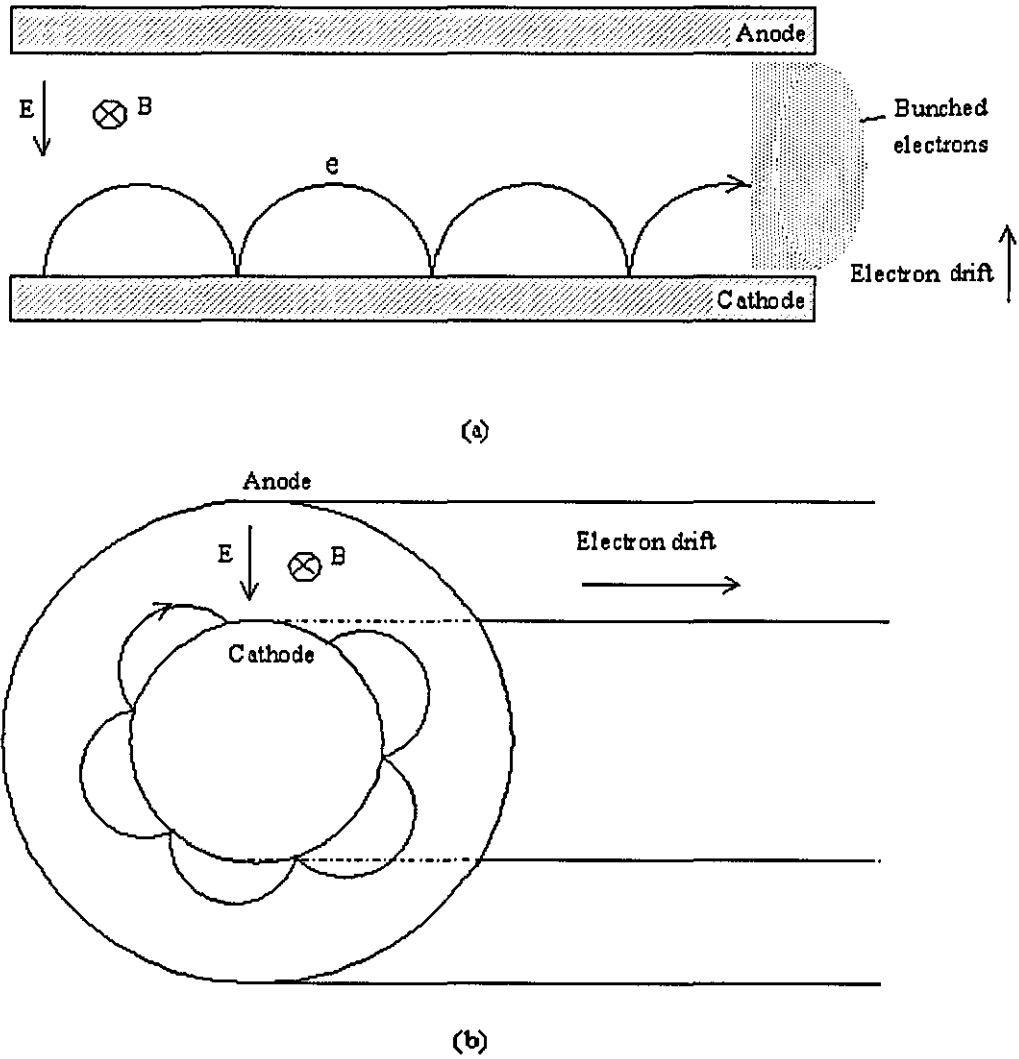


Figure 4.9 Mechanism for magnetically-insulated gap

(a) electron drift in a magnetically-insulated gap representing planar geometry or cylindrical geometry with insulation resulting from the azimuthal magnetic field with radial electrical field. (b) electron drift in cylindrical geometry with insulation resulting from the radial magnetic field with radial electrical field.

is approximated by a collection of N thin concentric slotted cylinders connected in series and separated by different distances δ_i ($i = 1, \dots, N-1$) with $\delta_i > \delta_{i+1}$ as shown in Figure 4.10 (b). In each cylinder an EMF is generated as $V_i = -M_i dI_p/dt$, where M_i is the mutual inductance between the primary turn and the i_{th} secondary turn, which can

be readily calculated as described in Section 2.11.1. The positions of the (cylindrical) turns are such that the ratio $(M_{i+1}+M_i)/2\delta_i$ is approximately constant, which generates an almost equal electric field stress between turns.

It is known [4.22] that when the distance between two electrodes in vacuum is larger than 1 mm, the relation between voltage breakdown (v) and gap distance (δ) is no longer linear and is given by

$$v = k\sqrt{\delta}, \quad (\text{Eq.4.7})$$

where $k = 9.3 \times 10^5 \text{ V/m}^{1/2}$ is a constant obtained by using data from [4.23]. Equation 4.7 can thus provide a way to predict the breakdown voltage between each pair of turns and allow calculation of the characteristic vacuum breakdown voltage V_{break} of the HVT without magnetic insulation.

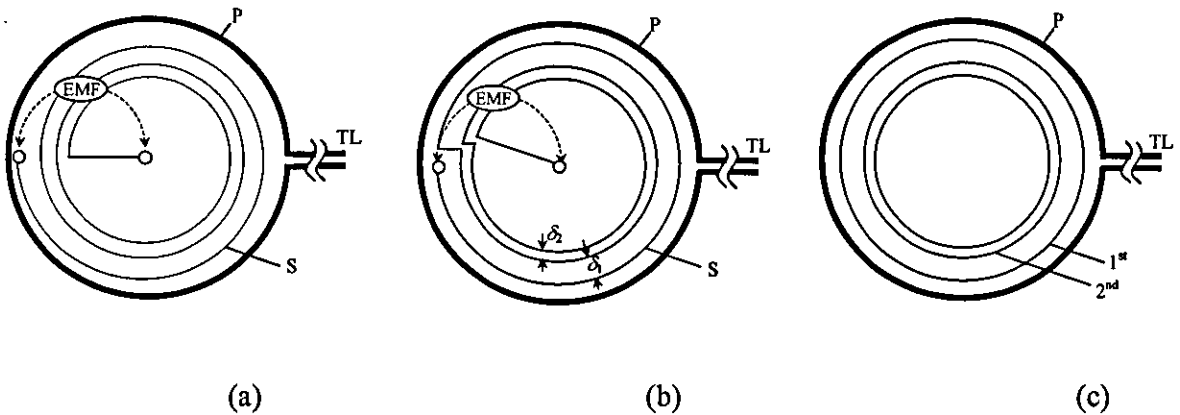


Figure 4.10 Schematic view of a 3-turn spiral-strip HVT

(a) view of the real transformer (b) simplified circuit, P—primary, S—secondary, TL—flat transmission line (input), EMF—electromotive force (c) simplified secondary winding geometry adopted in MAGIC® simulations.

According to Equation 4.7, the gap breakdown voltage increases with the gap length. Breakdown occurs when $E\delta_i > k\sqrt{\delta_i}$, or $\delta_i > (k/E)^2$, which occurs at the largest gap if the inter-gap electric field is assumed to be the same for all gaps. Consequently, the magnetic insulation criteria will be calculated for δ_1 . Between two adjacent finite width cylinders, the electric field distribution is however non-uniform and the maximum electric stress E generated between the two edges can be approximately calculated using the geometry dependent field enhancement factor F_i [4.24], as $E = F_i V_i / \delta_i$. If V_s is the (secondary) HVT output voltage $V_s = \sum V_i$, and if E is common to all pairs of turns, then

$$E = V_s / \sum_{i=1}^{N-1} (\delta_i F_i) \quad (\text{Eq.4.8})$$

With relativistic effects, displacement currents and initial electron velocities all neglected, the minimum magnetic field B_{\min} required to provide the insulation can be simplified from Equation 1.9 as

$$B_{\min} \geq \sqrt{\frac{2E}{\alpha d}} \quad (\text{Eq.4.9})$$

Substituting Equation 4.8 in Equation 4.9 with $d = \delta_1$, an approximation is provided to the minimum conditions for magnetic insulation as

$$I_p^{\min} \geq \frac{1}{K} \sqrt{\frac{2V_s}{\alpha \delta_1 \sum_{i=1}^{N-1} \frac{\delta_i}{F_i}}} \quad (\text{Eq.4.10})$$

where I_p^{\min} is the minimum primary current required to generate an output voltage V_s . Because I_p and V_s are both easily measured, Equation 4.10 can be used for comparing theory and experiment.

Equation 4.10 represents however only a first-order estimation and the following paragraphs therefore present detailed theoretical considerations using the electric and magnetic field distributions, taking into account the actual geometry of the grading structures. A 3D particle dynamics study then provides an accurate

prediction of the current-voltage characteristic of a real device, and is for use as both a design tool and to aid the understanding and interpretation of experimental results.

4.4.1.2 Estimation of magnetic insulation characteristics

A simple way to estimate the primary current required for generating 0.5 MV with the MSI-HVT above described is to use Equation 4.10 with data provided in Table 4.1. Field enhancement factors F_i for each pair of turns are given in the Table 4.1 and were calculated from [4.24]:

$$F_i = 0.9 \frac{\delta_i}{2r \ln \left(\frac{\delta_i + t}{2r} \right)} \quad (\text{Eq.4.11})$$

The coefficient K in Equation 4.9 can be approximated as $K = \mu_0/(w+0.9a) = 5.08 \times 10^{-6} \text{ T/A}$ from the inductance formula in [4.25].

Using these data, Equation 4.10 states that it is necessary for a current of more than 33.7 kA to flow through the primary circuit in order to generate a voltage of about 0.5 MV with the present MSI-HVT.

Table 4.1 Main parameters of the simplified MSI-HVT model

i	1	2	3	4	5	6	7
$\delta_i \text{ (mm)}$	11	9	7	6	5	5	4
F_i	2.31	2.18	2.09	2.08	2.13	2.13	2.32
$(M_i + M_{i+1})/2 \delta_i$	2.49	2.45	2.63	2.62	2.72	2.37	2.59
(10^{-5} H/m)							

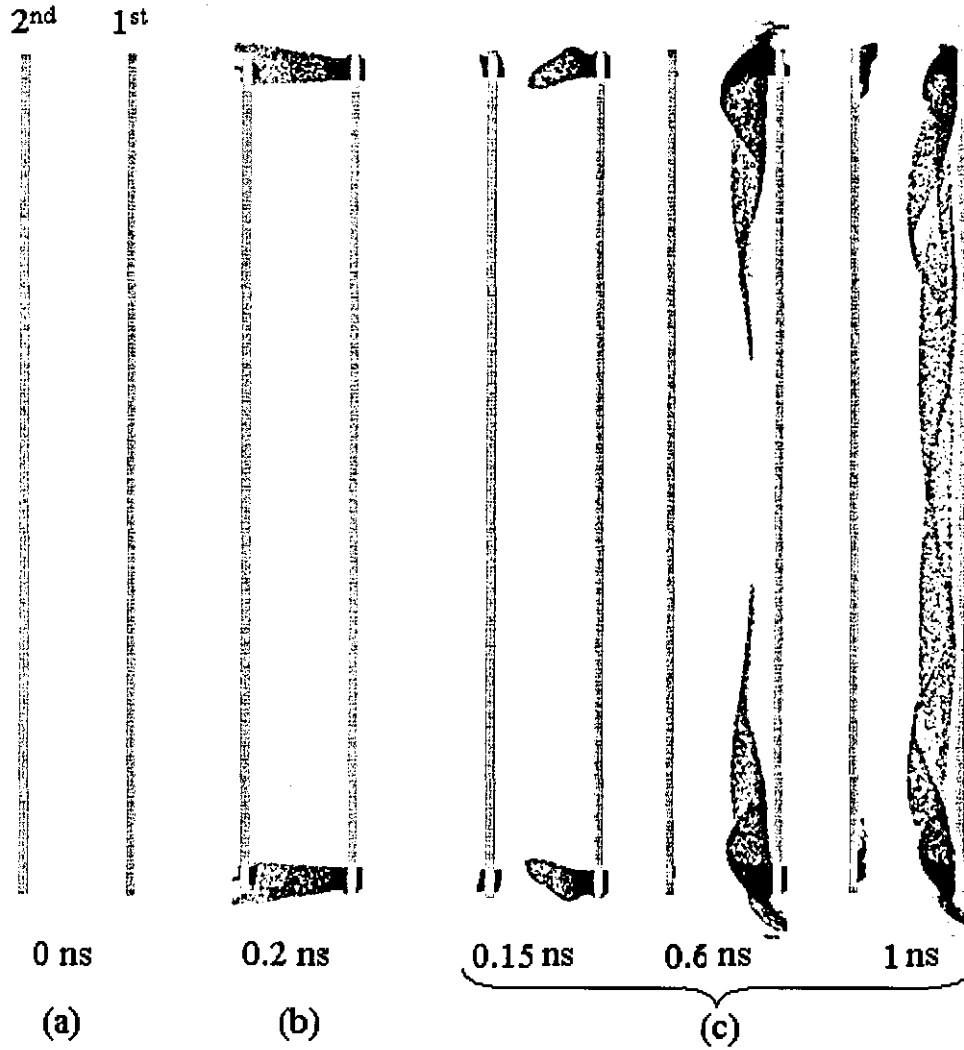


Figure 4.11 Examples of electron particle dynamics simulations in MAGIC® using the geometry of Figure 4.10 c showing (a) initial situation at $t = 0$, (b) breakdown at $I_p = 0$ kA, $V_s = 500$ kV, (c) magnetic insulation at $I_p = 49$ kA, $V_s = 500$ kV

Figure 4.10 (c) shows the simplified secondary winding geometry used in MAGIC® simulations [4.26], where the cylinders are unslotted and there is a fixed background field together with a constant voltage applied between each pair of cylinders.

MAGIC® calculations (Figure 4.11) begin in this time-frozen environment at an arbitrary moment, which is unrelated to the time of the experiment. The MAGIC® software version utilizes an embedded explosive electron emission model with a threshold field of 2.3×10^7 V/m. It is assumed that, based on the calculated 3D

trajectories, electrical breakdown occurs whenever an electron travels between adjacent turns, due to an insufficiently high flux density (i.e., insufficient primary current). Two representative examples of electron particle dynamics are presented in Figure 4.11, one showing a breakdown and the other with sufficient primary current to enable magnetic insulation. Note that at the two edges the radial component of the magnetic field has a different orientation, which is responsible for the symmetric dynamics of the electrons in both r and z directions. Also note that the electron flow is 3D with the circular trajectories (along the θ direction) not shown in Figure 4.11. By finding the primary current required to avoid breakdown for various secondary (output) voltages, a current-voltage characteristic can be obtained and a current of 49 kA predicted to be necessary for generating 0.5 MV.

4.4.2 Magnetic insulation with imposed field

4.4.2.1 Imposed field system design

Assuming that the dI/dt pulse fed to the primary winding generated by the circuit of Figure 4.2 has the waveforms of Figure 4.8, it is obvious that the most severe situation arises immediately the main capacitor discharge begins, when the secondary voltage step and the consequent high electric field appearing across the secondary windings necessitate strong insulation, and unfortunately at this time the primary winding current is close to zero. Once the initial situation has passed, the main current discharged into the primary winding of the transformer becomes sufficient to produce the magnetic field required for self-insulation.

Using the simplified method described in Section 4.4.1.1, the characteristic vacuum breakdown voltage V_{break} of the HVT can be calculated using Equation 4.7 as 350 kV, which is much more than the initial secondary voltage (about 30 kV). But initial experiments at $V_0 = 15$ kV experienced however an early breakdown about 1 μs after the beginning of the capacitor discharge. One solution suggested is that an externally produced field can be used to provide magnetic insulation at the initial time.

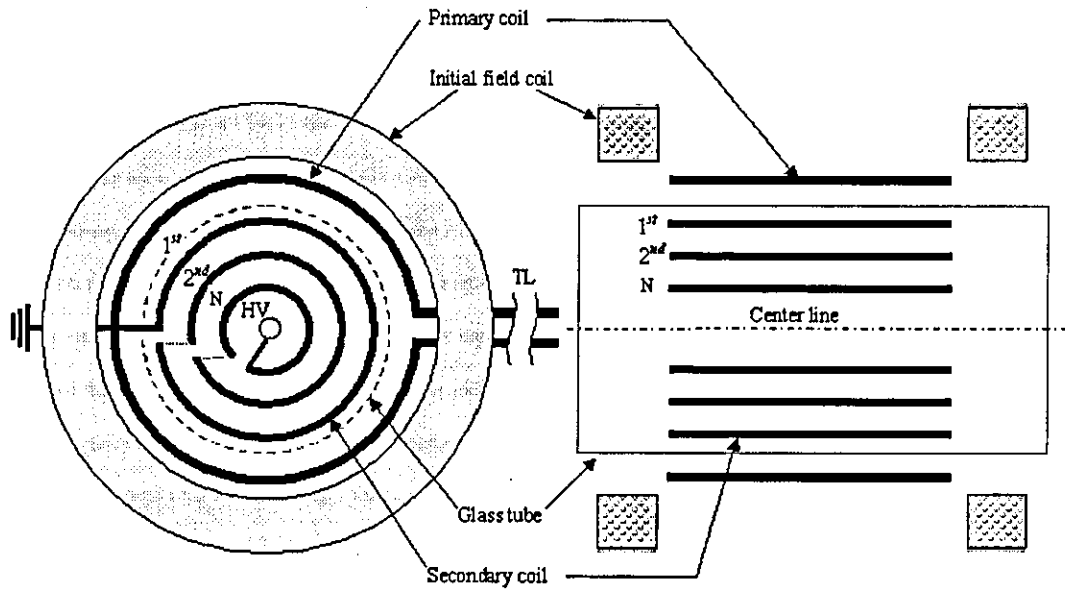


Figure 4.12 Schematic drawing of spiral-strip high voltage transformer arrangement with the injection of external magnetic field

TL-flat transmission line (input), HV- high voltage output.

An initial field can be established based on the existing capacitor bank with a capacitance of $2400 \mu F$ and a stored energy of $14.7 kJ$ at the rated voltage of $3.5 kV$. The aim of the initial coil design is provide the maximum magnetic field, considering the inductance influence, field strength efficiency and manufacturing difficulties, and each coil used was of $5 mm$ overall diameter enamel insulated copper wire with eight layers each having eight turns and wound on a plastic mandrel $330 mm$ in diameter as shown in Figure 4.12. The axial distance between the two coil centres is $120 mm$ and the total equivalent resistance and inductance of the initial field coil system are $230 m\Omega$ and $5.55 mH$. It was easy to maintain a current of up to $2 kA$ with a rise time of $5 ms$.

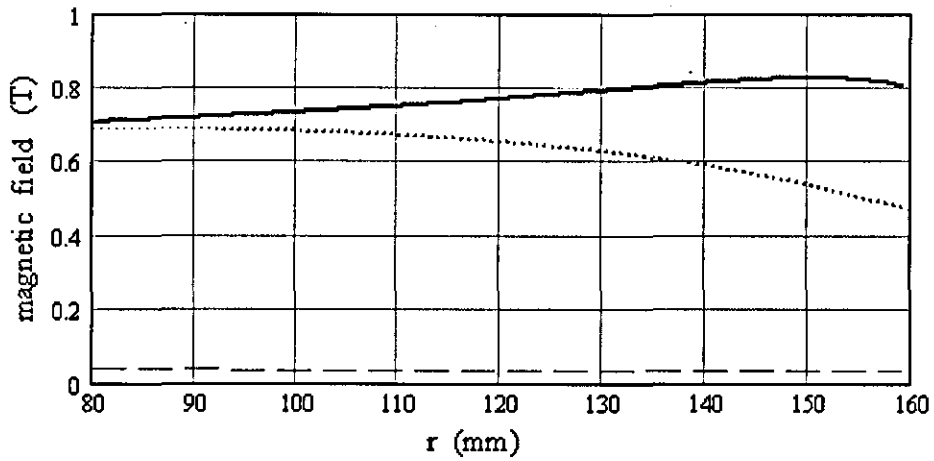
4.4.2.2 Evaluation on the efficiency of the imposed field

The axial component of the magnetic flux density produced by a single-primary turn, with its centre at the origin, is obtained by using the techniques in [4.27] as

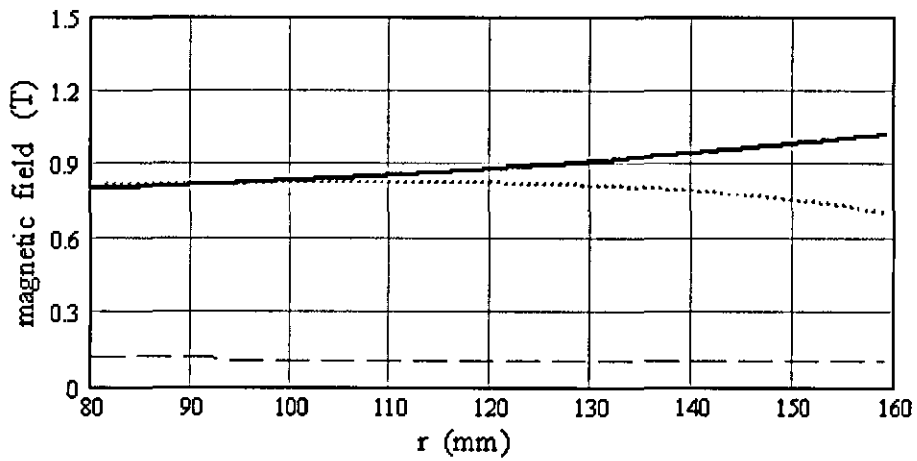
$$B_z = \frac{\mu_0 I}{4\pi h} \int_0^\pi \frac{1 - X \cos \theta}{1 + X^2 - 2X \cos \theta} \times \left(\frac{1 - Z}{\sqrt{(a/h)^2 (1 + X^2 - 2X \cos \theta) + (1 - Z)^2 / 4}} + \frac{1 + Z}{\sqrt{(a/h)^2 (1 + X^2 - 2X \cos \theta) + (1 + Z)^2 / 4}} \right) d\theta \quad (\text{Eq.4.12})$$

where I , a , h are, respectively, the current, radius and length of the coil and $X = r/a$, $Z = 2z/h$. The current density is assumed to have a uniform axial distribution.

The efficiency of magnetic insulation is examined at the time the main capacitor discharge begins and also when the secondary voltage pulse reaches its peak. When the main capacitor discharge begins, although the primary winding current is close to zero, there is an external axial magnetic field in the gap that is generated by the initial coils. The magnetic field was examined at Figure 4.13 (a), which shows the radial distribution of axial component of the magnetic flux density at $t = 0$ and when the magnetic field was applied by both primary winding and initial coil, which was presented in Figure 4.13 (b). The above analysis shows the transformer is well insulated over the duration of the voltage pulse applied across the secondary windings with the initial field injection.



(a)



(b)

Figure 4.13 Axial component of magnetic flux density variation along a radial line

(a) $t = 0$ (b) $t = 4.25 \mu s$

At the edge of windings (red line), at the centre (blue dot), the critical magnetic field required for magnetic insulation calculated from Equation 4.9 (solid line).

5 Design of a 1 MV HVT with external magnetic insulation

As stated earlier, the aim of an ongoing research project at Loughborough is to develop compact and lightweight transformers working in the MV range and for use as high-voltage pulse generators. The use of conventional forms of transformer insulation cannot compare in either weight or volume with the magnetically insulated devices that are the focus of the research.

This chapter describes the design of a 1 *MV* Tesla transformer [5.1] in which the magnetic insulation is established by an external auxiliary power source, unlike the magnetic self-insulation described in Chapter 4. It is based on a Tesla transformer operated in vacuum and used in a dual-resonant mode, with a description given of the novel constructional details that preliminary testing has shown are necessary to ensure satisfactory operation.

5.1 Introduction to the Tesla transformer

The Tesla transformer, invented by Nikola Tesla, is a high voltage two-coil resonant device, which is capable of developing high potentials ranging from a few hundreds of kilovolts up to several megavolts. The voltage produced is AC, at a frequency typically between 50 and 400 *kHz*. Operation is normally in a pulsed mode, with pulse widths varying from some nanoseconds up to several hundreds of microseconds, according to the specific application.

The Tesla transformer has been known for more than a century in the scientific community and has been used in several applications. A significant number of papers, articles and books have been written about the theory of its operation [5.2-5.5] and its practical construction [5.6-5.7]. Today the Tesla transformer, also known as the Tesla coil, is embedded in numerous devices in the fields of radio, television, telecommunications, medicine, and it is used in many applications where high frequency currents are required. It is also important in the generation of high voltages and can be a good simulator of lighting by generating high-voltage pulses with an amplitude of several megavolts and emitting electrical discharges that can easily extend for several meters.

5.1.1 Brief history of Tesla coil

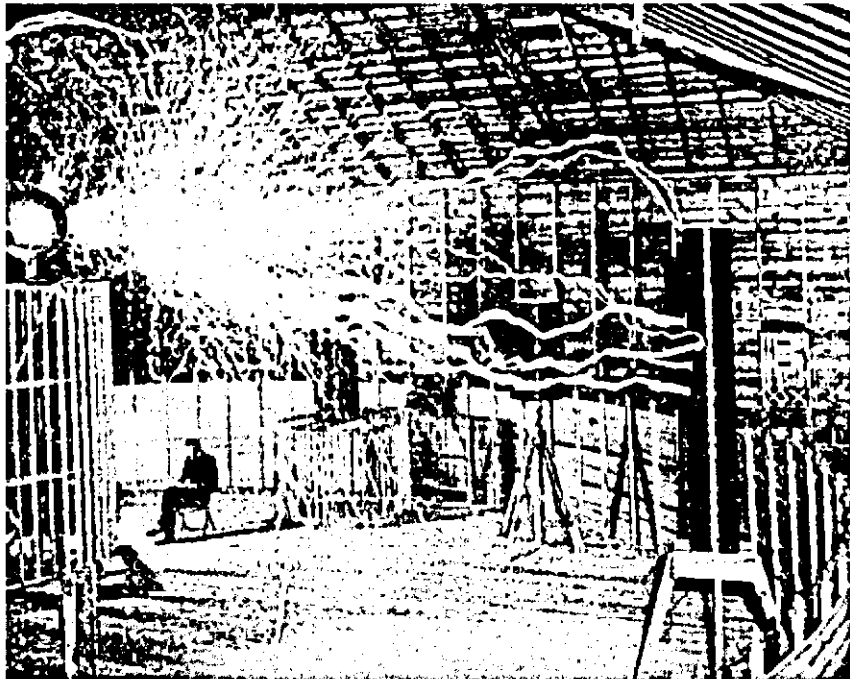


Figure 5.1 Nikola Tesla in his laboratory with his transformer (a photograph taken in Colorado Springs during an experiment on December 31, 1899)

Nikola Tesla (1856 - 1943) was an important inventor who held 112 U.S. patents and had a similar number of patents outside that country. He invented the induction motor and three-phase power in 1888, and the Tesla coil in 1891. In 1893 he devised a system for the wireless transmission of intelligence and the Tesla Oscillator was patented in 1900. His fundamental contributions in both power and communications have truly changed the course of human history.

The first record of Tesla's air-cored transformer is dated 1891 and appeared in one of his patents [5.8], where the high voltage developed was intended to be used for electric lighting. The circuit converted low frequency currents into "*currents of very high frequency and very high potential*". A much more refined version of the Tesla Coil that bears his name "*a resonant step-up transformer that develops extremely high voltages*" appeared in his patent [5.9] dated 1914. This coil generated high-frequency oscillations by means of a resonant LC "tank" circuit, which was periodically made and intercepted through the action of a spark gap or rotary switch.

Different groups of people have been interested in Tesla transformers for many years. In the first half of the 20th century, industry manufactured small-sized Tesla transformers to generate high-voltage for a number of applications (e.g. X-ray generators, electrocution and coagulation for veterinary purposes). Research groups have replicated Tesla's original transformer designs and have produced new ones, according to the increase in the number of useful materials becoming available (plastics for insulators in particular). Many attempts have been made to improve on the rudimental measurements Nikola Tesla originally made and to provide a robust and proven mathematical model covering all operational principles of Tesla transformers.

Tesla transformers are widely used nowadays as test sources in the routine testing of insulators and insulating materials [5.10]. For example, traditional tests performed with high DC voltages might not reveal the true aging effects that occur in insulation materials during repeated operation of high-voltage switched-mode power supplies. The Tesla transformer avoids non-linear effects because it is air-cored. As the size of its coils is increased, the distance between its windings

can also be increased, so that the stray capacitance becomes smaller and, although difficult to control, the wave-shape of the damped high-frequency oscillations of Tesla transformers are similar to the typical transient disturbances found in power systems (e.g. caused by switching operations or by arcing to ground). They are widely used as test sources in routine tests [5.11] and also for generic insulator testing [5.12] and the synthetic testing of circuit breakers[5.13].

Tesla transformers are also used in research on lightning discharges, and while cloud-to-ground lightning has been studied extensively, cloud-to-cloud and cloud-to-air discharges still need to be understood more thoroughly as they are difficult to measure [5.14]. Field observations of lightning reveal little of the physics of the phenomenon; the propagation process and the leader velocity are best studied by the scaling of laboratory sparks [5.15-5.16] generated by Tesla transformers.

Another important application of Tesla transformers is the generation of high-voltage pulses. Sources of short high-voltage pulses with a high repetition rate are of interest in a number of situations. For instance, they can be used to generate electromagnetic radiation to measure the size of objects with a very high precision or to produce powerful microwave pulses with 3-*cm* wavelength [5.17]. Numerous papers have been published with particular emphasis on the use of a Tesla transformer in relativistic electron beam generators [5.6-5.6], with its main advantages over the Marx generator being a high repetition rate of operation and low cost because of the fewer capacitors used. Tesla transformers have become well established, and other reported applications include a series of compact and portable devices to drive cold cathode e-beam tubes, X-ray tubes [5.18], the rapid spectral analysis of minerals and jewels, and in radiography.

5.1.2 Simplified theory of operation

The Tesla transformer comprises two coupled, frequency-matched LC circuits, as shown in Figure 5.2. The primary circuit is of high capacitance C_p and

low inductance L_p , and the secondary is of low inductance L_s and high capacitance C_s .

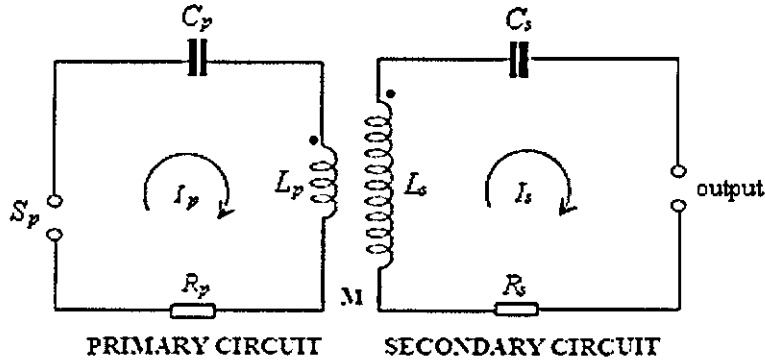


Figure 5.2 Tesla transformer basic schematic diagram

When C_p is sufficiently charged, the potential difference between the spark gap electrodes S_p causes the gap to fire and allows current to flow. The energy stored in the primary capacitor C_p is fed to L_p , and C_p and L_p form the primary circuit with a resonant frequency defined by the values of C_p and L_p . The magnetic field generated by L_p is coupled with the secondary coil L_s , which together with the secondary circuit capacitor C_s forms a second resonant circuit. If its resonant frequency is near to that of the primary circuit, an extremely high potential is developed at the output terminal, and the secondary circuit voltage can easily reach between 100 kV and several MV. Once the capacitor C_p is discharged, the spark gap S_p ceases conducting and the process just described is repeated.

During the primary oscillation energy is passed back and forth between the primary capacitor and the primary inductor. Some of the energy is dissipated in the spark gap, which causes the oscillation to decay relatively rapidly with time. The oscillating current in the primary induces a similar oscillating current in the secondary coil, and energy is transferred from the primary to the secondary circuit.

The energy transfers back and forth between the primary and secondary circuits until it is entirely dissipated in resistive and RF losses, when the current in the primary circuit is minimal and the spark gap opens.

Because of its unique double resonant operation, the ratio between the voltage applied to L_p and that developed on L_s is not dependent on the turns ratio between the primary and secondary coils like a conventional transformer, but is directly proportional to the square root of the ratio of L_s to L_p , which is usually less than the ratio of actual number of turns in most Tesla transformer. The general conditions required for a complete energy transfer from the primary to the secondary circuits is identified in [5.19], the conditions required to achieve the maximum voltage at the secondary circuit is pointed out in [5.20] and a full description of the Tesla transformer operation is given in [5.20]. Based on these, the coupling coefficient between the two coils ranges from 0.1 to 0.6 and is quite different from the values of 0.9 found in traditional iron-core transformers. Dual-resonant transformer technology is used [5.19], which is achieved when the coupling factor between the transformer primary and secondary coils is close to 0.6 and the two resonant frequencies are equal. At this level of coupling the transformer achieves its maximum output voltage within one cycle of the primary oscillation.

5.2 Design specification and main solutions

The performance of a Tesla transformer, defined as the maximum voltage developed at the output secondary terminal, is related to a number of factors including losses in components and connections, component value selection, operational environment conditions and the physical dimensions of the coils.

Figure 5.3 shows a magnetically-insulated HVT developed at Loughborough [5.21]. The arrangement is simple, with a single-turn primary winding, a helical secondary winding and a cylindrical central conductor that produces the circular magnetic field orthogonal to the axial and radial electric fields existing between the winding conductors. The operation of magnetic insulation will be explained in detail in Section 5.2.4.

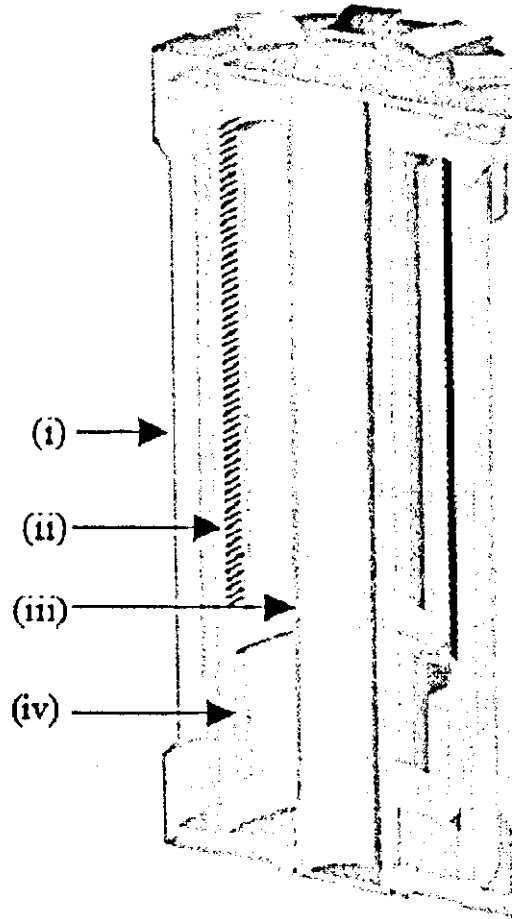


Figure 5.3 HVT components in vacuum showing (i) primary winding, (ii) high voltage secondary winding, (iii) central cylindrical conductor, (iv) HV electrode of capacitive divider [5.21]

5.2.1 Primary capacitor selection

The primary capacitance usually varies between $0.05 \mu F$ and $0.2 \mu F$, with the selection influencing both the primary resonant frequency and the maximum available pulsed power of the transformer. The energy oscillating in the circuits is a function of the primary capacitance and the voltage at the time of the spark-gap conduction, which is often known as the bang size. If the primary capacitor C_p is charged to a voltage V_0 , the energy discharged into the primary winding is

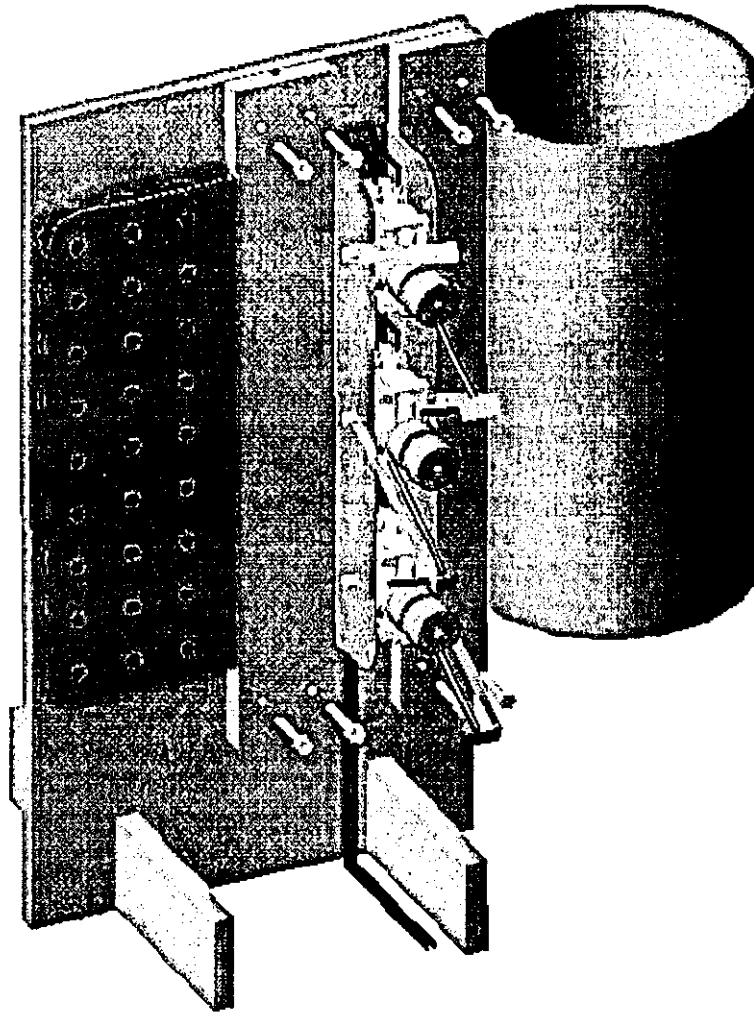


Figure 5.4 Primary circuit arrangement of 1 MV HVT

$$E_0 = \frac{1}{2} C_p V_0^2 \quad (\text{Eq.5.1})$$

By tuning with other parameters, and in accordance with practical experience, the primary capacitance was chosen as $0.12 \mu F$ and made up from forty five commercially available capacitors assembled in a series-parallel arrangement to achieve the voltage and capacitance requirements. Figure 5.4 shows this tubular capacitor assembly connected to the primary winding through three spark gaps arranged in parallel. There are two monolithic transmission lines, that include in their design the capacitor bank and the primary coil, each entirely encapsulated in a mylar-polyethylene laminate, which minimizes the number of connections and reduces the number of potential insulation fault points. The current probe consists of three magnetic pick-up coils in a single glass-tube package, which gives the ability to measure the current waveform as well as indicating the current density in the transmission line and providing assurance that all three switches operate.

5.2.2 Spark gap selection

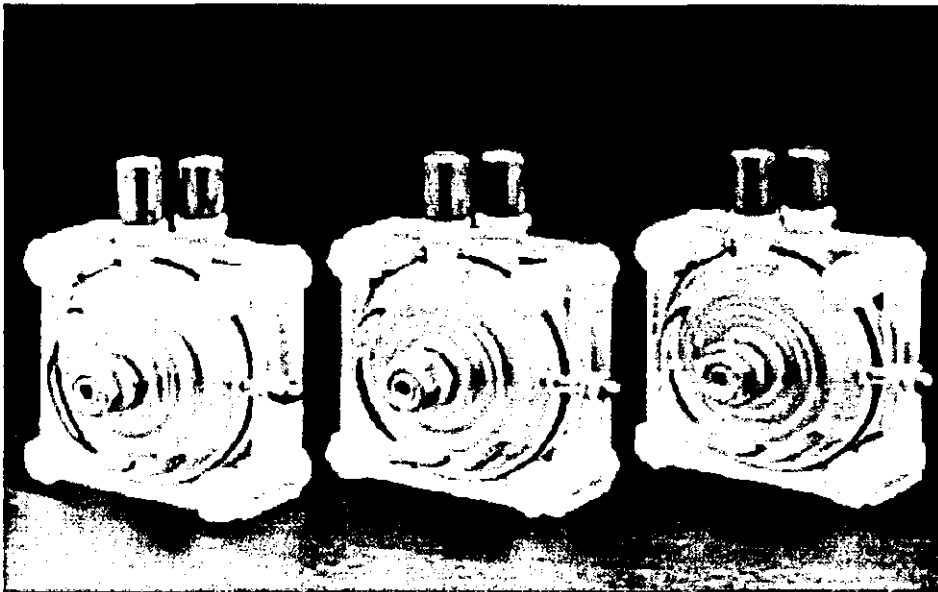


Figure 5.5 Titan T-670 Spark Gaps

The spark gap is basically a high power switch that is responsible for initiating the discharge of the capacitor into the primary winding of the Tesla coil. It turns-on when sufficient voltage exists across the spark gap and turns-off when the current flowing through it falls to a low level. It has to have a high voltage hold-off capability in the off-state, a high current carrying capability in the on-state and an extremely fast turn-on time, to be ideal for use in a Tesla transformer.

The simplest solution for the spark gap is a pair of electrodes separated by a dielectric that is usually a dry gas mixture including SF_6 , N_2 , etc. Commercial spark gaps also usually employ a trigger electrode to provide initial ionization of the dielectric and to facilitate breakdown between the two main electrodes. This provides control of the exact spark repetition rate, as required by radars, lasers, etc.

The major weakness of a non-triggered static spark gap is the variability of its threshold voltage and the consequent uncertainty in its operation. On the other hand, triggered spark gaps can control the exact spark repetition rate but are considerably more expensive and have a limited lifetime. Although Tesla transformers normally employ repetitive self breakdown spark gap switches, the requirements of the present project call for the use of triggered spark gap switches to allow controlled synchronization of the discharge.

The T-670 spark gap switches shown in Figure 5.5 and produced by Titan Corporation Pulse Sciences Division were chosen because their “pancake” configuration makes them well-suited to fairly high-energy applications requiring low inductance. These switches are designed for operation in the 20-100 kV range, and they can reliably handle a peak current of 100 kA and a charge transfer of 0.15 C . The use of three spark gap switches in parallel reduces the overall inductance of the main power source and in turn reduces the loss in the transformer.

5.2.3 Tesla coil dimensions and material selection

The physical dimensions of the Tesla transformer play an important role in its performance, as they determine the inductances of the primary and secondary coils, which are important parameters in determining the transformer output voltage. Selection of the physical dimensions for a Tesla transformer is a compromise between factors such as the inductances, resistive losses of the primary and secondary coils and the internal capacity of secondary coil.

The primary coil must be able to withstand the high peak currents in the primary circuit when the spark gap fires and it should be constructed from a good electrical conductor with a low resistivity and a considerable cross-sectional area. Thus a single-turn copper coil is the ideal choice and is relatively easy to manufacture.

For a Tesla transformer to operate correctly the primary and secondary circuits need to be tuned to the same resonant frequency, which is achieved by making one component of either the primary or the secondary circuit adjustable. The coupling coefficient also need to be adjusted to about 0.6 in order to achieve the maximum voltage at the secondary circuit [5.21]. The design of the high-voltage secondary winding requires a minimum separation between the individual turns and between the primary and secondary windings to avoid dielectric breakdown. The secondary winding is located in a vacuum chamber that is evacuated to a pressure of 10^{-5} Torr , thereby simplifying enormously the insulation problems between the primary and secondary windings. All these requirements translate into a minimum number of turns for the windings to achieve compact geometry and simplicity of construction.

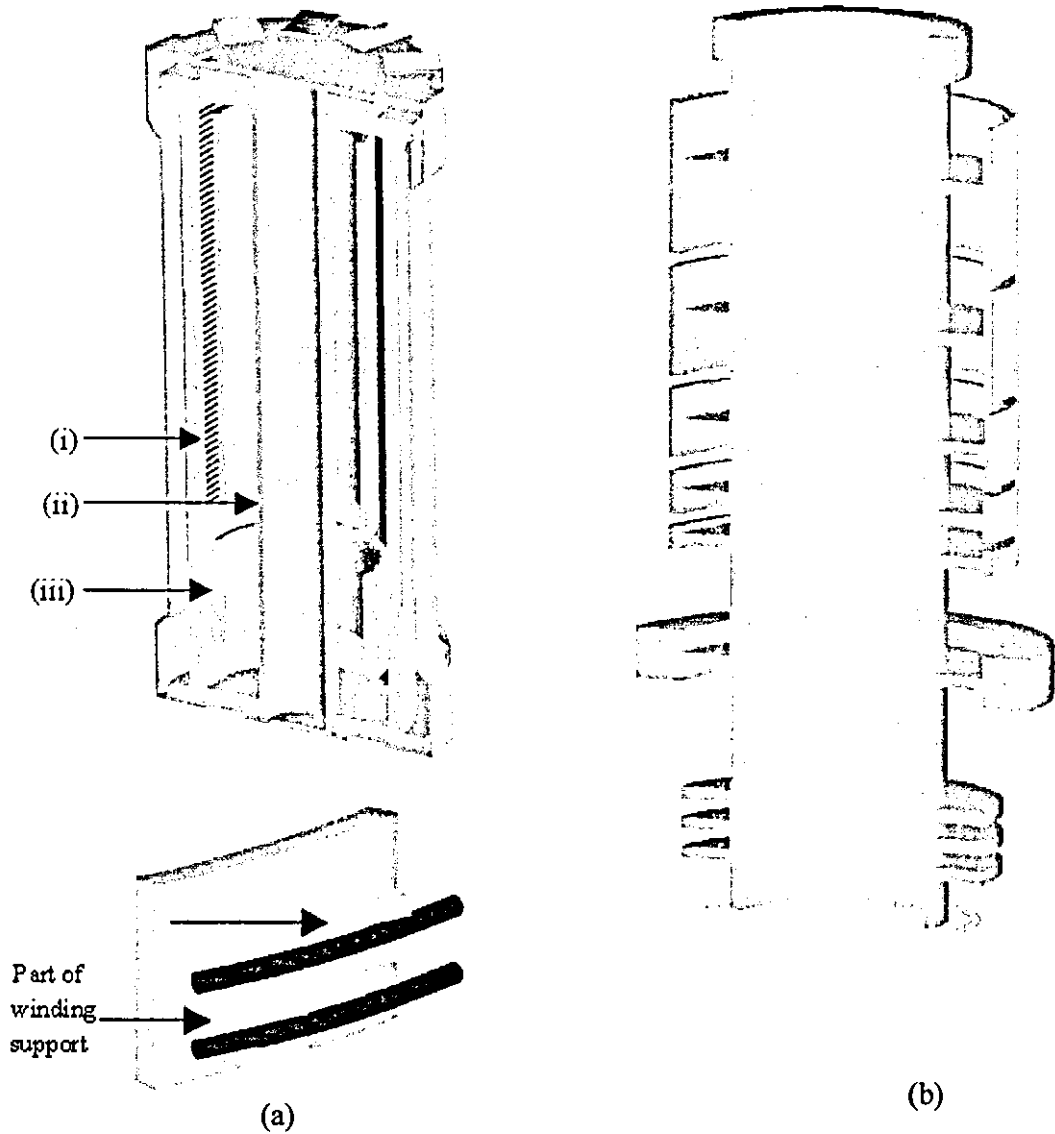


Figure 5.6 Secondary winding arrangement of Tesla transformer

(a) secondary winding using 2 mm uninsulated stainless steel wire with PVC spacers between the turns (b) secondary winding with polyethylene insulated copper wire.

In order to obtain the optimal transformer layout, different transformer secondary coil geometries and conductor types were studied. An early winding was made of 2 mm uninsulated stainless steel conductor wound around a PVC mandrel with a constant pitch, with the pitch maintained by the polythene spacers shown in Figure 5.6 (a). Both inter-turn insulation and the prevention of flashover across the

surfaces are maintained mainly by the magnetic insulation when the voltage exceeds 500 kV. A later design was constructed from 3 mm polyethylene insulated cable with a 0.9 mm copper conductor, which allows the secondary winding to be shorter and much more compact as shown in Figure 5.6 (b). Both type of secondary winding were tested using the single-turn primary winding described in Chapter 6.

5.2.4 External field system design

As stated in Section 3.4, turn-to-turn breakdown arising from fast-rising voltage transients is common with helical HVTs. Unlike the transformer described in Chapter 4, the electric field of a spiral-strip secondary winding is radial and the major axial component of the magnetic field from the single-turn primary is extremely favourable to the adoption of magnetic insulation. The electric field of the helical winding is axial and the maximum electric stress occurs mainly in the central region, while the radial component of the magnetic field strength produced by a helical coil or single-turn primary (which is the component that in magnetic insulation can be used to divert the electrons) is small, especially so at the centre. The successful use of helical magnetic self insulation transformer was reported in a small-scale prototype [5.22], but the additional magnetic field is essential for operation in the megavolt range.

An auxiliary conductor positioned inside the secondary coil was introduced to achieve magnetic insulation as shown in Figure 5.7. A high current flows through this, producing a circular magnetic field B perpendicular to the major axial electric field already existing. The magnetic field is given by [5.23] as:

$$B = \frac{\mu_0 I}{2\pi r} \quad (\text{Eq.5.2})$$

The current is kept constant to prevent any changes in the magnetic flux influencing the transformer performance. In order to reduce the inductance of the auxiliary coil, a number of strips outside the secondary coil are used as return conductors.

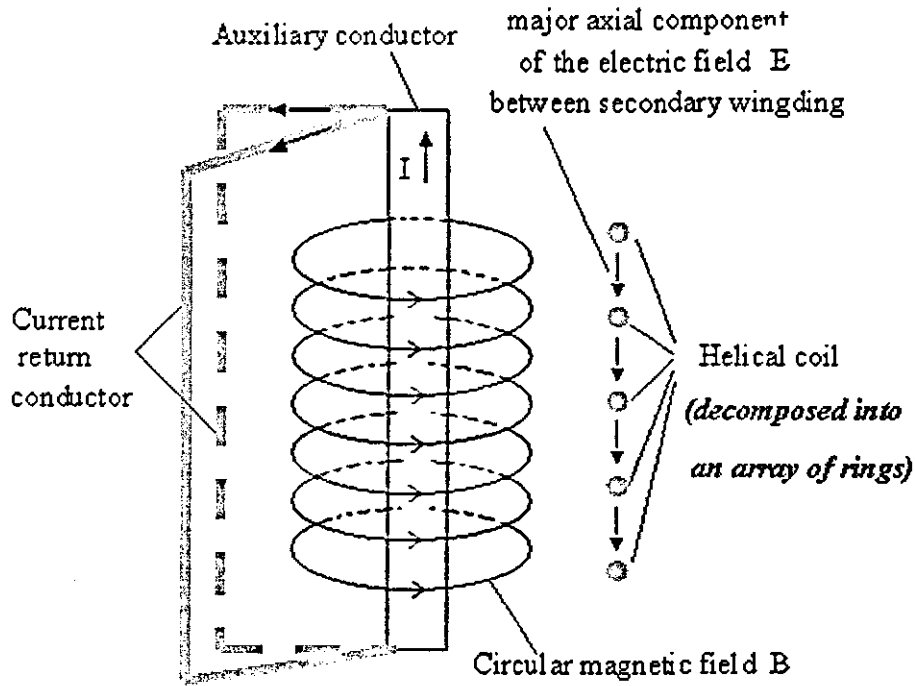


Figure 5.7 Mechanism of magnetic insulation with auxiliary coil

5.3 Simulation model

Filamentary modelling [5.24] was used to optimize the transformer design and to predict the transformer performance. The inductance and capacitance were calculated and used in a complete model of the Tesla transformer through which the parameters of the resonant circuits and the Tesla transformer were tuned to develop the maximum secondary voltage with compact geometry. The validity of the overall model is assessed in Chapter 6, by comparing measured and simulated results.

5.3.1 Theory of operation

Figure 5.8 illustrates the principle of magnetic insulation in the Tesla transformer. According to first Kirchhoff's first law, the sum of the voltages around a closed circuit is zero, therefore the corresponding set of first-order differential equations are obtained as:

$$V_0 - \frac{Q_p}{C_p} = (R_p + R_b)I_p + (L_p + L_b)\frac{dI_p}{dt} - M\frac{dI_s}{dt} \quad (\text{Eq.5.4})$$

$$0 = R_s I_s + L_s \frac{dI_s}{dt} - M \frac{dI_p}{dt} \quad (\text{Eq.5.5})$$

where Equation 5.4 is for the primary circuit and Equation 5.5 is for the secondary circuit. The external magnetic field is provided by an additional source, which contains the capacitor C_{ext} connected directly to the auxiliary coil L_{ext} (R_{ext} represents the equivalent resistance) through the switch S_{ext} . Firstly the auxiliary bank is charged, and after the switch S_{ext} is closed, the capacitor C_{ext} discharge with the governing equation being

$$V_{ext0} - \frac{Q_{ext}}{C_{ext}} = R_{ext} I_{ext} + L_{ext} \frac{dI_{ext}}{dt} \quad (\text{Eq.5.3})$$

When the current I_{ext} from the auxiliary bank approaches a maximum and $\frac{dI_{ext}}{dt}$ is almost zero, the main capacitor bank controlled by spark gap S_p starts to discharge into the transformer primary winding. The operating period of the auxiliary bank is longer than that of the main capacitor bank, say by about 80 times, which means that during the whole period of main capacitor bank operation $\frac{dI_{ext}}{dt}$ from the auxiliary bank may be regarded as zero, which ensures that the auxiliary coil has almost no coupling effect with either the primary and secondary windings.

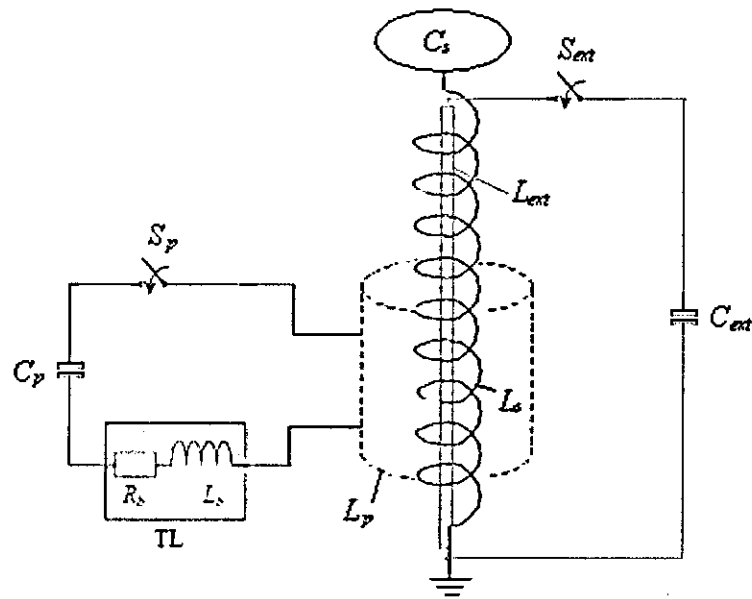


Figure 5.8 Principle of magnetic insulation in Tesla transformer

5.3.2 Parameter calculation

Calculation of the self-inductances of the primary and secondary windings and also the mutual inductance between them is described in Section 2.5.2 and the filamentary representation of the helical HVT is shown in Figure 2.8 with a detailed explanation given in Section 2.10.3. The capacitance calculation is given in Section 2.8 and the resistance calculation in Section 2.4.5. The results of these calculation compare well with experimental data, so that they provide a good basis for both performance prediction and system optimization.

5.3.3 Optimized system

The rules for selecting the major components of a Tesla transformer were summarized in Section 5.2. The general design of the transformer is influenced by the power supply choice, and the commercially available capacitors used enable the power supply to be readily scalable as more modules can be added in series to reach a higher charging voltage. The present transformer design is subject to the following constraints:

- Resonant frequency matching
- Coupling factor between the primary and secondary coils close to 0.6
- Maximum voltage of about 1.5 MV
- Primary current limited by the capacitor and spark gaps

The first design used one spark gap with a capacitor of $0.22 \mu F$ charged to 30 kV, with the overall capacitor bank inductance of 75 nH and resistance 130 m Ω including the contribution from spark gap. The primary inductance is 140 nH (single-turn winding of 1.2 mm copper sheet with a length of 600 mm and outside diameter of 320 mm). The secondary inductance is 412 μH (80-turn, 240 mm diameter, 800 mm long helical winding of 3 mm stainless steel conductor with constant pitch of 7 mm) and the mutual inductance is 5 μH . The inductance and resistance results are from Section 5.3.2. with the equations in Sections 2.5.2 and 2.4.5. Predicted wave forms of the primary current and voltage output are shown in Figure 5.9. The maximum output voltage pulse from Figure 5.9 (b) is about 1.3 MV as expected, but Figure 5.9 (a) shows that the maximum primary current is about 25 kA, just on the limit that the capacitor bank can withstand.

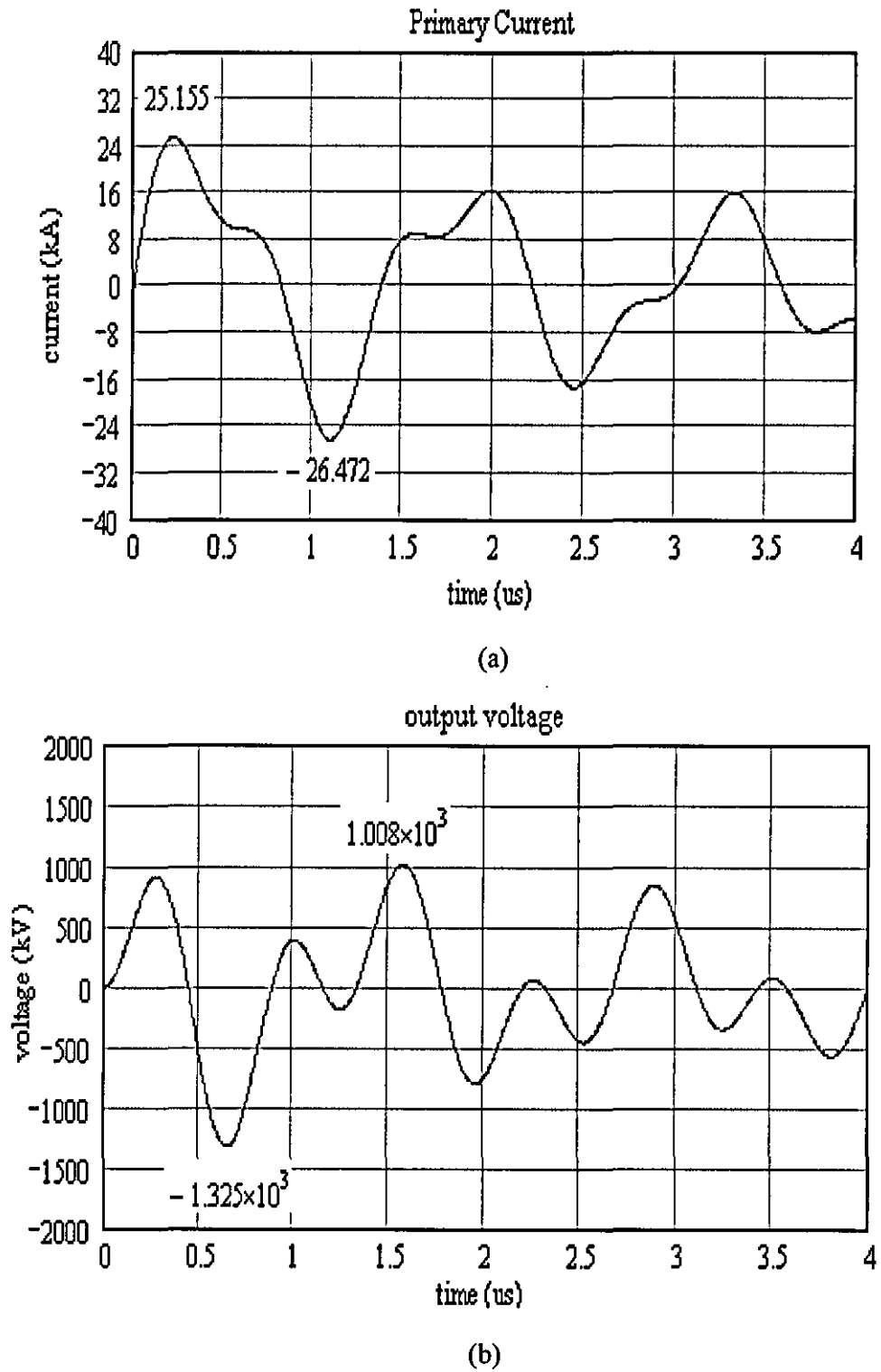
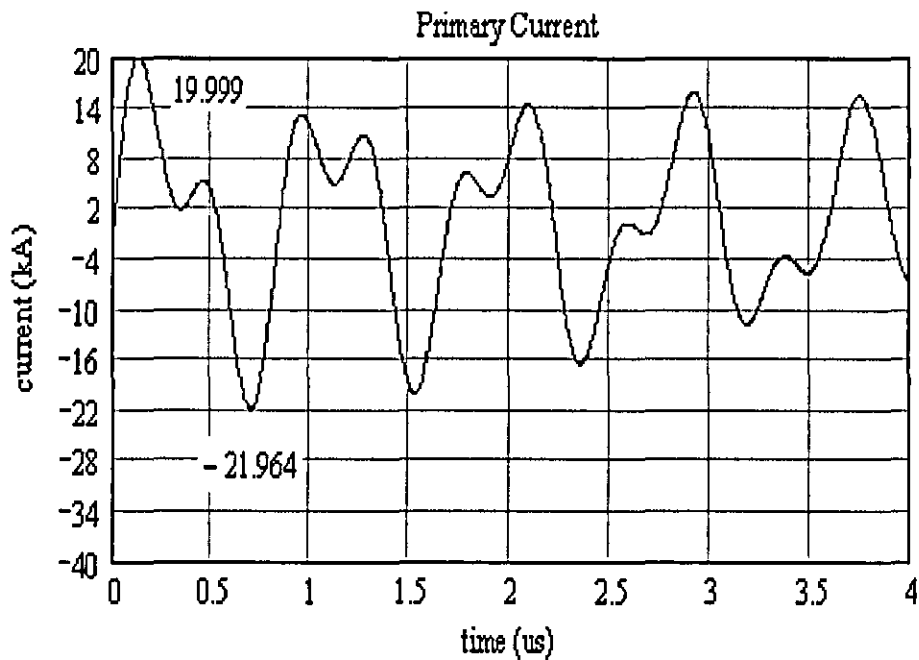


Figure 5.9 Predicted values of first design (a) primary current (b) open secondary voltage

The second design used three spark gaps with the capacitor $0.09 \mu F$ charged to $30 kV$, with overall capacitor bank inductance of $40 nH$ and resistance $60 m\Omega$ includes the contribution from the spark gaps. The primary inductance is $138 nH$ (single-turn winding of $1.2 mm$ copper sheet with a length of $600 mm$ and an outside diameter of $316 mm$). The secondary inductance is $259 \mu H$ (50-turn, $250 mm$ diameter, $500 mm$ long helical winding of $3 mm$ stainless steel conductor with constant pitch of $7 mm$) and the mutual inductance is $4 \mu H$. The inductance and resistance results are from Section 5.3.2. and the corresponding predicted primary current and voltage output are shown in Figure 5.10. The maximum output voltage pulse from Figure 5.10 (b) is about $1.3 MV$ and the maximum primary current from Figure 5.10 (b) is reduced to about $20 kA$ which satisfies the withstand rating condition of both the capacitor bank and the spark gaps. However this design requires a very small secondary capacitance as about $30 pF$, which may be exceeded by secondary winding.



(a)

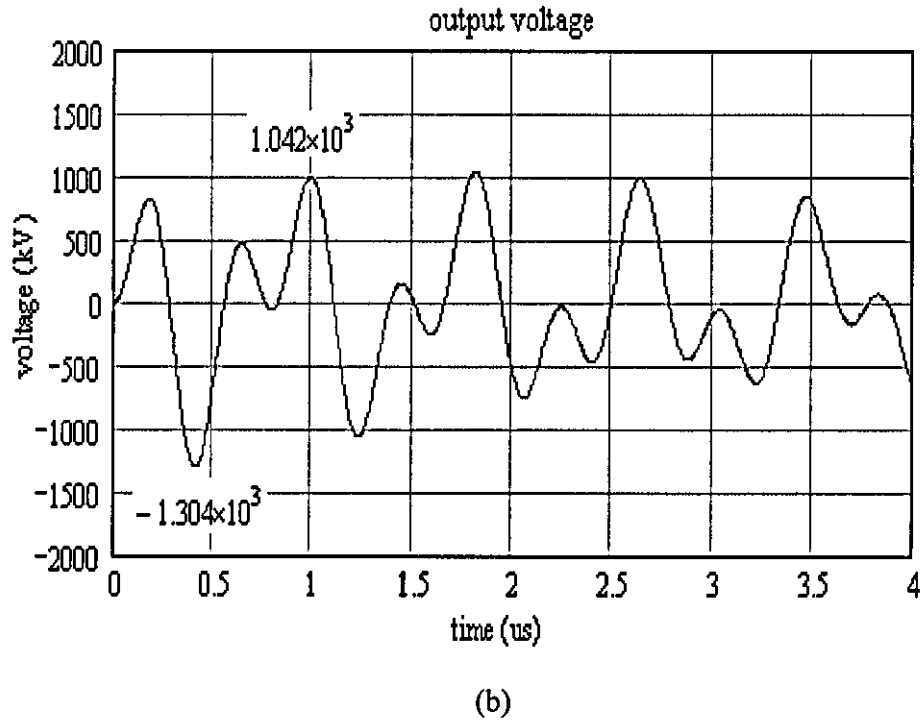


Figure 5.10 Predicted values of second design (a) primary current (b) open secondary voltage

A third design was produced by optimisation of the second design [5.20]. In the discharge circuit of Figure 5.8, the capacitor C_p is $0.12 \mu F$ and the overall inductance from the capacitor bank of $30 nH$ includes the contribution from spark gaps. The primary inductance is $140 nH$ (single-turn winding of $1.2 mm$ copper sheet with a length of $600 mm$ and outside diameter of $320 mm$). The secondary inductance is $240 \mu H$ (55-turn, $270 mm$ diameter, $550 mm$ long helical winding of $3 mm$ stainless steel conductor with constant pitch of $10 mm$) and the mutual inductance is $4.2 \mu H$. The primary current and voltage output can be obtained as shown in Figure 5.11 and the maximum output voltage pulse is about $1.4 MV$ with the maximum primary current being about $20 kA$.

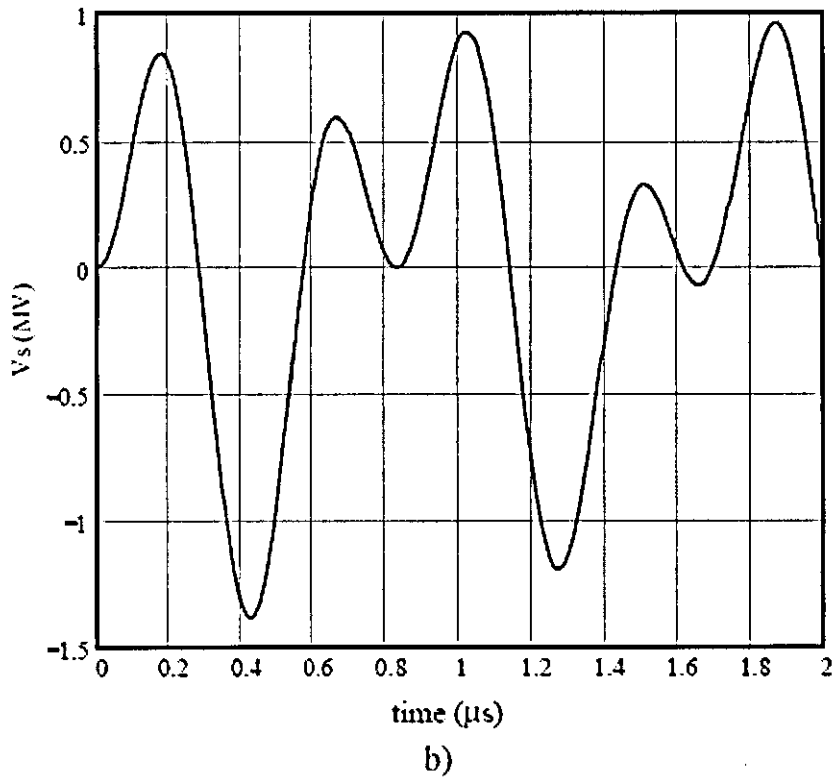
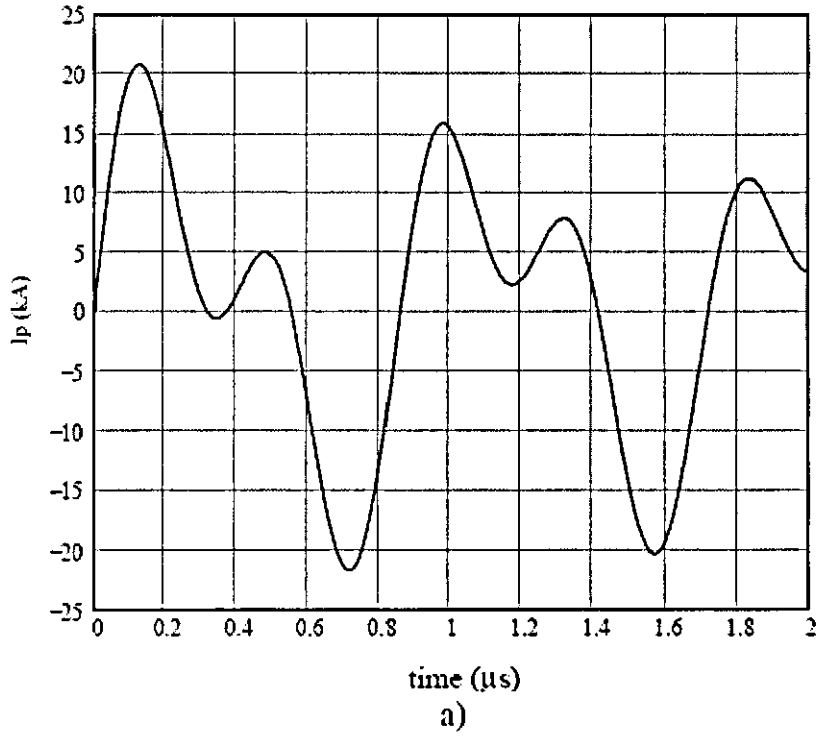


Figure 5.11 Predicted values of third design (a) primary current (b) open secondary voltage

The auxiliary coil was designed to achieve maximum magnetic field with an existing capacitor bank of $200\ \mu F$ and a low internal inductance of $20\ nH$, charged to $25\ kV$. An exploding wire array was used as opening switch to protect the auxiliary bank from high-current reversal oscillations, which introduced a inductance of $20\ nH$. The conductor contains a $900\ mm$ long, $106\ mm$ diameter aluminum tube with a number of aluminum strips carrying the return current positioned outside the secondary winding acting as coaxial return conductors to minimize the inductance. The calculated inductance is about $280\ nH$, including the return conductors. A maximum current of $0.6\ MA$ can be obtained as shown in Figure 5.12 and the calculated magnetic flux density of about $1\ T$ from Equation 5.2 is produced by the auxiliary bank through the central cylindrical conductor.

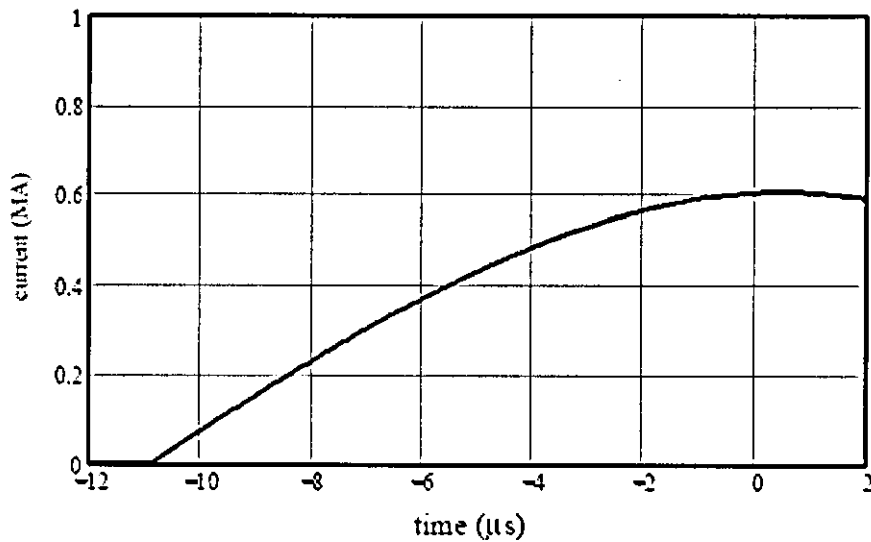


Figure 5.12 Predicted current provided by an external source and required for the magnetic insulation (time origin as Figure 5.1)

6 Testing

A range of experiments was carried out on the transformers with magnetic insulation described in Chapter 4 and 5. The experimental results are generally in good agreement with data predicted from numerical modelling and have provided theoretical justification of the magnetic insulating properties. Magnetic self-insulation has been demonstrated up to 500 *kV* and up to 1 *MV* with an injected magnetic field, both of which open the way for even more advanced higher voltages transformers.

6.1 Self-Magnetic insulation of 500 kV HVT [6.1]

To study the magnetic insulation effect, a vacuum spiral-strip transformer as stated in Chapter 4 was constructed, with insulation provided by the magnetic field produced by the primary winding current. The effect of magnetic insulation was investigated by keeping the same dI_p/dt , while feeding the primary winding with current pulses I_p of different amplitudes.

6.1.1 Experimental set up

The experiment construction and arrangement described in Chapter 4 was again used for testing the self-magnetically insulated transformer of Figure 6.1. The single-turn primary is constructed from high-conductivity 1.2 *mm* copper sheet, with an effective primary winding width of 100 *mm* and an internal

diameter of 320 mm. A glass bell jar, positioned inside the single-turn primary winding and evacuated to a pressure of 10^{-5} to 10^{-6} Torr by a vacuum pump, houses the 8-turn stainless steel secondary winding of Figure 6.2, which is also 100 mm wide and 1.2 mm thick. The mean diameter of the first (outermost) turn is 290 mm and that of the final (innermost) turn is 176 mm. To ensure that an approximately constant field exists between turns, the distance between them varies with radius from 11 mm for the outermost turns to 4 mm for the innermost turns.

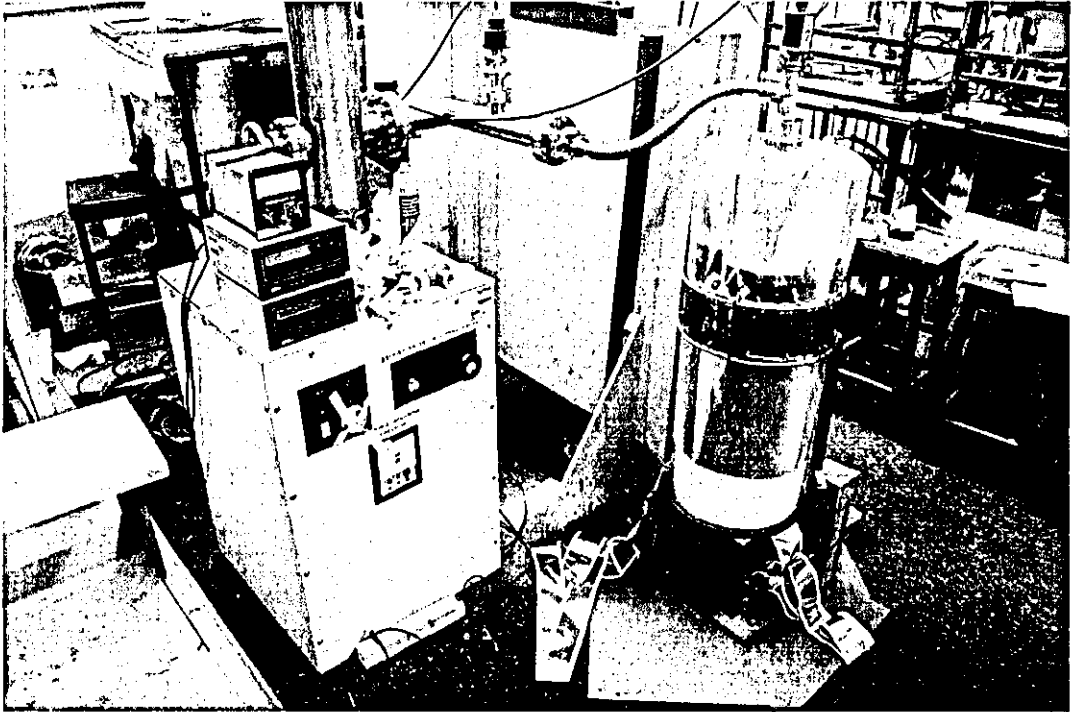
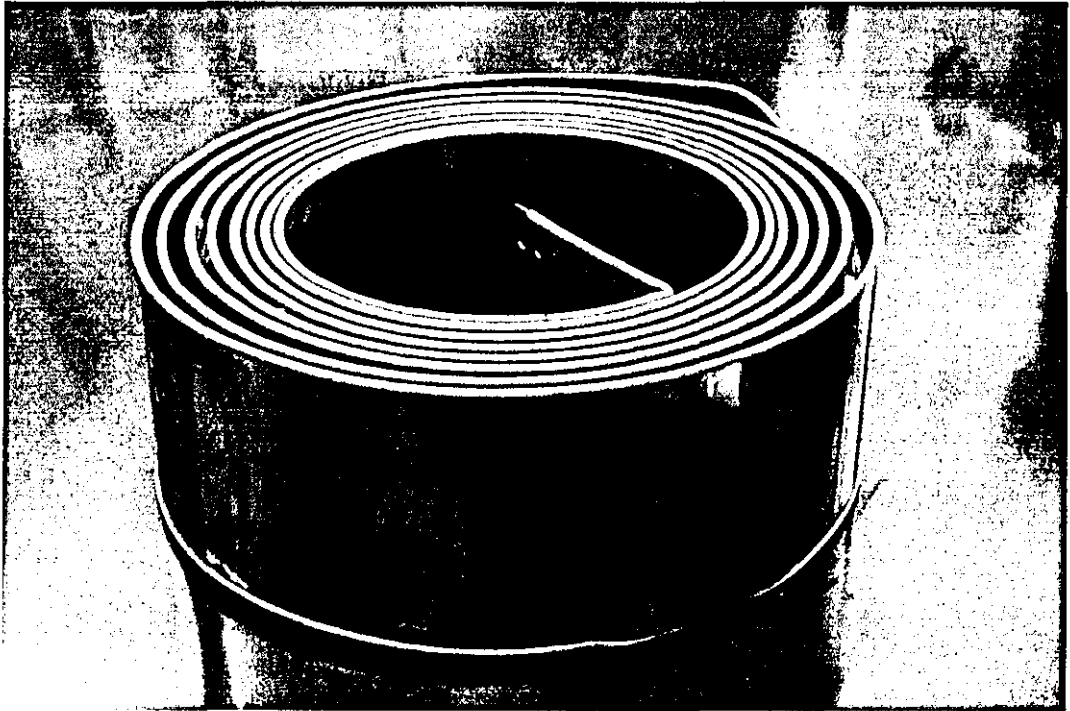
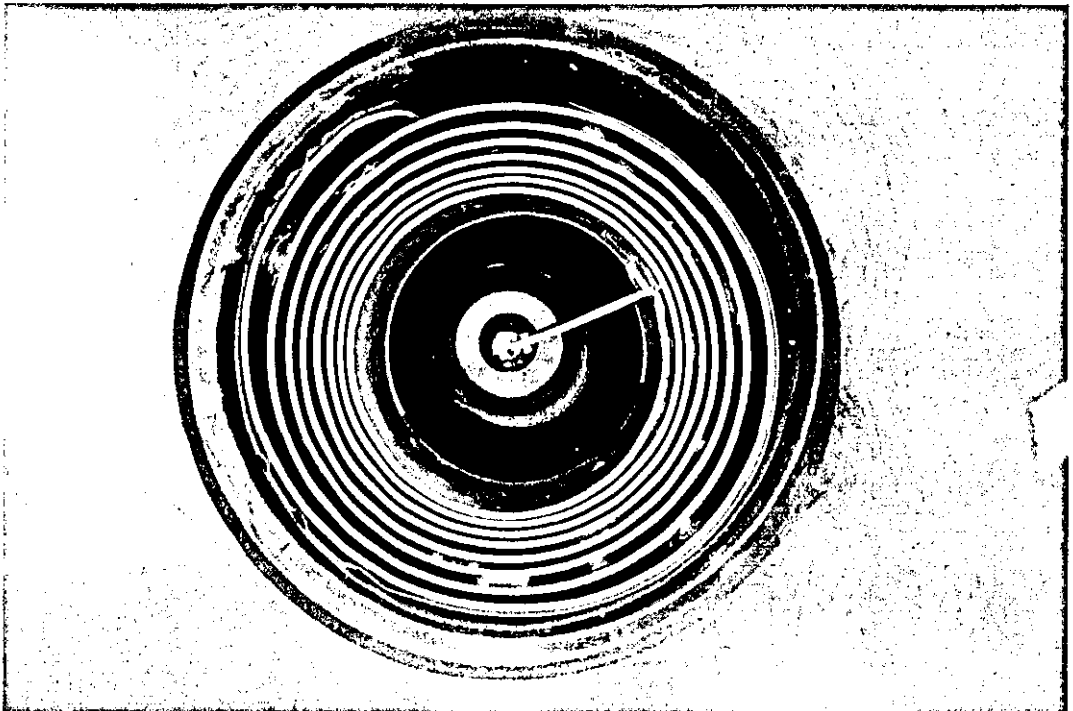


Figure 6.1 Experimental 500 kV transformer with self-magnetic insulation



(a)



(b)

Figure 6.2 Secondary spiral winding of transformer

(a) side view (b) front view

Supporting spacers, consisting of two MACOR[®] cylinders with an intervening glass sheet mounted between turns, assist in maintaining the spiral integrity. All components are bonded together and attached to the stainless steel turns by high vacuum epoxy resin. Figure 6.3 presents a schematic of a spacer and a photograph of a real component. Two split rings (shown in Figure 6.4) are placed near the edge of the primary winding to form a ring cage shield [6.2] which, as described in Section 3.3.3.3, will substantially reduce the field enhancement.

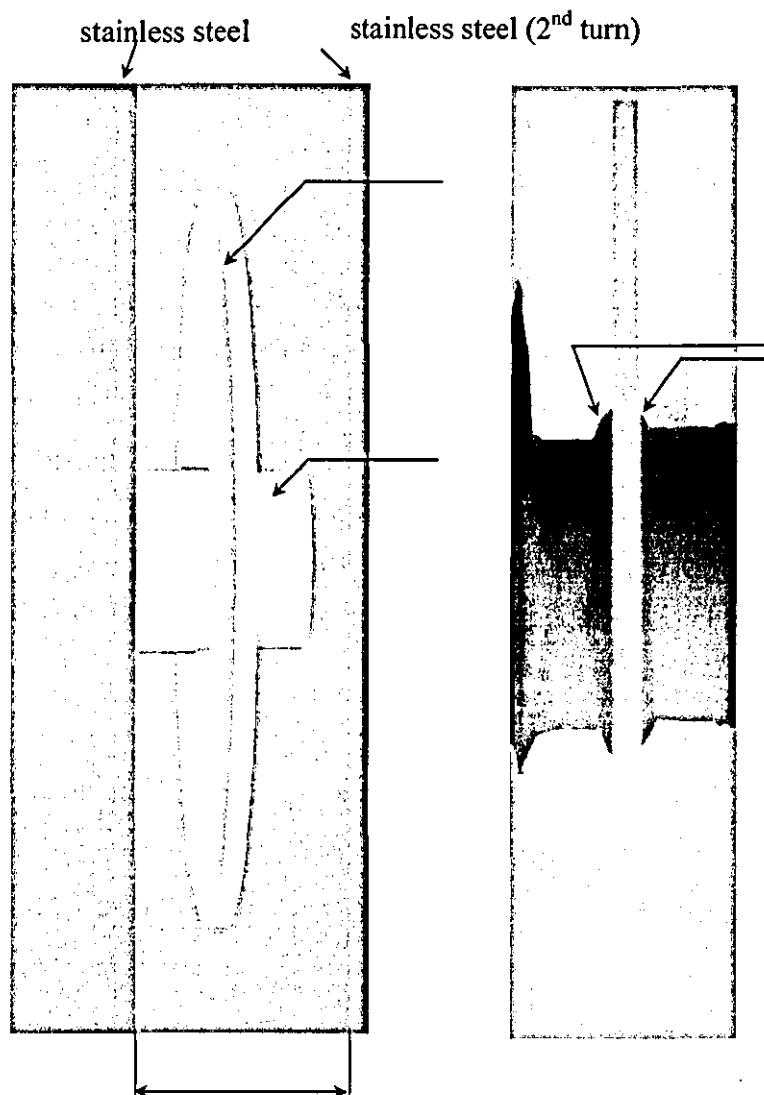


Figure 6.3 Schematic (dimensions in mm) and photograph of a glass/Macor[®] spacer installed in the secondary winding

A magnetic pick-up probe located in a tunnel in the transmission line and calibrated *in situ* measures the dI_p/dt , with the result being numerically integrated to provide the current I_p . A built in high-voltage capacitive divider (HVD) calibrated using a commercial 1 MV capacitive probe [6.3] enables the secondary voltage to be recorded. Optical fibres collect light from the EWA explosion, and provide triggering signals for battery powered 500 MHz digital oscilloscopes through opto-electronic couplers to ensure electromagnetically noise-free signals.

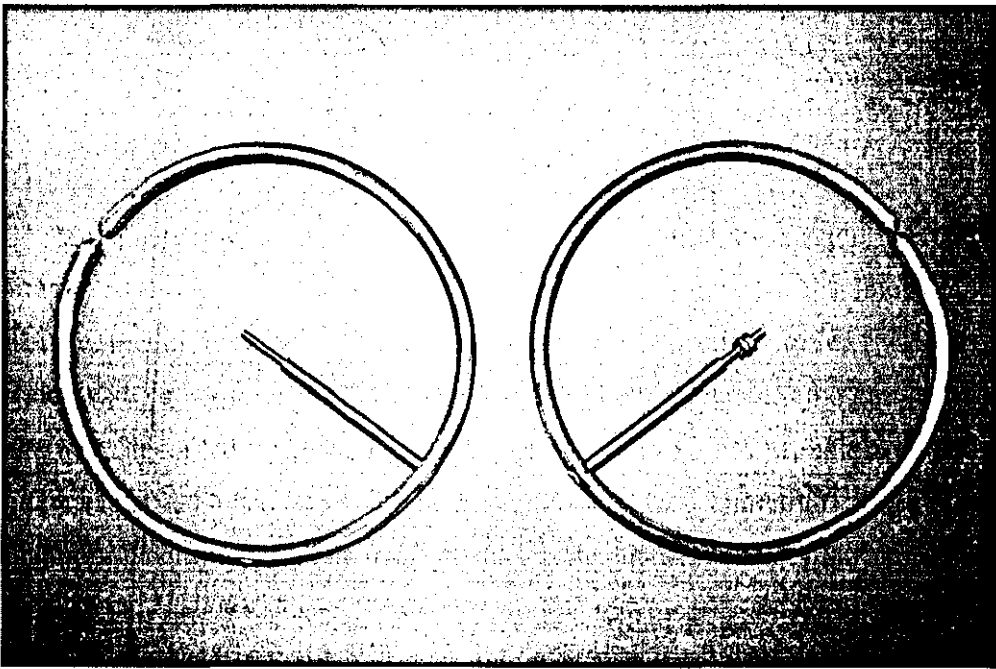


Figure 6.4 Ring cage shield

Figure 6.5 shows the experimental arrangement, in which the transformer primary circuit is powered through a parallel-plate transmission line (TL) from a 52.5 μF 25 kV capacitor (C). An exploding wire array (EWA) acts as a pulse conditioning circuit element, and is constructed from a number of 250 μm OFHC copper wires in parallel. To investigate the performance of the magnetic insulation, the capacitor charging voltage V_0 can be varied from 0 to 25 kV, the number of exploding wires from 2 to 11 and their length from 135 to 250 mm, which

together enable the HVT primary winding to be fed with a range of current pulses I_p of different amplitudes but approximately the same dI_p/dt . This allows the conditions for magnetic insulation to be investigated, since the secondary voltage is given by $V_s = -M(dI_p/dt)$ and I_p is responsible for the insulating field.

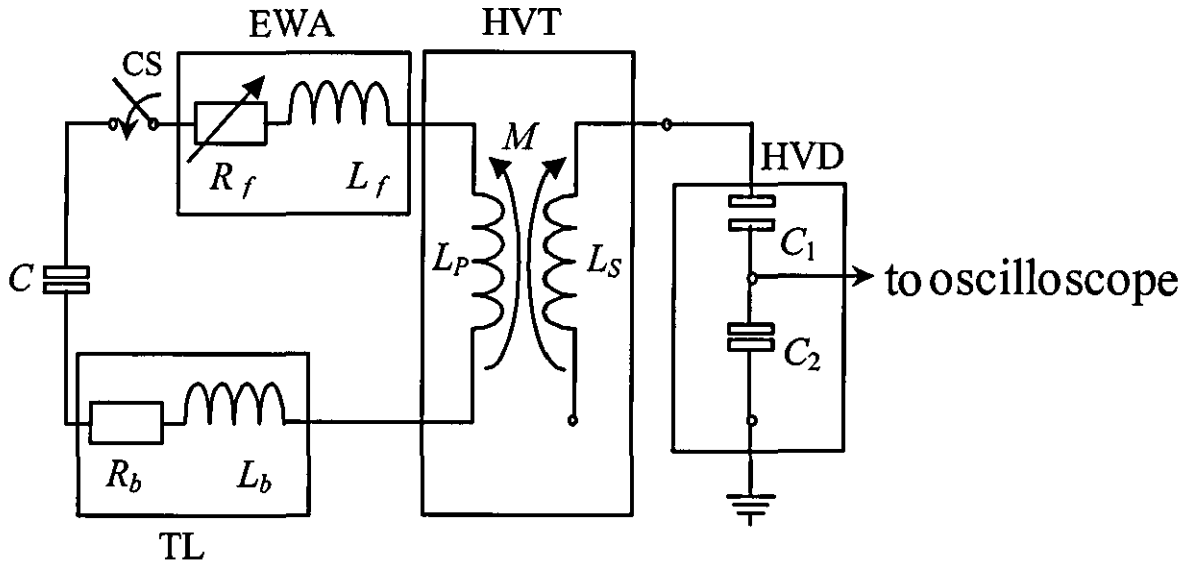


Figure 6.5 Circuit for MSI-HVT experiments

R_f , L_f and R_b , L_b are the resistance and inductance of the EWA and TL. C_1 and C_2 are the high voltage and low voltage capacitors of the HVD. Other components are explained in the text.

The EWA assembly that acted as an opening switch was introduced into the transmission line of the discharge circuit, and consisted of two copper electrical retaining plates with rows of electrical retaining points on which to lay the exploding wires horizontal. The length of the wires can be controlled by adjusting the distance between the retaining plates and the selected number of wires was soldered onto the retaining points. Insulation between the plane of the wires and the copper strip forming the current return path is provided by a polyethylene plate. The opening switch was inevitably damaged during an experiment and had to be substantially remade for each experiment.

After each 10 experiments the bell jar was opened and the transformer secondary winding scrutinized. It was found that most breakdowns happening during experiment action originated from the winding edges, particularly in the vicinity of the grounded outermost turn as predicted in Section 4.4.1.2.

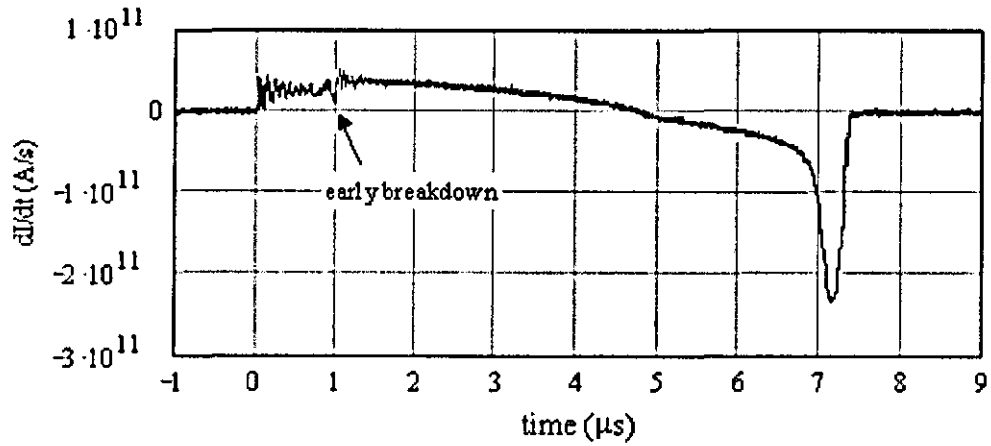
6.1.2 Analysis of results

6.1.2.1 Preliminary experimentation

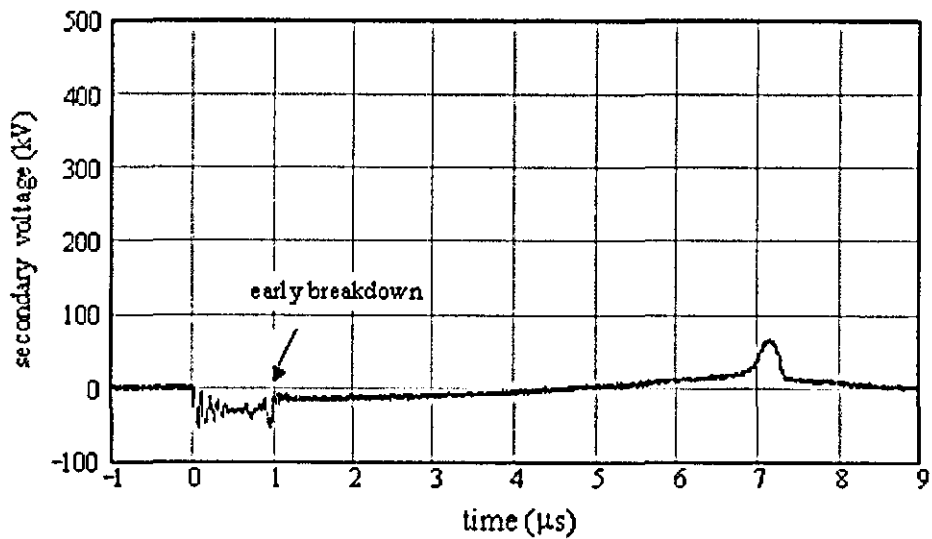
Using the simplified approach of Section 4.4.1, the characteristic vacuum breakdown voltage V_{break} of the HVT without magnetic insulation was estimated as 350 kV. Initial experiments at $V_0 = 15$ kV however experienced an early breakdown, about 1 μs after the beginning of the capacitor discharge. This was unexpected, as the secondary voltage at the time (about 40 kV) was very much less than V_{break} , and the exact cause of the breakdown remains unknown.

One possible solution, given in Section 4.4.2, is to introduce an externally produced magnetic field at the initiation of the experiment, but it would be complex to construct another field producing system. The eventual solution adopted was to decrease the high electric stress at the critical points (edges) by attaching field grading rings [6.2] to both transformer windings, as explained in Section 3.3.3.3. This was straightforward for the primary winding (see Figure 6.4), but a round copper structure such as a slotted cylinder was difficult to install at the edges of the secondary winding. A practical alternative was found in the use of conductive O-strips (CHOMERICS® [6.4]) having a diameter of 3.2 mm and formed from silicone elastomer binder with a conductive filler of Ag and Cu, resulting in a volume resistivity of $\rho = 4 \times 10^{-5} \Omega\text{m}$. The low degassing properties of the O-strip material ensured that it performed well under vacuum conditions. Figure 6.7 shows the slotted O-strips in position on the secondary winding, and numerical analysis indicated that the grading on both windings resulted in about a 30% reduction in the peak electrical field.

With this technique implemented, early breakdown only occurred when the capacitor charging voltage was above 19 kV, which was adequate to allow the conditions necessary for magnetic insulation to be investigated.



(a)



(b)

Figure 6.6 (a) dI_p/dt and (b) V_s measured in an experiment with early breakdown (1 μ s after closure of CS of Figure 6.5) The initial charging voltage of the capacitor bank was 15 kV

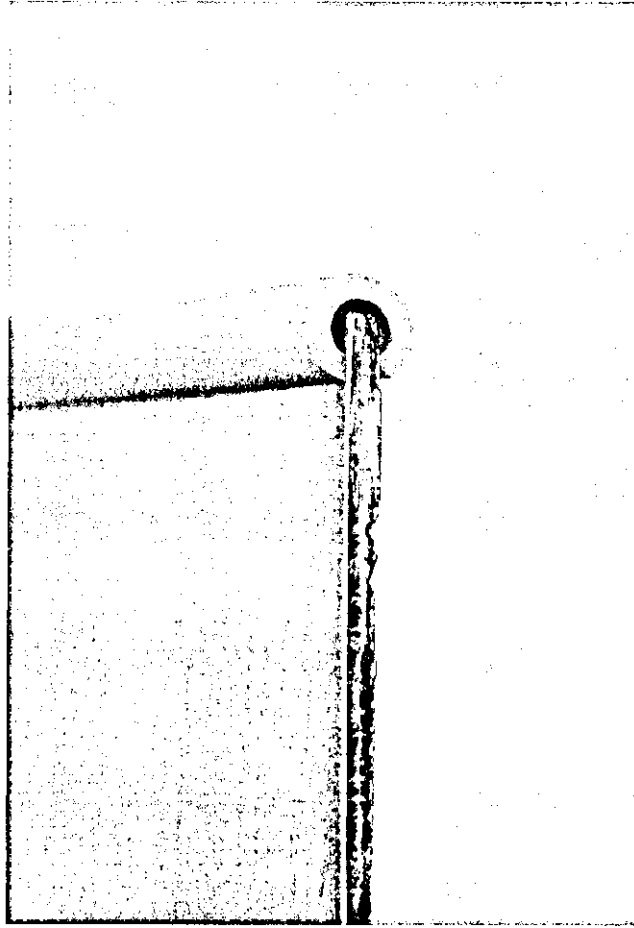


Figure 6.7 Slotted conductive O-strip placed onto the edge of secondary winding

6.1.2.2 EWA performance

Before the main magnetic insulation experiments, a series of calibration experiments were performed. The equivalent circuit of Figure 6.8 presents the calibration circuit for the EWA, in which a $210 \mu F$ capacitor bank was charged initially to about $20 kV$. The inductance L_b is $32 nH$ and the resistance R_b is $1 m\Omega$, which include contributions from both the capacitor bank and the transmission line. An I-dot probe was located in the copper conductors of the transmission lines.

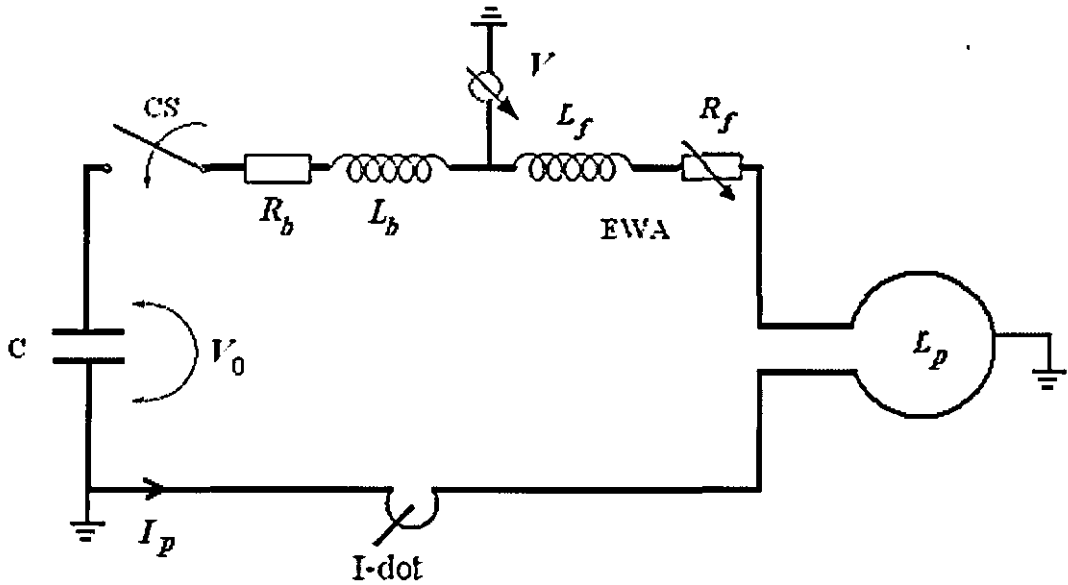


Figure 6.8 Calibration circuit for EWA

The characteristics of Figures 6.9, 6.10 and 6.12 show the series circuit discharge current, the time rate-of-change of this current and the voltage developed across the EWA, with the solid and dotted traces in each figure representing respectively the simulation results from Section 4.2 and results from experiments. Figure 6.9 shows a steady rise of discharge current to a peak of 361 kA after a time of 7.7 μs followed by a rapid decay. The current does not fall to zero after the wires explode, possibly due to a breakdown occurring in the EWA. Figure 6.10 shows that the time rate-of-change of current attains a peak value of 4×10^{11} A/s after a time of 9.5 μs and, importantly, the characteristic attains high values for relative large values of the discharge current. Figure 6.11 shows details of the rate-of-change of current between 9 μs and 10 μs , with a breakdown of the EWA presumably happening at 9.6 μs , according to this diagram. Figure 6.12 shows that the potential difference across the EWA reaches a value of 138.49 kV at 9.5 μs . This establishes that high level of voltage are developed in the circuit, and that a high voltage pulsar has been achieved.

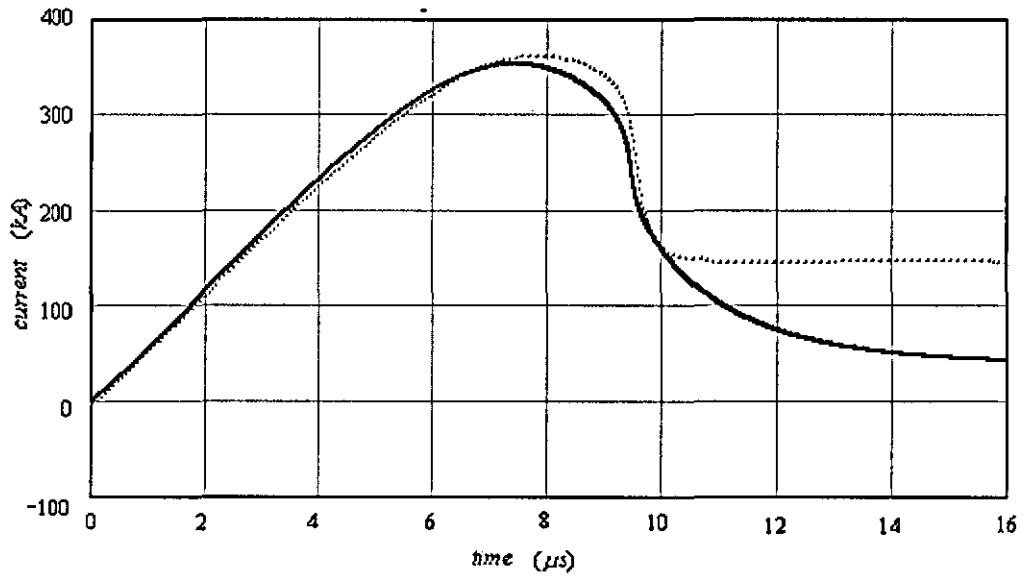


Figure 6.9 Circuit current

(solid -simulation result ; dotted -experiment result)

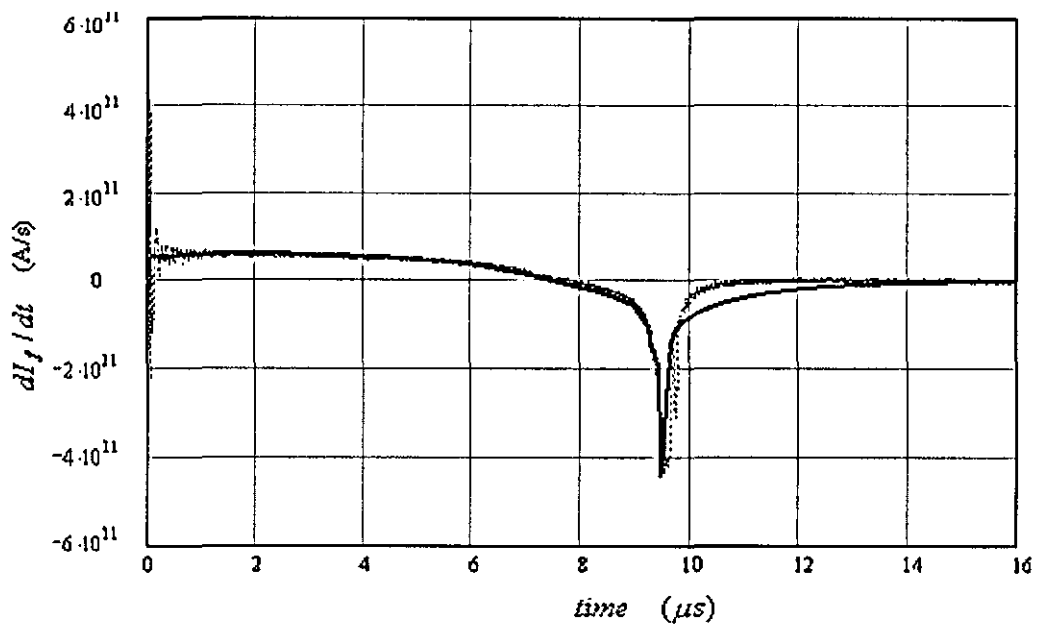


Figure 6.10 Rate-of-change of current

(solid -simulation result ; dotted -experiment result)

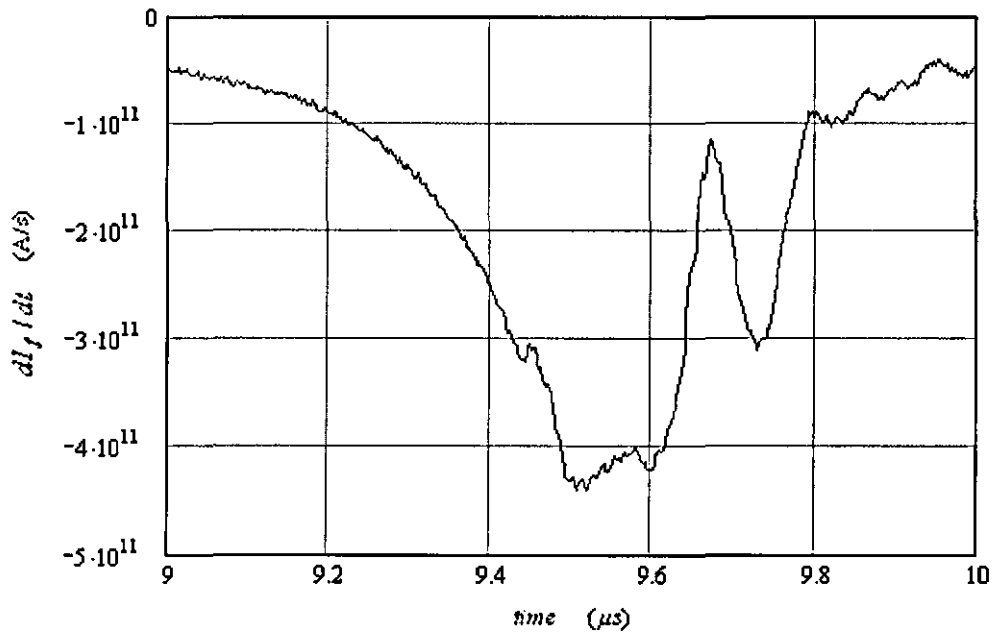


Figure 6.11 Details of rate-of-change of current between (9 μ s - 10 μ s)

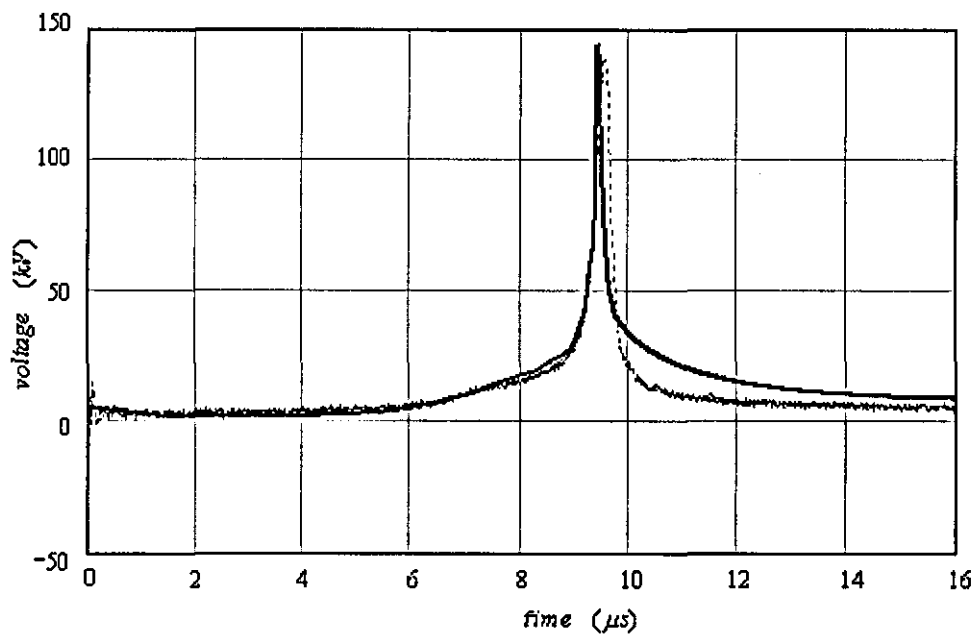


Figure 6.12 Voltage across EWA

(solid -simulation result ; dotted -experiment result)

The dependence of the resistivity of the EWA on the input energy W for the exploding wires was determined. Due to the insufficient number of points collected from the oscilloscopes, it was somewhat difficult to obtain the direct dependence of $R(W)$ from the measurements. Therefore, the result from [6.5] was used and refitted to match the calculation results with the measurements. The $R(W)$ variation obtained is shown in Figure 4.5, which was then incorporated into the mathematical model of the pulsar in Section 4.2.

6.1.2.3 Inductance

The primary inductance of the transformer can be obtained by measuring the voltage across the primary winding together with the rate of change of current in the winding, by using the circuit shown in Figure 6.13 and the formula:

$$L_p = \frac{V_p}{\frac{dI_p}{dt}} \quad (\text{Eq.6.1})$$

Also the mutual inductance can be found from:

$$M = \frac{V_s}{\frac{dI_p}{dt}} \quad (\text{Eq.6.2})$$

where V_s is the measured open circuit voltage of the secondary winding and $\frac{dI_p}{dt}$ is the rate of change of current in the primary winding using the circuit shown in Figure 6.14.

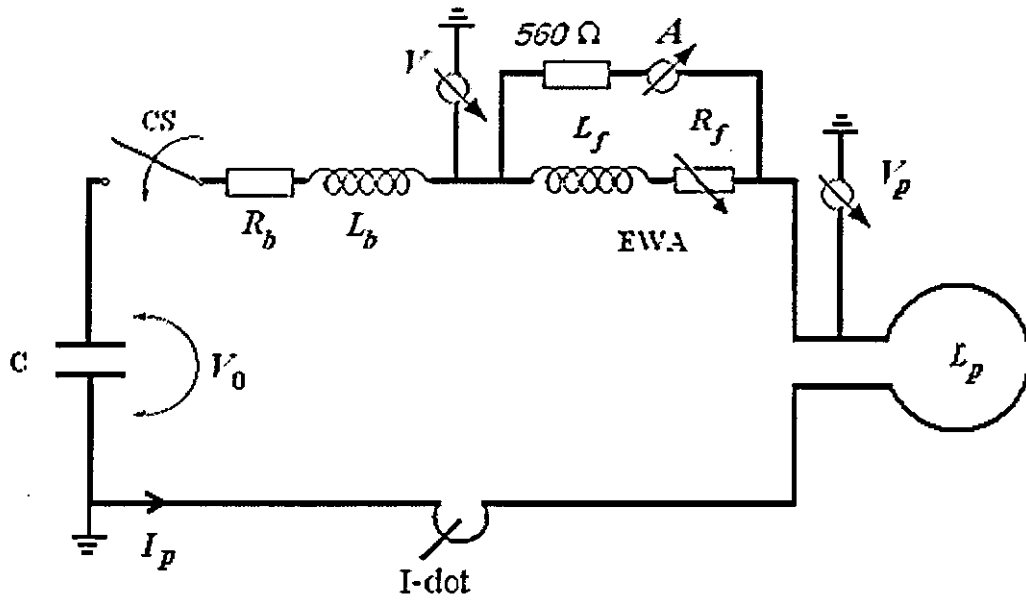


Figure 6.13 Measurement of primary inductance

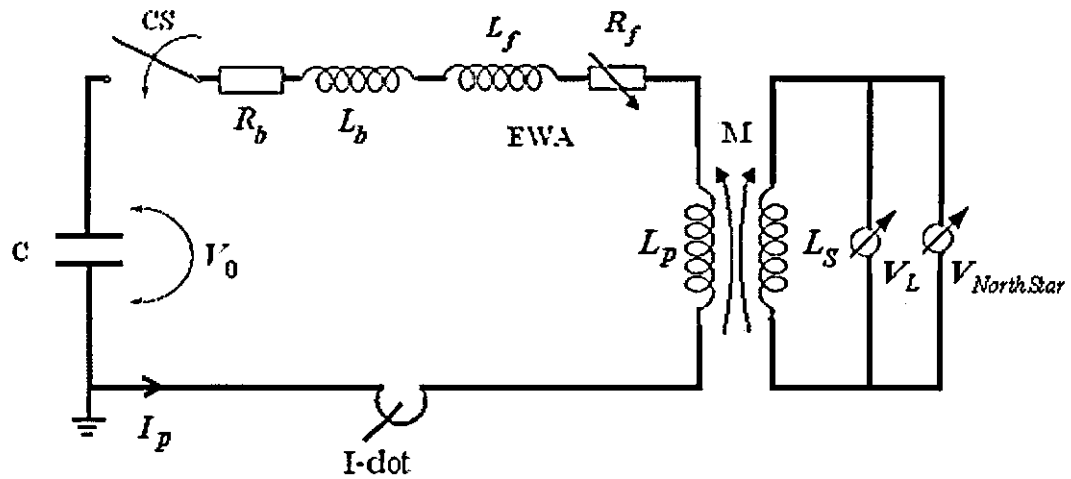


Figure 6.14 Measurement of mutual inductance

The value of the primary inductance, secondary inductance and mutual inductance were all calculated using the filamentary modelling of Section 4.2 as 430 nH , $12 \text{ }\mu\text{H}$ and $1.37 \text{ }\mu\text{H}$ respectively. These values agreed to within 5% of those obtained experimentally, corresponding to the estimated errors in the current and voltage sensors.

6.1.2.4 Transformer performance

In an initial test with the circuit of Figure 6.5, the capacitor was charged to 18.1 kV and the EWA had 6 wires of diameter 250 μm and length 135 mm. The results obtained are given in Figures 6.15 to 6.17, which show the primary current, its time rate-of-change, and the load voltage. Figure 6.17 records a typical result when breakdown occurred at $V_s = 480$ kV substantially above vacuum breakdown voltage (300 kV) to confirm the self-insulating effect. The results are compared with their corresponding theoretical modelling, with the dotted and solid traces in each figure representing measured and simulated results respectively. The general trends of the results have considerable similarity, with any difference most probably introduced by the EWA switch resistance model used in the simulation work, as discussed previously in Section 4.2.

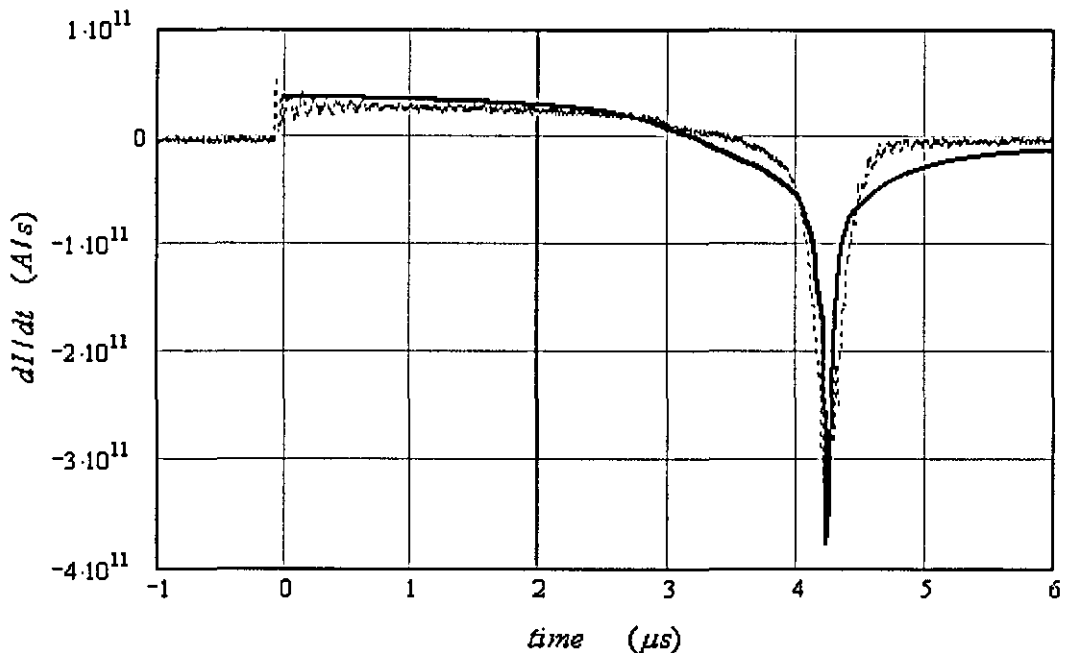


Figure 6.15 dI/dt of primary current

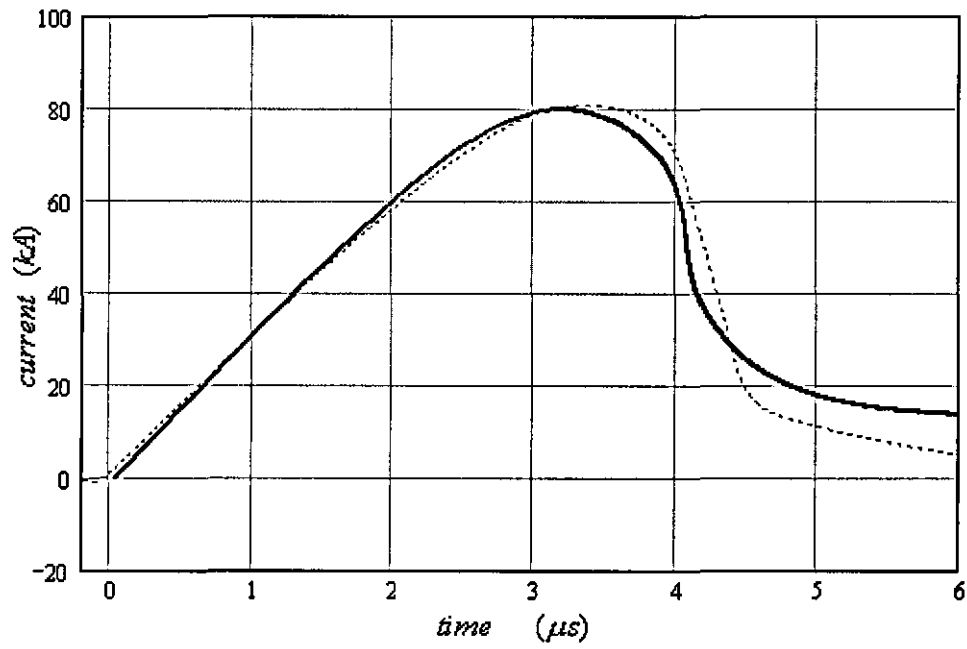


Figure 6.16 Integrated primary current

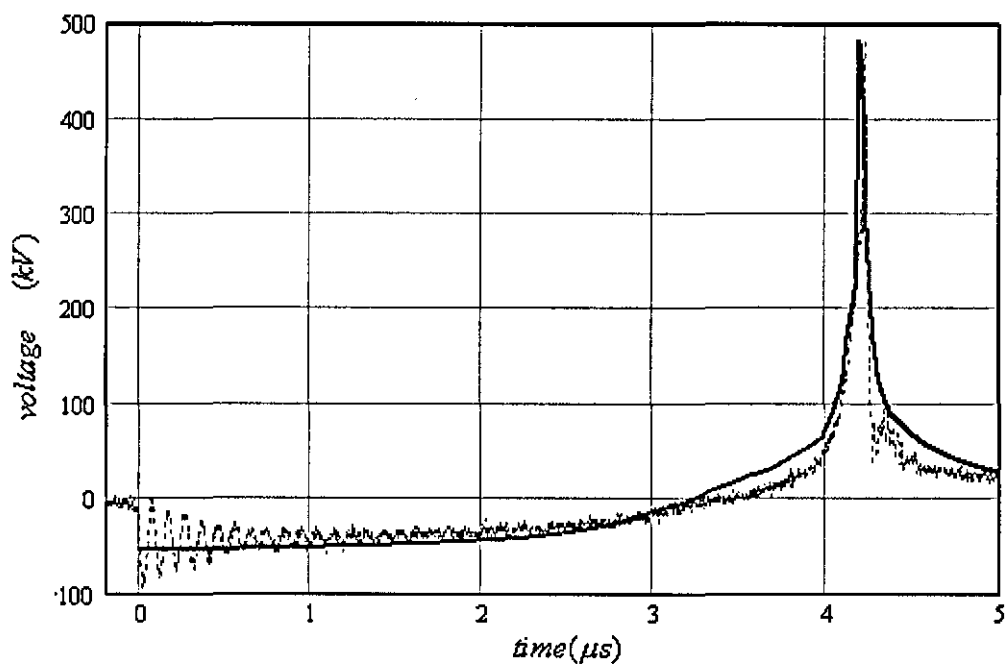
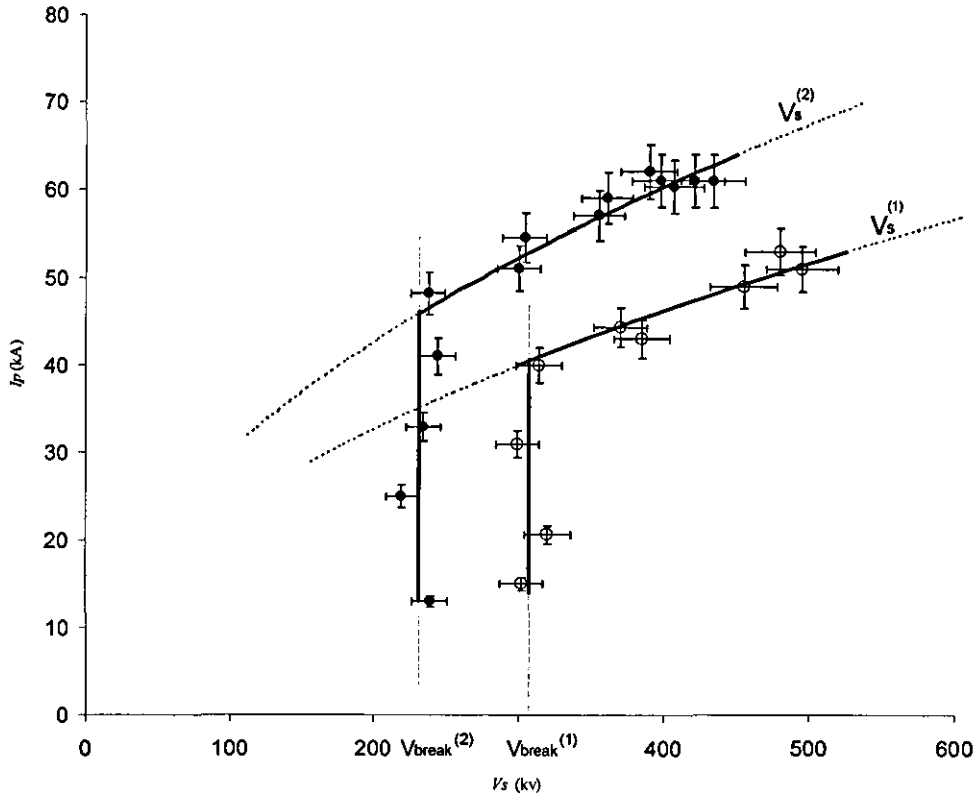


Figure 6.17 Load voltage

6.1.3 Magnetic insulation dependence on primary current [6.1]

Figure 6.18 summarize the principal results from an extensive experimental investigation of the prototype MSI-HVT [6.1], which shows the dependence of the HVT breakdown values V_s on the corresponding primary current. Figure 6.18 also shows that the different characteristics obtained at different vacuum pressures can be represented by $V_s^{(i)} = a_i I_p^2$ ($i = 1, 2$) where $a_1 = 0.187 \times 10^{-3} \text{ V/A}^2$ when the pressure is 10^{-6} Torr and $a_2 = 0.11 \times 10^{-3} \text{ V/A}^2$ when it is 10^{-5} Torr . The corresponding vacuum breakdown voltages, determined for very low values of I_p , are $V_{\text{break}}^{(1)} = 307 \text{ kV}$ and $V_{\text{break}}^{(2)} = 227 \text{ kV}$.



Reference to Paschen's law indicated that the pressure dependence of the data in Figure 6.18 was not expected at these very low gas-pressure-times gap-length products. However, a search of the relevant literature indicated that such a dependence had actually been reported earlier [6.6-6.7]. In addition to this, the local pressure near the secondary windings is not really known. Without any precautions taken, air can be trapped by the electric field grading elastomer mounted on the secondary winding edges, with the degassing process altering the local Paschen conditions. This issue will be investigated in future experiments.

Figure 6.19 presents a typical waveform of V_s and I_p [6.1], and it is evident that the magnetic insulation produced is sufficient for the HVT to function at a voltage significantly above V_{break} (with V_{break} established experimentally with I_p very low). Breakdown occurs about $4.25 \mu s$ after closure of the closing switch when $V_s = 480 \text{ kV}$ and $I_p = 57 \text{ kA}$. The initial charging voltage of the capacitor bank was 19 kV and the pressure 10^{-6} Torr .

Figure 6.20 also presents typical waveforms of V_s and I_p demonstrating vacuum insulation breakdown. Breakdown occurs when $V_s = 300 \text{ kV}$ (below V_{break}) corresponding to $I_p = 32 \text{ kA}$. The initial charging voltage of the capacitor bank was 13 kV , the EWA length 150 mm , the number of wires 6 and the pressure 10^{-6} Torr .

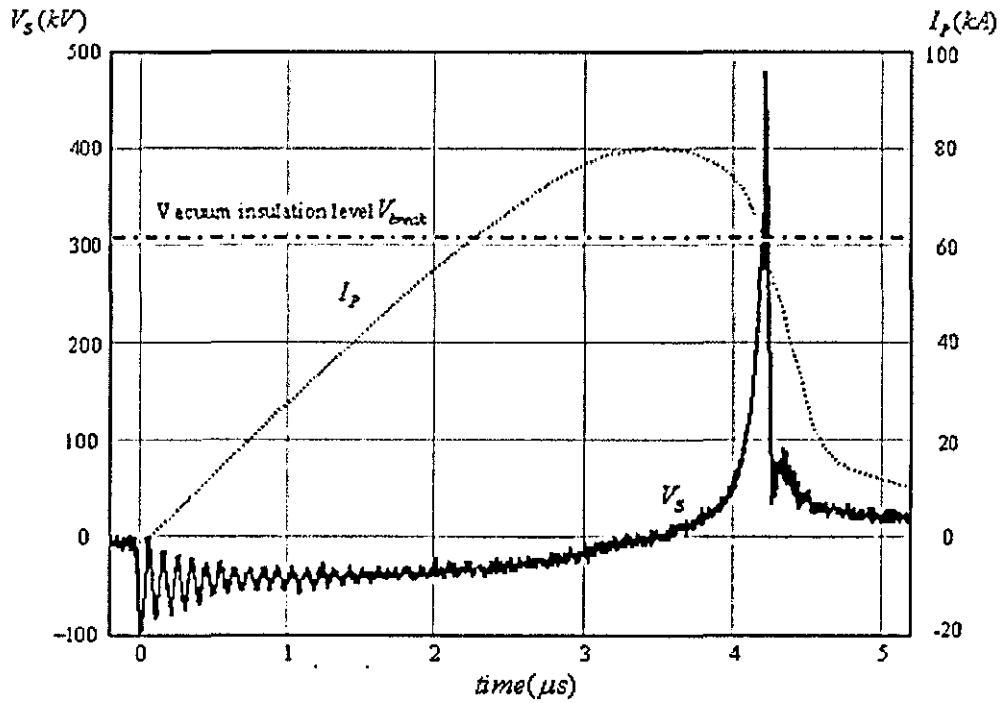


Figure 6.19 Typical waveforms when secondary breakdown-voltage is $V_s = 480$ kV, corresponding to $I_p = 57$ kA. [6.1]

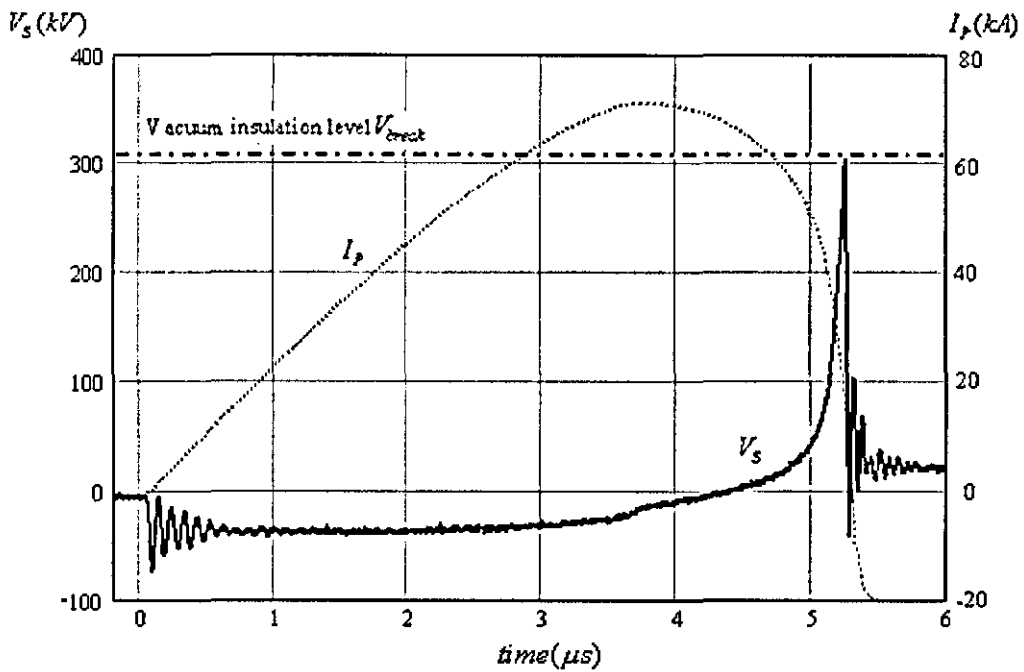


Figure 6.20 Typical waveforms when peak output voltage $V_s = 300$ kV, corresponding to $I_p = 32$ kA

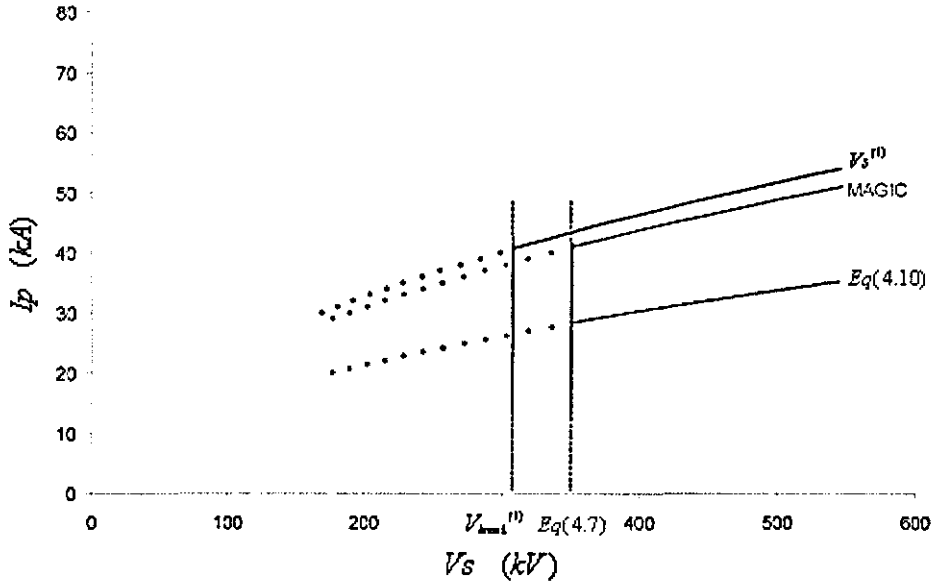


Figure 6.21 Comparison between theoretical predictions for the primary-current/secondary breakdown-voltage characteristics for MSI-HVT based on Equations 4.7 and 4.10 and MAGIC[®] calculation and experimental data as in Figure 6.18 [6.1]

To benchmark the theoretical prediction of Section 4.4.1, theoretical predictions for the primary-current/secondary breakdown-voltage characteristics for MSI-HVT based on Equations 4.7 and 4.10 and MAGIC[®] calculation are shown in Figure 6.21 and compared to experimental data from Figure 6.18 [6.1]. It is clear that the experimental characteristics at 10^{-6} Torr are in good agreement with those predicted by MAGIC[®] calculations (52 kA are required to generate 0.5 MV against 49 kA predicted), which opens the way for the design of a scaled-up version of the prototype transformer. Note that $V_s^{(1)}$ suggests that in order to generate higher voltages, say 1 MV, the required current is only about 80 kA.

6.2 Magnetic insulation of 1 MV HVT [6.8]

A dual-resonant Tesla transformer with helical secondary winding as stated in Chapter 5 was constructed for research on the magnetic insulation effect when established by an auxiliary power source and a cylindrical conducting tube located inside the secondary winding.

6.2.1 Experimental arrangement

The experiment construction and transformer arrangement are based on the theoretic analysis of Chapter 5, with a photograph of the main experimental arrangement being given in Figure 6.22 and the transformer arrangement shown in Figure 6.23. The single-turn primary is constructed from high-conductivity copper sheet (1.2 mm) with an effective primary winding length of 600 mm and an internal diameter of 320 mm. A vacuum chamber, positioned inside the single-turn primary, is evacuated to a pressure of 10^{-5} Torr and houses the helical secondary winding.

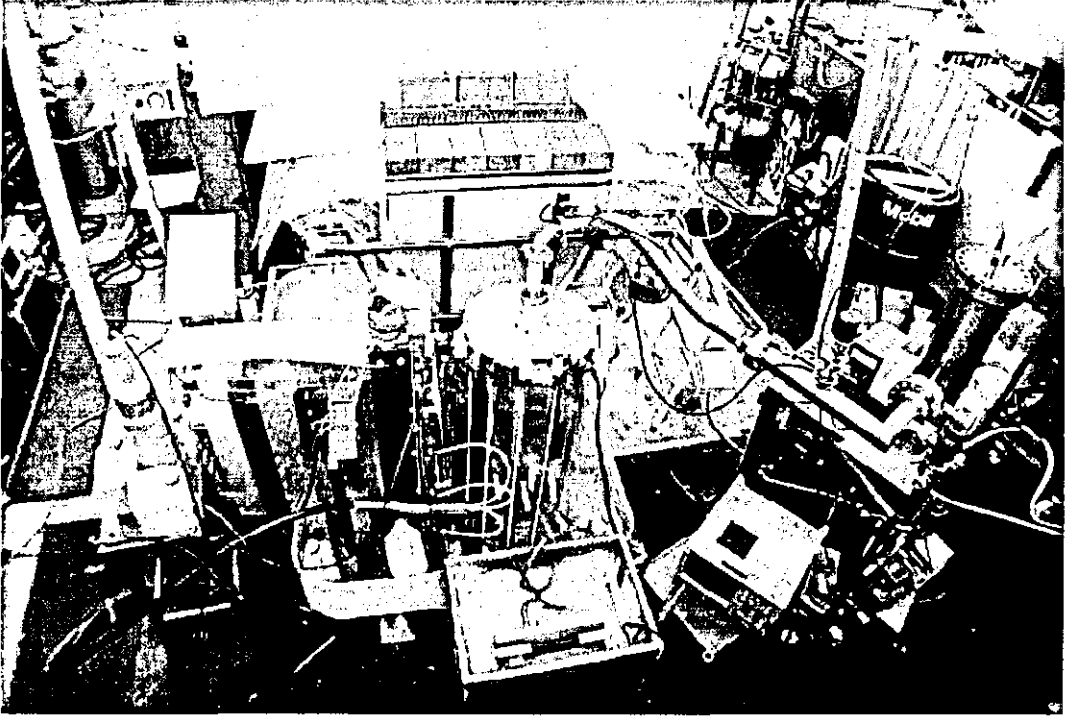


Figure 6.22 Experimental arrangement of 1 *MV* Tesla transformer with magnetic insulation [6.8]

In order to obtain the optimal transformer layout, different transformer secondary coil geometries and conductor types were studied. Firstly, Figure 6.24 (a) shows the 77-turn 220 *mm* diameter, 520 *mm* long helical secondary winding of 2 *mm* thick bare stainless steel conductor wound around a 168 *mm* diameter PVC mandrel. A constant pitch of 6.8 *mm*, is maintained by the polythene spacers shown in Figure 6.24 (b), which limit the area of the flashover surfaces of the transformer secondary. Both inter-turn insulation and the prevention of flashover across the surfaces are maintained mainly by the magnetic insulation when the voltage exceeds 500 *kV*.

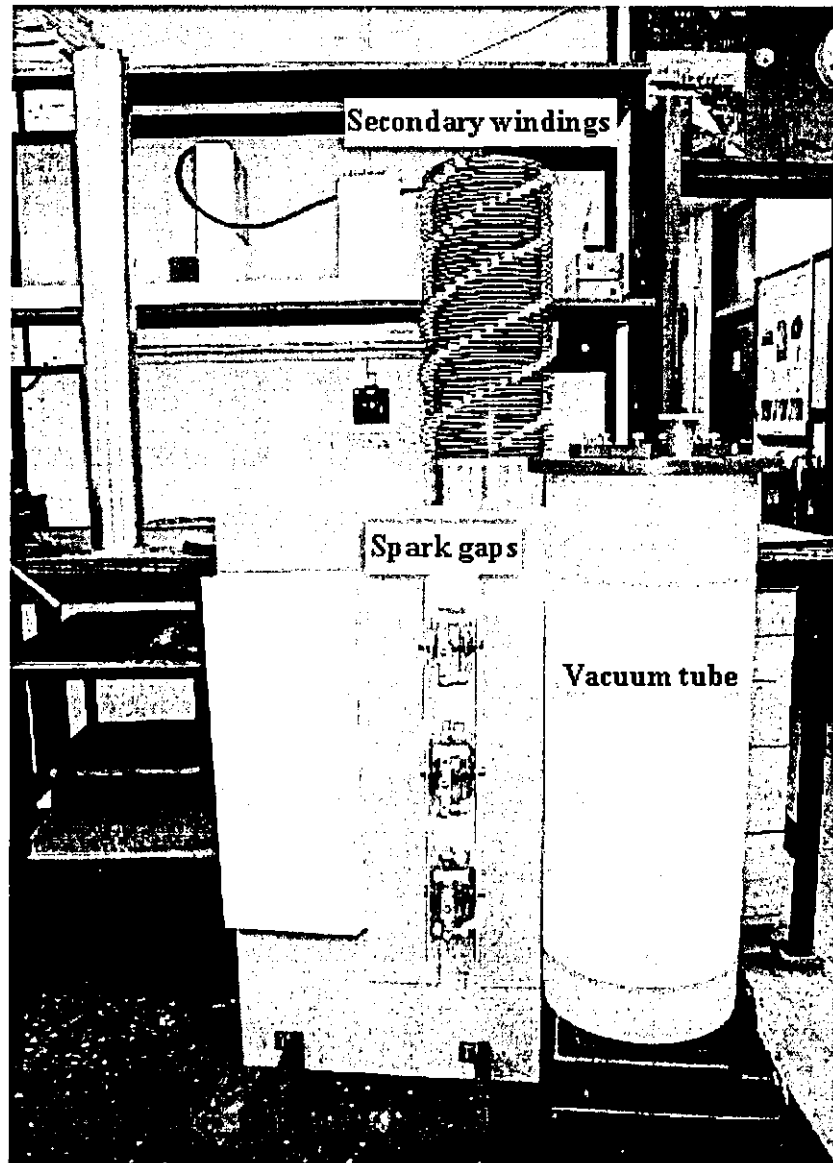
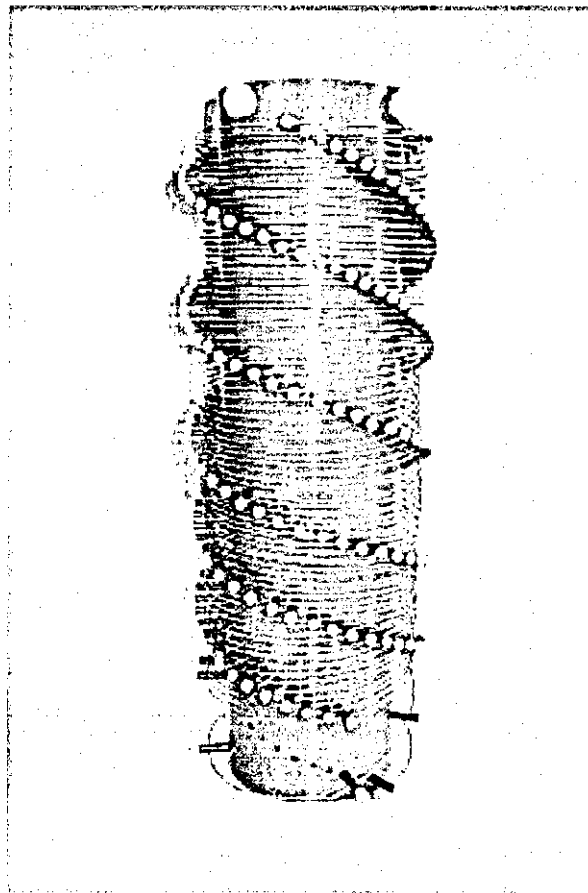
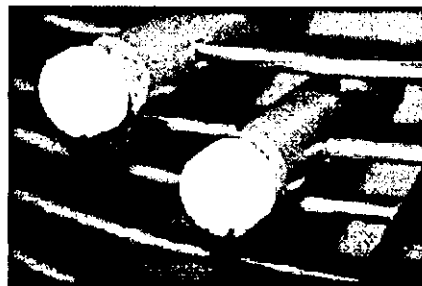


Figure 6.23 Experimental 1 MV Tesla transformer with magnetic insulation



(a)



(b)

Figure 6.24 (a) Secondary winding using 2 mm uninsulated stainless steel wire, (b) PVC spacers between the secondary turns

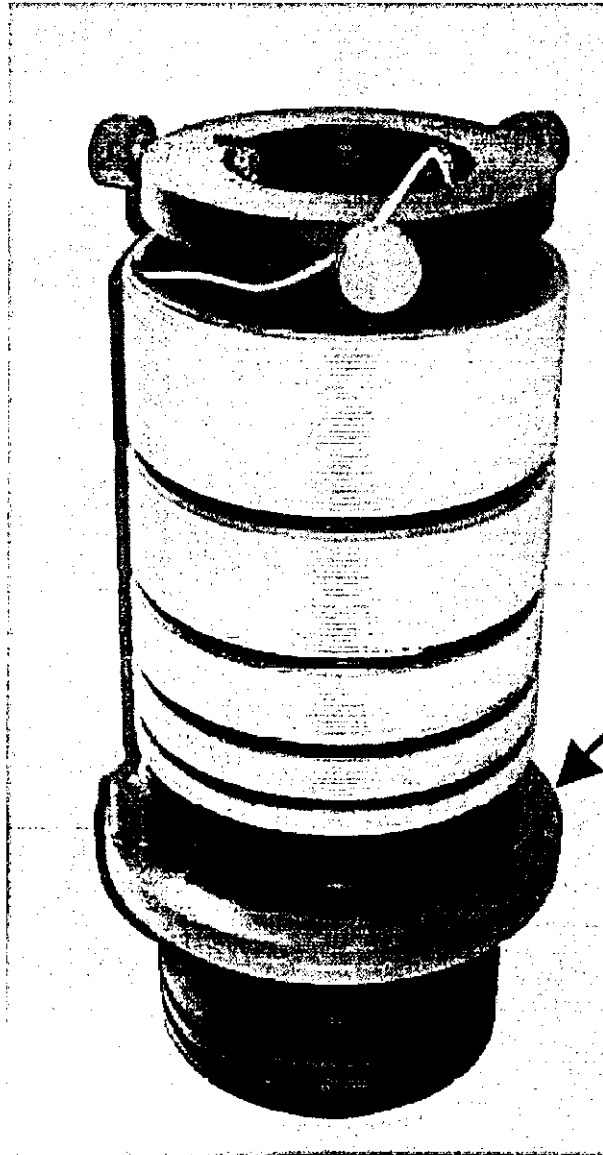


Figure 6.25 Secondary winding with polyethylene insulated conductor enabling a compact design [6.8]

(arrow pointing at HV part of the capacitive divider)

Secondly, Figure 6.25 shows the 73-turn 210 mm diameter, 270 mm long helical secondary winding of 3 mm polyethylene insulated conductor 0.9 mm copper conductor. Here, the inter-turn insulation is provided only by the polyethylene insulation of the conductor (quoted maximum voltage up to 21 kV dc between the inner conductor and the outside of the cable), so that the secondary can be made shorter and much more compact.

However, flashover across the overall surface of the transformer secondary is still inhibited by magnetic insulation and by a novel geometry that separates sections of the secondary turns. Both types of transformer secondary were tested with the same single-turn primary winding. It was determined experimentally that the second secondary coil geometry (Figure 6.25) performs better than the first (i.e. giving a higher output voltage), so that only results for the second geometry are presented.

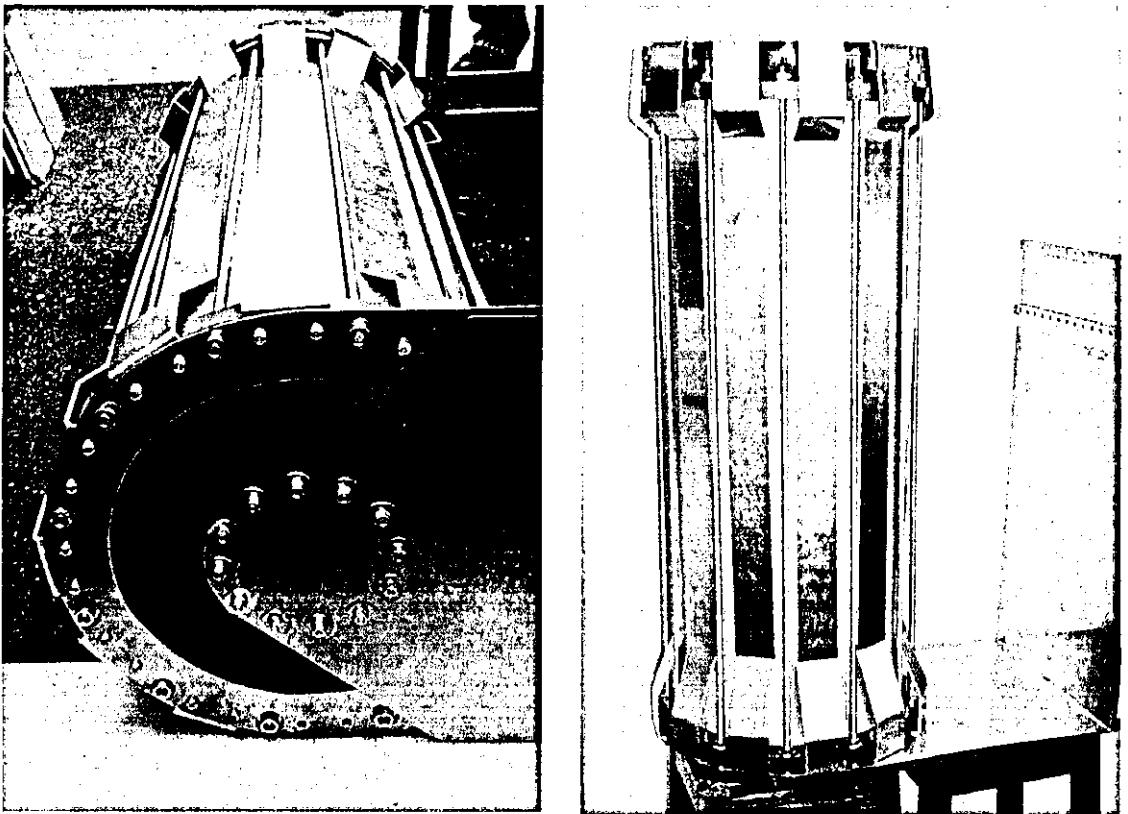


Figure 6.26 Outside view of the auxiliary coil [6.9]

Preliminary experiments showed that for voltages exceeding 0.5 *MV* vacuum insulation was insufficient to prevent electric breakdown of the secondary coil. To obtain higher voltages an external magnetic field needed to be established before the closure of spark gaps, to enable the magnetic insulation to prevent

immediate electric breakdown. This field was provided by an auxiliary coil energized by a current from the auxiliary capacitor bank. The auxiliary coil consists of a 900 mm long, 106 mm diameter aluminum tube inside the secondary coil, with a number of aluminum strips positioned outside the chamber acting as coaxial return conductors, as shown in Figure 6.26. The tube can produce a circular magnetic field orthogonal to the axial and radial electric fields existing between the conductors, which are precisely the conditions required for the onset of magnetic insulation.

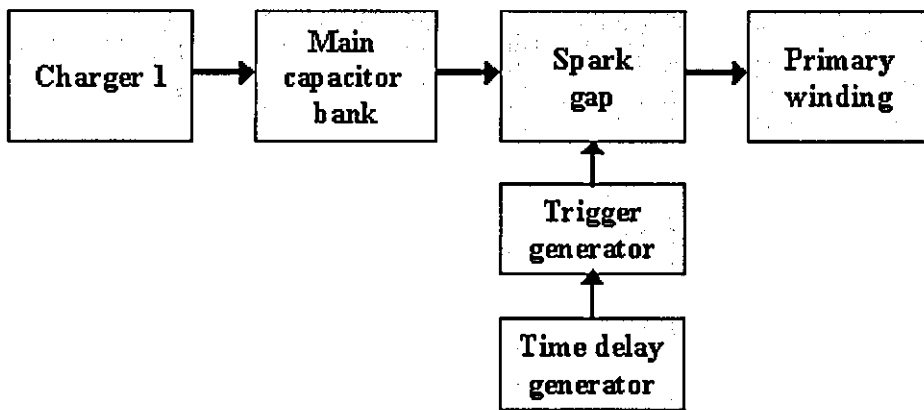


Figure 6.27 Schematic of primary main capacitor bank supply

The main bank comprises forty five 2.7 nH capacitors and is connected to the transformer primary via high precision spark gap switches (Series T-670, Titan Corp. USA, www.titan-psd.com). The switches are pressurized with synthetic air in a symmetrical configuration and with a thin trigger electrode positioned precisely in the plane of symmetry. As each unit has an inductance of about 60 nH, three switches are used in parallel as shown in Figure 6.23 to reduce the overall inductance of the main power source, when the overall inductance of the main power source becomes 31 nH. Operation of the main bank must be accurately synchronized with the auxiliary capacitor bank (Quattro, see Figure 6.22). This is achieved using a time delay pulse generator to trigger the 140 kV high voltage trigger generator (Physics International Model TG-70), which in turn initiates the three spark gap switches. The key elements of the primary main capacitor bank are highlighted in Figure 6.27.

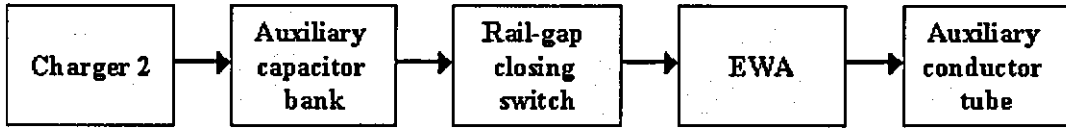


Figure 6.28 Schematic of auxiliary capacitor bank supply

The auxiliary bank comprises four $52.64 \mu F$ capacitors, each with an unusually low internal inductance of $7 nH$. The main parts of the bank system is organized as shown in Figure 6.28. The capacitors are connected to a flat parallel-plate transmission line via a rail-gap closing switch (Model 40302, Titan Corp). The switch is pressurized with a mixture of oxygen (10%) and argon (90%). Between the closing switch and the load there is an exploding wire array (EWA), optimized to open the circuit immediately after the peak of the current to protect the capacitor bank from high-current reversal oscillations. The overall inductance of the auxiliary power source is less than $40 nH$, including the contribution from the EWA (40 – 80 OFHC copper wires of $250 mm$ diameter and $90 mm$ length). The load consists of the central cylindrical conductor, a $900 mm$ long, $106 mm$ diameter aluminium tube and a number of aluminium strips acting as coaxial return conductors. With a load inductance of about $250 nH$ and a capacitor charging voltage of $25 kV$, currents up to $600 kA$ can be achieved.

Figure 6.29 shows the main experimental arrangement. When the auxiliary capacitor bank is fully charged, a command input triggers the $100 kV$ Marx generator (Model 40230, Titan Corp), which in turn initiates the rail gap switch. A signal from the Marx trigger circuit is sent to the time delay unit, which synchronizes the two banks so that the maximum current from the auxiliary capacitor bank coincides with the maximum voltage being generated in the transformer secondary winding [6.8].

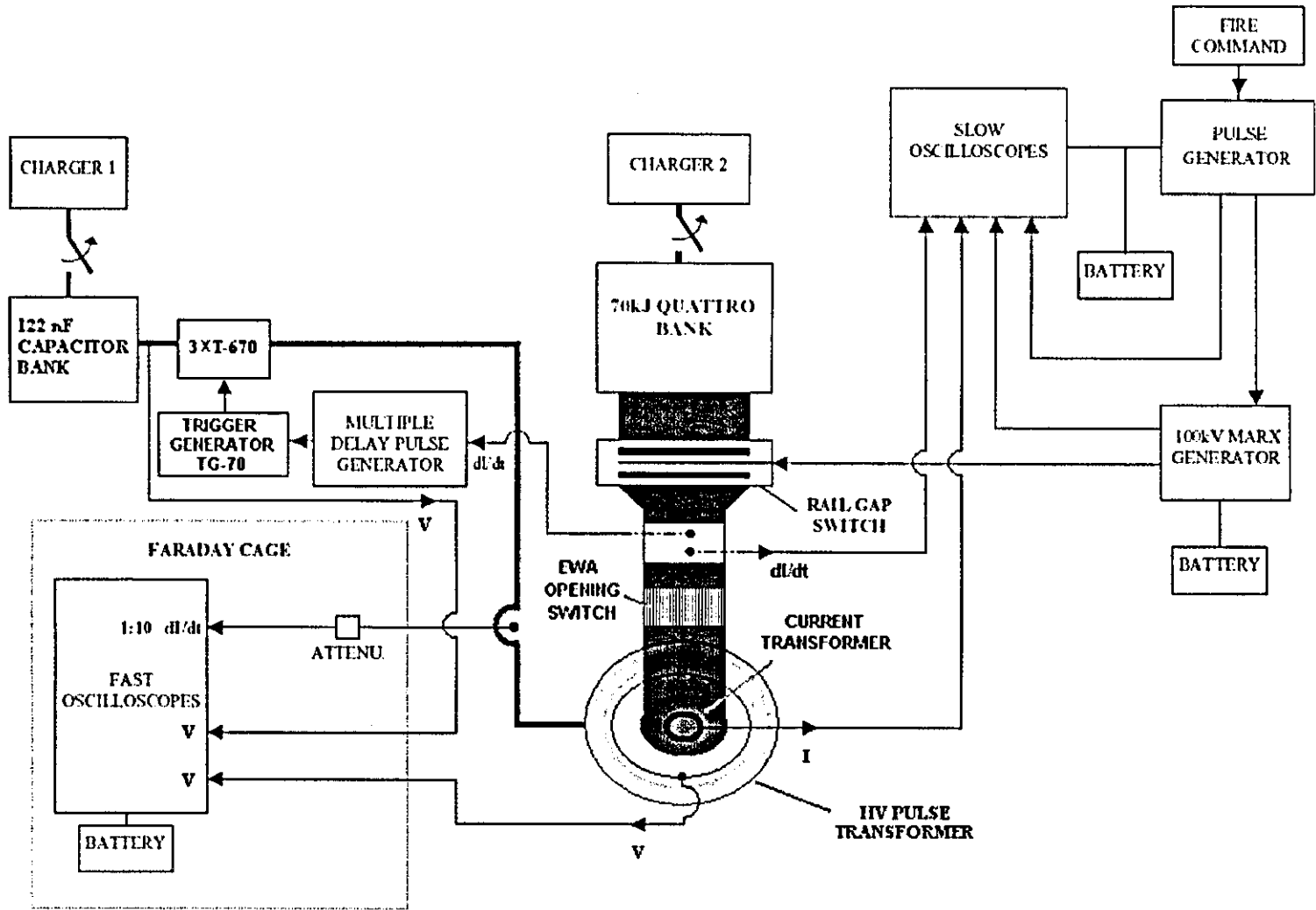


Figure 6.29 Schematics of experimental arrangement [6.8]

6.2.2 Diagnostic methods

A long inductive pick-up probe calibrated in situ and located in a tunnel in the parallel-plate transmission line from the auxiliary capacitor bank is used to monitor both the time rate-of-change of the current and the current itself. Also, the load current of the auxiliary capacitor bank is measured by a 20 *MHz* current transformer enclosing one of the eleven coaxial return conductors to monitor possible irregularities in the load. Three inductive pick-up probes positioned in a tunnel in the flat transmission line of the main capacitor bank monitor the current in the transformer primary and the performance of the spark gap switches (the pick-up probes are located close to the spark gaps). A commercial 80 *MHz*, 100 *kV* capacitive divider records the main capacitor bank voltage, and a fast LU built, 1 *MV* capacitive divider with a low capacitance that does not load the secondary transformer circuit, measures the output voltage of the transformer.

6.2.3 Analysis of results

Signals from the capacitive probe following the last (HV) turn of the transformer secondary are shown in Figure 6.30. The maximum injection field current from the auxiliary capacitor bank is 0.58 *MA* establishing a field of about 1 *T* in the vicinity of the secondary winding. As Figure 6.30 shows, when the main capacitor was charged to 28 *kV*, that was adequate to provide insulation up to an output voltage of 1 *MV*. Dotted lines represent calculated predictions of the transformer performance and show a good agreement with the experimental results. After testing the transformer performance with magnetic insulation, a few shots were made at different charging voltages without magnetic insulation present, which established that the breakdown in vacuum occurred at charging voltages of about 11 *kV* – 13 *kV* and secondary voltages of 400 *kV* – 500 *kV*.

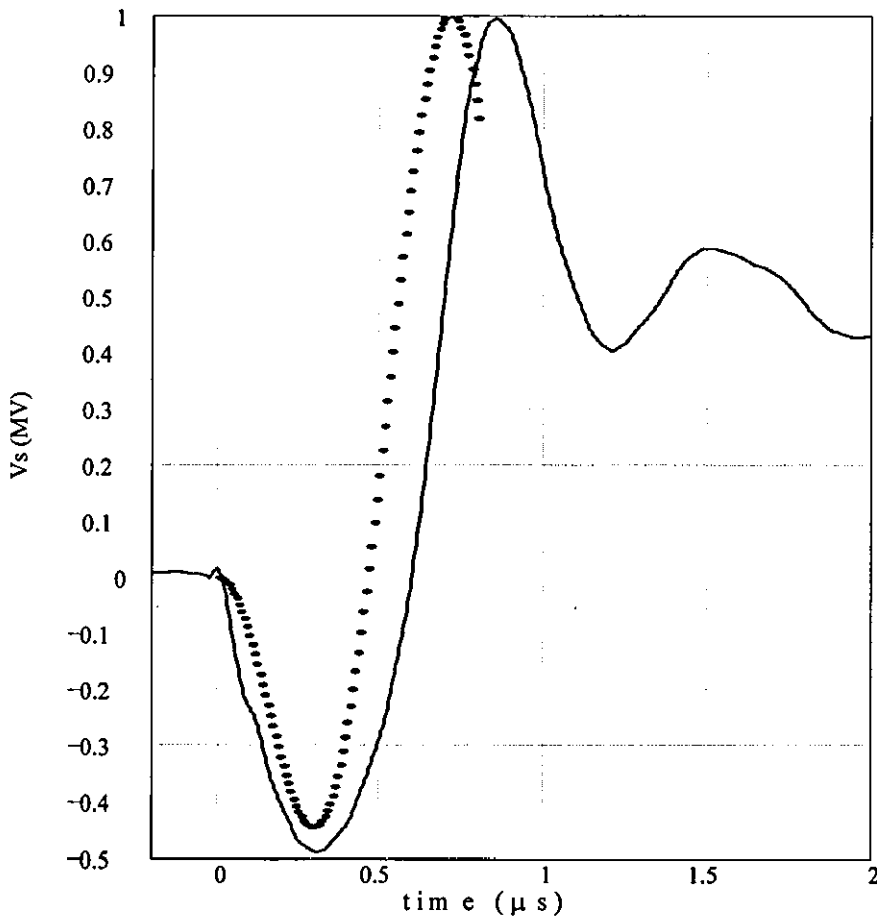


Figure 6.30 Magnetically insulated output voltage signal with maximum injection field current of 0.58 MA corresponding to a field of about 1 T. C_b charged to 28 kV

7 Conclusion

This thesis has described the successful implementation of magnetic insulation techniques into two different high voltage pulse transformers, leading to simple, compact and lightweight units. It is believed that they represent the first working examples of magnetically-insulated transformers anywhere in the world and open the way to the multi-*MV* pulse transformers design.

The numerical modelling presented in the thesis aimed to study and understand pulsed power systems and their intimate nature and, based on this knowledge, to further develop them. The 2D filamentary technique has been continuously improved at Loughborough University and has been successfully applied in a very wide range of pulsed power applications as electromagnetic launchers [7.1], ultrahigh magnetic field generators [7.2], explosively driven flux-compression generators [7.3], multi and single-turn inductive launchers [7.4-7.5] and electromagnetic flux-compression [7.6]. In this thesis, detailed 2D filamentary models for the two high-voltage pulse transformers were successfully benchmarked in Chapter 2 against both Loughborough data and experimental results obtained from elsewhere, with the error being less than 3%. The model was then applied to the design and optimization process in Chapters 4 and 5, and finally again compared with experimental data in Chapter 6. The agreement evident confirms that the present 2D filamentary model can be used with confidence to predict accurately the dynamic performances of HVTs in high power conditioning systems. The models is at present widely used at Loughborough in designing HVT based compact conditioning circuits.

An extended study of electric field enhancement optimization was carried out by finite element analysis. A good solution was demonstrated [7.7] in the development of a 3 *MV* HVT and was improved [7.8] in the Loughborough 15-turn spiral-strip HVT by a similar cage configuration to that suggestion in [7.7]. The results reported in Chapter 3 shows the ring cage technique not only reduces the maximum electric field strength by about 50% but also produces a more homogeneous distribution.

A magnetically self insulating transformer has been demonstrated for voltages up to 0.5 MV in Chapter 4, with very little conventional insulation and no oil, using simple and effective techniques for grading the electric fields. Experimental results in Chapter 6 illustrate that the maximum breakdown voltage is controlled by the primary current (the source of the insulating magnetic field) and it is confirmed in Chapter 5 that this can be accurately predicted by detailed numerical modelling. Implementation of the magnetic self-insulated HVT into a compact system powered by a flux compression generator should offer an important advantage, as the exponentially rising primary current will not allow the generation of high voltages at a low primary current, thereby avoiding the possibility of an early breakdown. Although the HV output will always be relatively short (between 100 ns and 200 ns) due to the EWA action tending to suppress the current and therefore the magnetic insulation conditions, the time scale is clearly sufficient to drive a high-power microwave source such as a vircator, as proved by recent experiments in Loughborough using a conventional air-core transformer [7.9].

A magnetically insulated pulse transformer was designed for operation at MV levels in Chapter 5, based on a Tesla transformer operated in vacuum and used in a dual-resonant mode. The results in Chapter 6 show a transformer magnetically insulated output voltage to 1 MV , with the maximum injection field current of 0.58 MA corresponding to a field of about 1 T . The very important features of reduced mass and volume will be exploited in future transformer design scaled-up for multi- MV operation.

In conclusion, the theoretical and experimental work and research presented in the thesis has laid a solid base for future scientific research.

Published papers that include J. Luo as a co-author

- [1] J. Luo, B. M. Novac and I. R. Smith, "Accurate modelling of high-current, high-voltage air-cored transformers", *2nd European Pulsed Power Symposium, Hamburg, September, 2004*, pp. 207-211
- [2] B. M. Novac, I. R. Smith, J. Luo and J. Brown, "High-voltage magnetically insulated transformers", *2nd European Pulsed Power Symposium, Hamburg, September, 2004*, pp. 186-189
- [3] J. Luo, B. M. Novac and I. R. Smith, "Design of high-current, high-voltage air cored transformer", *1st Power and Renewable Energy Division Conference, Loughborough, April, 2005*, pp. 46-49
- [4] J. Luo, B. M. Novac, I. R. Smith and J. Brown, "Fast and accurate two-dimensional modelling of high-current, high-voltage air-cored transformers", *J. Phys. D: Appl. Phys.*, vol. 38, pp. 955-963, 2005
- [5] J. Luo, B. M. Novac and I. R. Smith, "Accurate modelling of high-current, high-voltage air-cored transformers", *15th IEEE International Pulsed Power Conference, Monterey, CA, June, 2005*
- [6] B. M. Novac, M. Istenic, J. Luo, et al., "A 10 GW pulsed power supply for HPM sources" *15th IEEE International Pulsed Power Conference, Monterey, CA, June, 2005*
- [7] J. Luo, M. Istenic, B. M. Novac, I. R. Smith and J. Brown, "Design of 500 kV pulse transformers using magnetic insulation", *IEE Pulsed Power Symposium, Basingstoke, September, 2005*, pp. 17/1-17/4
- [8] B. M. Novac, M. Istenic, J. Luo, et al., "A 10 GW pulsed power supply for HPM sources", *IEE Pulsed Power Symposium, Basingstoke, September, 2005*, pp. 7/1-7/4
- [9] M. Istenič, B. M. Novac, J. Luo, R. Kumar, I. R. Smith and J. Brown, "Magnetic insulation techniques for MV pulse transformer design", *27th IEEE Power Modulator Symposium and 2006 High Voltage Workshop, Washington, DC, May, 2006*

- [10] M. Istenič, B. M. Novac, **J. Luo**, R. Kumar, I. R. Smith and J. Brown, "Self magnetic insulation of high-voltage pulse transformers", *2006 Megagauss XI Conference, Imperial College, London, September, 2006*
- [11] **J. Luo**, M. Istenic, B. M. Novac, I. R. Smith, N. Hook, R. Kumar and J. Brown, "High voltage pulse transformers with magnetic insulation", *1st Euro-Asian Pulsed Power Conference, Chengdu, China, September, 2006*
- [12] **J. Luo**, B. M. Novac, I. R. Smith and J. Brown, "Accurate modelling of high-voltage pulsed transformers", *1st Euro-Asian Pulsed Power Conference, Chengdu, China, September, 2006*
- [13] M. Istenič, B. M. Novac, **J. Luo**, R. Kumar, I. R. Smith and J. Brown, "High Voltage Pulse Transformer Employing Magnetic Self-Insulation", *IET Pulsed Power Symposium 2006, Warrington, UK, October, 2006*, pp. 41-44
- [14] M. Istenič, B. M. Novac, **J. Luo**, R. Kumar, I. R. Smith and J. Brown, "Magnetically Insulated 1 MV Pulse Transformer", *IET Pulsed Power Symposium 2006, Warrington, UK, October, 2006*, pp. 66-70
- [15] B. M. Novac, M. Istenič, **J. Luo**, I. R. Smith et. al., "A 10-GW Pulsed Power Supply for HPM Sources" *IEEE Trans. on Plasma Sci.*, vol. 345, pp. 1814-1821, 2006
- [16] M. Istenič, B. M. Novac, **J. Luo**, R. Kumar and I. R. Smith, "A 0.5 MV magnetically self-insulated pulsed transformer", *J. Phys. D: Appl. Phys.*, vol. 39, pp. 4529-4535, 2006
- [17] M. Istenič, B. M. Novac, **J. Luo**, R. Kumar and I. R. Smith, "A 1 MV magnetically insulated Tesla transformer", *J. Phys. D: Appl. Phys.*, (submitted for publication)

References

- [1.1] K. H. Schoenbach, M. Kristiansen and G. Schaefer, "A review of opening switch technology inductive energy storage", *Proc. IEEE*, vol. 72, pp. 1019-1040, 1984
- [1.2] L. X. Schneider and G. J. Lockwood, "Engineering high reliability", *Low jitter Marx generators Proceedings of the 5th IEEE Pulsed Power Conference*, pp. 780-783, 1985
- [1.3] N. W. Harris and H. I. Milde, "15 kJ LC generator: low inductance device for a 100 GW pulsed electron accelerator", *J. Vac. Sci. Technol.*, vol. 12, pp. 1188-1190, 1975
- [1.4] R. A. Fitch, T. S. Howell, "Novel principle of transient high-voltage generation", *Proc. IEE*, vol. 111, no. 4, pp. 849-855, 1964
- [1.5] F. Ruhl and G. Herziger, "Analysis of the spiral generator", *Rev. Sci. Instrum.*, vol. 51, pp. 1541-1547, 1980
- [1.6] G. J. Rohwein, "A three megavolt transformer for PFL pulse charging", *IEEE Trans on Nuclear Science*, vol. NS-26, pp. 4211-4213, 1979
- [1.7] G. J. Rohwein, "Air core pulse transformers for high power lasers", *Laser Focus*, pp. 70-74
- [1.8] J. C. Martin, P. D. Champney and D. A. Hammer, "Notes on the construction methods of a Martin high-voltage pulse transformer", *Cornell University Report*, 1976
- [1.9] J. C. Martin, and I. D. Smith, "High voltage pulse generating transformer", *US Patent*, no. 3456221, 1969
- [1.10] M. Istenič, B. M. Novac, J. Luo, R. Kumar and I. R. Smith and J. Brown, "Magnetically Insulated 1 MV Pulse Transformer", *IET Pulsed Power Symposium 2006, IET, Warrington, UK, October 2006*, pp 66-70
- [1.11] M. Istenič, B. M. Novac, J. Luo, R. Kumar and I. R. Smith "A 0.5 MV magnetically self-insulated pulsed transformer", *J. Phys. D: Appl. Phys.*, vol. 39, pp. 4529-4535, 2006

- [1.12] M. Goodman, "J C Charlie Martin: a UK tribute", *12th IEEE Int. Pulsed Power Conf. (Monterey, CA, 1999)* ed C Stallings and H Kirbie, pp. 49-58, 1999
- [1.13] B. M. Novac and I. R. Smith, "A compact 0.5 MV, 1 GW twin-output pulser", *Pulsed Power 2001, IEE Symposium*, 2001
- [1.14] M. Y. Wang and M. S. Di Capua, "Operating point of long magnetically insulated vacuum transmission lines", *J. Appl. Phys.*, vol. 51, no. 11, pp. 5610-5619, 1980
- [1.15] J. M. Creedon, "Magnetic cutoff in high-current diodes", *J. Appl. Phys.*, vol. 48, no. 3, pp. 1070-1077, 1975
- [1.16] Y. Carmel and J. A. Nation, "Instability of an unneutralized relativistic electron beam", *Phys. Rev. Lett*, vol. 31, pp.286-289, 1973
- [1.17] T. J. Orzechowski and G. Bekefi, "Current flow in a high-voltage diode subjected to a crossed magnetic field", *Phys. Fluids*, vol. 19, no.1, pp.43-51, 1976
- [1.18] P. Ottinger, S. A. Goldstein, and R. A. Meger, "Theoretical modelling of the plasma erosion opening switch for inductive storage applications", *J. Appl. Phys*, vol. 56, no. 3, pp.774-784, 1984
- [1.19] F. Winterberg, "Magnetically insulated transformer for attaining ultrahigh voltage", *Rev. Sci. Instrum*, vol. 41, no. 12, pp. 1756-1763, 1970
- [1.20] B. M. Novac, I. R. Smith and J. Brown, "Magnetically self-insulated transformers", *J. Phys.D: Appl. Phys*, vol. 35, pp. 1467-1472, 2002
- [1.21] R. V. Lovelace and Edward Ott, "Theory of magnetic insulation" *Physics of Fluids*, vol. 17, pp. 1263-1268, 1974
- [2.1] D. F. Rankin, B. M. Novac, I. R. Smith and M. Hubbard, "Complex multi-physical modelling of pulsed ultrahigh magnetic field systems", *Proc2nd European Pulsed Power Symposium, Hamburg, Germany* , pp. 212-216, 2006
- [2.2] N. Miura N and S. Chikazumi, "Computer simulation of megagauss field generation by electromagnetic flux-compression", *Japan. J. Appl. Phys.*, vol. 18, pp. 553-564, 1979
- [2.3] N. Miura and K. Nakao, "Computer analysis of megagauss field generation by condenser bank discharge" *Japan. J. Appl. Phys.*, vol. 29, pp. 1580-1599, 1990

-
- [2.4] B. M. Novac, I. R. Smith and M. C. Enache, "Accurate modeling of the proximity effect in helical flux-compression generators", *IEEE Trans. Plasma Sci.*, vol. 28, pp. 1353-1355, 2000
- [2.5] B. M. Novac, I. R. Smith, M. C. Enache and H. R. Stewardson, "Simple 2D model for helical flux-compression generators", *Laser and Particle Beams*, vol. 15, pp. 379-95, 1997
- [2.6] K. Gregory, I. R. Smith, V. V. Vadher and M. J. Edwards, "Experimental validation of a capacitor discharge induction launcher model", *IEEE. Trans. Magnetics*, vol. 31, pp. 599-603, 1995
- [2.7] B. M. Novac, I. R. Smith, M. C. Enache and P. Senior, "Studies of a very high efficiency electromagnetic launcher", *J. Phys. D: Appl. Phys.*, vol. 35, pp.1447-1457, 2002
- [2.8] B. M. Novac, I. R. Smith and M. Hubbard, "2D modeling of electromagnetic flux-compression in θ -pinch geometry", *IEEE Trans. Plasma Sci.*, vol. 32, no. 5, pp. 1896-1901, 2004
- [2.9] B. M. Novac, I. R. Smith, P. E. Jarvis and C. J. Abbott, "Accelerating conductors by electromagnetic action through metallic shields" *IEEE. Trans. Magnetics*, vol. 39, pp. 305-309, 2003
- [2.10] J. C. Maxwell, "*A treatise on electricity and magnetism*", (Oxford: Clarendon Press) 3rd edition, 1904
- [2.11] W. M. Widner, "Warp-10: a numerical simulation model for the cylindrical reconnection launcher", *IEEE Trans. Magnetics*, vol. 27, pp. 634-638, 1991
- [2.12] A. Y. Wu and K. S. Sun, "Formulation and implementation of the current filament method for analysis of current diffusion and heating in conductors in railguns and homopolar generators", *IEEE. Trans. Magnetics.*, vol. 25, pp. 610-615, 1989
- [2.13] W. R. Smythe, "*Static and dynamic electricity*", (NY: McGraw-Hill), 1950
- [2.14] F. Jahnke and E. Emde, "*Tables of functions*", (NY: Dover Publications), 1933
- [2.15] W. H. Press, B. P. Flannery, S. A. Tenkolsky and W. T. Vetterling, "*Numerical recipes in pascal: the art of science computing*", (Cambridge: Cambridge University Press), 1989

- [2.16] F. W. Grover, "*Inductance calculations*", (NY: Dover), 1973
- [2.17] H. M. Arnold, "The resistance of round-wire single-layer inductance coils", *Proc. IEE*, vol. 98, pp. 94-100, 1951
- [2.18] B. M. Novac, I. R. Smith and J. Brown, "A high-power high-voltage multi-pulse twin-output driver for radiation generators", *J. Phys. D: Appl. Phys.*, vol. 34, pp. 3510-3514, 2001
- [2.19] J. Zhang, J. Dickens, M. Giesselmann, J. Kim, E. Kristinansen, J. Mankowski, D. Garcia and M. Kristiansen, "The design of a compact pulse transformer", *12th IEEE Int. Pulsed Power Conf. (Monterey, CA)*, ed C. Stalling and H. Kirbie, pp. 704-707, 1999
- [2.20] R. E. Reinovsky, R. G. Colclaser, J. M. Welby and E. A. Lopez, "Energy storage transformer power conditioning systems for mega joule class flux compression generators", *Megagauss technology and pulsed power applications*, ed C. M. Fowler, R. S. Caird and D. J. Erikson, (NY: Plenum), pp. 575-582, 1987
- [2.21] N. F. Roderick, B. J. Kohn, W. F. McCullough, C. W. Beason, J. A. Lupo, J. D. Letterio, D. A. Kloc and T. W. Hussey, "Theoretical modeling of electromagnetically imploded plasma liners", *Laser Particle Beams*, vol. 1, pp. 181-206, 1983
- [3.1] W. R. Smythe, "Static and dynamic Electricity", McGraw-Hill Book Co., New York, NY., 1950
- [3.2] S. T. Ko, "Field enhancement optimisation of an air-cored spiral strip pulse transformer", *IEEE Trans. Plasma Science*, vol. 33, pp. 1268-1272, 2005
- [3.3] T. H. Martin, A. H. Guenther and M. Kristiansen, "Nanosecond pulse techniques", *Adv. Pulsed Power Technol.*, vol. 3, pp. 35-74, 1996
- [3.4] G. J. Rohwein, "Design of pulse transformers for PFL charging", *2nd IEEE Int. Pulsed Power Conf.*, pp. 87-90, 1979
- [3.5] H C Miller, "Values of the electron emission functions $\nu(y)$, $t(y)$, and $\Theta(y)$; for $y \geq G_i$ ", *J. Franklin Inst*, vol. 287, pp. 347-351, 1969
- [3.6] M Giesselmann, J Zhan, T Heeren et al, "Pulse power conditioning with a transformer for an inductive energy storage system", *Proceedings of the*

- 12th IEEE International Pulse Power Conference, Monterey, California, June 27-3, 1999*
- [4.1] B. M. Novac and I. R. Smith, "Consideration of an autonomous compact source for high-power microwave applications", *IEEE Trans. Plasma Sci.*, vol. 28, pp. 620-623, 2000
 - [4.2] B. M. Novac, I. R. Smith and J. Brown. "A high-power high voltage multi-pulse twin-output driver for radiation generators", *J. Phys. D: Appl. Phys.*, vol. 34, pp. 3510-3514, 2001
 - [4.3] M. Goodman, "J C Charlie Martin: a UK tribute", *12th IEEE Int. Pulsed Power Conf. (Monterey, CA, 1999)* ed C Stallings and H Kirbie, pp. 49-58, 1999
 - [4.4] B. M. Novac, I. R. Smith and J. Brown, "Magnetically self-insulated transformers", *J. Phys.D: Appl. Phys.*, vol. 35, pp. 1467-1472, 2002
 - [4.5] M. Y. Wang and M. S. Di Capua, "Operating point of long magnetically insulated vacuum transmission lines", *J. Appl. Phys.*, vol. 51, no. 11, pp. 5610-5619, 1980
 - [4.6] J. M. Creedon, "Magnetic cutoff in high-current diodes", *J. Appl. Phys.*, vol. 48, no. 3, pp. 1070-1077, 1975
 - [4.7] Y. Carmel and J. A. Nation, "Instability of an unneutralized relativistic electron beam", *Phys. Rev. Lett.*, vol. 31, pp. 286-289, 1973
 - [4.8] T. J. Orzechowski and G. Bekefi, "Current flow in a high-voltage diode subjected to a crossed magnetic field", *Phys. Fluids*, vol. 19, no.1, pp. 43-51, 1976
 - [4.9] P. Ottinger, S. A. Goldstein, and R. A. Meger, "Theoretical modelling of the plasma erosion opening switch for inductive storage applications", *J. Appl. Phys.*, vol. 56, no. 3, pp. 774-784, 1984
 - [4.10] R. J. Cliffe, J. Brown and I. R. Smith, "Interfacing transformer for a pulsed load current exceeding 1MA", *J. Phys. D: Appl. Phys.*, vol. 36, pp. 1651-1654, 2003
 - [4.11] I. Boscolo, G. Brautti, R. Coisson, M. Leo and A. Luches, "Tesla transformer accelerator for the production of intense relativistic electron beams" *Rev. Sci. Instrum.*, vol. 46, pp. 1535-1538, 1975

- [4.12] V. P. Gubanov, S. D. Korovin, I. V. Pegel, A. M. Roitman, V. V. Rostov and A. S. Stepchenko, "Compact 1000 PPS high-voltage nanosecond pulse generator", *IEEE Trans. Plasma Sci.* vol. 25, pp. 258-264, 1997
- [4.13] M. Istenič, B. M. Novac, J. Luo, R. Kumar and I. R. Smith, "A 0.5 MV magnetically self-insulated pulsed transformer", *J. Phys. D: Appl. Phys.*, vol. 39, pp. 4529-4535, 2006
- [4.14] H. R. Stewardson, B. M. Novac, I. R. Smith, and M. C. Enache, "Multi-stage pulse compression using an exploding foil and a PEOs", *11th IEEE International Pulsed Power Conference, Baltimore, USA, July, 1997*, vol. 2, pp. 1227-1232
- [4.15] B. M. Novac, I. R. Smith and K. Gregory, "Multi-pulse, twin-output high-voltage generator" *J. Phys. D: Appl. Phys.*, vol. 34, pp. 3239-3243, 2001
- [4.16] R. E. Reinovsky, "Fuse opening switches for pulse power applications", *Opening Switches*, ed A. Guenther et al, (New York: Plenum), pp. 209-232, 1987
- [4.17] J. V. Parker and W. M. Parsons, "Foil fuses as opening switches for slow discharge circuits", *Fifth IEEE Int. Pulse Power Conf. (Arlington, VA)*, ed P. J. Turchi and M. F. Rose, pp. 283-286, 1985
- [4.18] R. Latham, "HV vacuum insulation", *Academic press limited*, London, 1995
- [4.19] A. Watson, "The influence of crossed electric and magnetic field upon the breakdown voltage and prebreakdown current in vacuum", *J. Appl. Phys.*, vol. 51, no. 5, pp. 2527-2534, 1980
- [4.20] V. A. Petrosow, N. V. Cherkasskii, "The influence of transverse magnetic field on electric strength of high vacuum gap", *Sov. Phys. Tech. Phys.*, vol. 22, pp. 565, 1977
- [4.21] R. N. Sudan and R. V. Lovelace, "Generation of intense ion beams in pulsed diodes", *Phys. Rev. Lett*, vol. 31, pp. 1174-1177, 1973
- [4.22] R. Hawley, "The electrical properties of high vacuum" *High-voltage technology*, ed L. L. Alston, (Oxford University Press), pp. 59-94, 1968
- [4.23] Z. Kolaczowski, A. Rybski, S. Grzybowski and E. Kuffel, "Electric strength of point-point and point-plane gaps in vacuum in the presence of transverse magnetic field", *Proc. of Electrical Insulation and Dielectric Phenomena Conf. (Ottawa, Canada)*, pp. 66-71, 1988

- [4.24] A. Bouwers and P. G. Cath, "The maximum electrical field strength for several simple electrode configurations", *Philips Technical Rev.*, vol. 6, pp. 270-278, 1941
- [4.25] H. A. Wheeler, "Simple Inductance Formulas for Radio Coils", *Proc. of the Inst. of Radio Eng.*, vol. 16, pp. 1398-1400, 1928
- [4.26] L. Ludeking, D. Smithe, M. Bettenhausen, and S. Hayes, "MAGIC User's Manual. Newington", VA: MRC, Mar, 1999
- [4.27] N. Miura and S. Chikazumi, "Computer simulation of megagauss field generation by electromagnetic flux-compression", *Jap. J. Appl. Phys.*, vol. 18, no. 3, pp. 553-564, 1979
- [5.1] M. Istenič, B. M. Novac, J. Luo, R. Kumar and I. R. Smith and J. Brown, "Magnetically Insulated 1 MV Pulse Transformer", *IET Pulsed Power Symposium 2006, IET, Warrington, UK, October 2006*, pp 66-70
- [5.2] F. E. Terman, "Radio engineers' handbook.", McGraw-Hill, 1943
- [5.3] W. R. Smythe, "Static and dynamic electricity", McGraw-Hill, 1950
- [5.4] J. D. Craggs, J. M. Meek, "High voltage laboratory technique", *Butterworth scientific publications*, London, 1989
- [5.5] C. R. J. Hoffmann, "A Tesla transformer high-voltage generator", *Rev. of sci. instru.*, vol. 46, no. 1, pp.1-4, 1975
- [5.6] H. Matsuzawa and S. Suganomata, "Design charts for Tesla-transformer-type relativistic electron beam generators", *Rev. of Sci. Instru.*, vol. 53, no. 5, pp. 694-696, 1982
- [5.7] R. Hull, "The Tesla Coil Builder's guide to the Colorado Springs" *Notes of Nikola Tesla. Tesla Coil Builders of Richmond Virginia*, 1993
- [5.8] N. Tesla, "System of electric lighting", Patent no. 454622, 23, June, 1891
- [5.9] N. Tesla, "Apparatus for transmitting electrical energy", Patent no. 1119732, 1, December, 1914
- [5.10] N. Hardt, D. Koenig, "Testing of insulating materials at high frequencies and high voltage based on the Tesla transformer principle", *IEEE International Symposium on Electrical Insulation*, vol. 2, pp. 517-520, 1998
- [5.11] C. Boonseng, P. Apiratikul, and C. Phanomsarnrin, "A low cost approach to design the Tesla transformer for testing of insulating materials and

- industrial applications”, *IEEE International Symposium on Electrical Insulation*, pp. 248-251, 2002
- [5.12] B. T. Phung, T. R. Blackburn, et al., “Tesla transformer design and application in insulator testing” *7th International Symposium on High Voltage Engineering*, vol. 5, pp. 133-136, 1991
- [5.13] G. C. Damstra, J. A. J. Pettinga, “A six pulse kV Tesla transformer”, *5th International Symposium on High Voltage Engineering*, vol. 2, paper 62.13/1-3, 1987
- [5.14] M. A. Uman, “The lightning discharge”, *Academic Press*, 1987
- [5.15] Les Renardieres Group, “Positive discharges in long air gaps”, *Electra* 53, pp. 31-132, 1977
- [5.16] Les Renardieres Group, “Negative discharges in long air gaps”, *Electra* 74, pp. 67-216, 1981
- [5.17] V. P. Gubanov, S. D. Korovin, “Compact 1000 PPS high-voltage nanosecond pulse generator”, *IEEE Tran. on Plasma. Sci.*, vol. 25, no. 2, pp. 258-265, 1997
- [5.18] G. A. Mesyats, V. G. Shpak et al, “RADAN-EXPERT portable high-current accelerator”, *10th IEEE International Pulsed Power Conference*, vol.1, pp. 539-543, 1995
- [5.19] D. Finkelstein, P. Goldberg and J. Shucholawltz, “High voltage impulse system”, *Rev. of Sci. Instru*, vol. 37, no. 2, pp. 159-162, 1966
- [5.20] M. Denicolai, “Optimal performance for Tesla transformers”, *Rev. Sci. Instrum.*, vol. 73, no. 9, pp.1-5, 2002
- [5.21] M. Istenič, B. M. Novac, J. Luo, R. Kumar, I. R. Smith and J. Brown, “Magnetic insulation of MV pulse transformers”, *27th IEEE Power Modulator Symposium and 2006 High Voltage Workshop, Washington, DC, 14-18, May, 2006*
- [5.22] B. M. Novac, I. R. Smith and J. Brown, “Magnetically self-insulated transformers”, *J. Phys.D: Appl. Phys*, vol. 35, pp. 1467-1472, 2002
- [5.23] W. R. Smythe, “Static and dynamic electricity”, (NY: McGraw-Hill), 1950
- [5.24] J. Luo, B. M. Novac, I. R. Smith and J. Brown, “Fast and accurate two-dimensional modeling of high current, high-voltage air-cored transformers,” *J. Phys. D: Appl. Phys*, vol. 38, pp. 955-963, 2005

- [6.1] M. Istenič, B. M. Novac, J. Luo, R. Kumar and I. R. Smith "A 0.5 MV magnetically self-insulated pulsed transformer", *J. Phys. D: Appl. Phys.*, vol. 39, pp. 4529-4535, 2006
- [6.2] G. J. Rohwein, "A three megavolt transformer for PFL pulse charging", *IEEE Trans. Nucl. Sci.* vol. NS-26, pp. 4211-4213, 1979
- [6.3] Pulsed Megavolt High Voltage Divider Manual 2000 (Albuquerque, NM: North Star Research Corp)
- [6.4] CHO-SEAL 1215, Chomerics, Parker Hannifin Corp., Woburn, MA, USA, 1975
- [6.5] T. J. Tucker and R. P. Toth, "EBW1: A Computer Code for the Prediction of the Behavior of Electrical Circuits Containing Exploding Wire Elements." *Issued by Sandia Laboratories, operating for the United States Atomic Energy Commission* SF 1004-DF(2-74).SAND-75-0041, 1975
- [6.6] M. Lehr, R. Korzekwa, H. Krompholz and M. Kristiansen, "Magnetic-field effects on vacuum insulator flashover", *J. Appl. Phys.*, vol. 71, no. 1, pp. 389-394, 1992
- [6.7] R. Korzekwa, F. M. Lehr, H. G. Krompholz and M. Kristiansen, "Inhibiting Surface Flashover for Space Conditions Using Magnetic Fields", *IEEE Trans. on Plasma Sci.* vol. 17, no. 4, pp. 612-615, 1989
- [6.8] M. Istenič, B. M. Novac, J. Luo, R. Kumar and I. R. Smith and J. Brown, "Magnetically Insulated 1 MV Pulse Transformer", *IET Pulsed Power Symposium 2006, IET, Warrington, UK, October 2006*, pp 66-70
- [6.9] M. Istenič, B. M. Novac, J. Luo, R. Kumar and I. R. Smith, "A 1 MV magnetically insulated Tesla transformer", *J. Phys. D: Appl. Phys.*, (submitted for publication)
- [7.1] W. M. Widner, "Warp-10: a numerical simulation model for the cylindrical reconnection launcher", *IEEE Trans. Magnetics*, vol. 27, pp. 634-638, 1991
- [7.2] N. Miura and K. Nakao, "Computer analysis of megagauss field generation by condenser bank discharge" *Japan. J. Appl. Phys.*, vol. 29, pp. 1580-1599, 1990
- [7.3] B. M. Novac, I. R. Smith, M. C. Enache and H. R. Stewardson, "Simple 2D model for helical flux-compression generators", *Laser and Particle Beams*, vol. 15, pp. 379-95, 1997

- [7.4] K. Gregory, I. R. Smith, V. V. Vadher and M. J. Edwards, "Experimental validation of a capacitor discharge induction launcher model", *IEEE Trans. Magnetics*, vol. 31, pp. 599-603, 1995
- [7.5] B. M. Novac, I. R. Smith, M. C. Enache and P. Senior, "Studies of a very high efficiency electromagnetic launcher", *J. Phys. D: Appl. Phys.*, vol. 35, pp.1447-1457, 2002
- [7.6] B. M. Novac, I. R. Smith and M. Hubbard, "2D modeling of electromagnetic flux-compression in θ -pinch geometry", *IEEE Trans. Plasma Sci.*, vol. 32, no. 5, pp. 1896-1901, 2004
- [7.7] G. J. Rohwein, "A three megavolt transformer for PFL pulse charging", *IEEE Trans on Nuclear Science*, vol. NS-26, pp. 4211-4213, 1979
- [7.8] J. Luo, B. M. Novac, I. R. Smith and J. Brown, "Fast and accurate two-dimensional modeling of high current, high-voltage air-cored transformers," *J. Phys. D: Appl. Phys*, vol. 38, pp. 955-963, 2005
- [7.9] B. M. Novac, M. Istenič, J. Luo, I. R. Smith et. al., "A 10-GW Pulsed Power Supply for HPM Sources" *IEEE Trans. on Plasma Sci.*, vol. 34, pp. 1814-1821, 2006

